# Vibration Dynamics and Control of Vehicle and Rotor Systems

Lead Guest Editor: Xiao-ting Rui
Guest Editors: Dieter Bestle, Chuanzeng Zhang, Xuping Zhang,
Pierangelo Masarati, and Chengzhi Yuan

Vibration Dynamics and Control of Vehicle and Rotor Systems

Vibration Dynamics and Control of Vehicle and Rotor Systems

Lead Guest Editor: Xiao-ting Rui
Guest Editors: Dieter Bestle, Chuanzeng Zhang, Xuping Zhang, Pierangelo Masarati, and Chengzhi Yuan

Amal Hajjaj (iD), United Kingdom

Mohammad A. Hariri-Ardebili (iD), USA

Seyed M. Hashemi (iD), Canada

Xue-qiu He, China

Agustin Herrera-May (iD), Mexico

M.I. Herreros (iD), Spain

Duc-Duy Ho (iD), Vietnam

Hamid Hosano (iD), Japan

Jin Huang (iD), China

Ahmed Ibrahim (iD), USA

Bernard W. Ikua, Kenya

Xingxing Jiang (iD), China

Jiang Jin (iD), China

Xiaohang Jin, China

MOUSTAFA KASSEM (iD), Malaysia

Shao-Bo Kang (iD), China

Yuri S. Karinski (iD), Israel

Andrzej Katunin (iD), Poland

Manoj Khandelwal, Australia

Denise-Penelope Kontoni (iD), Greece

Mohammadreza Koopialipoor, Iran

Georges Kouroussis (iD), Belgium

Genadijus Kulvietis, Lithuania

Pradeep Kundu (iD), USA

Luca Landi (iD), Italy

Moon G. Lee (iD), Republic of Korea

Trupti Ranjan Lenka (iD), India

Arcanjo Lenzi, Brazil

Marco Lepidi (iD), Italy

Jinhua Li (iD), China

Shuang Li (iD), China

Zhixiong Li (iD), China

Xihui Liang (iD), Canada

Tzu-Kang Lin (iD), Taiwan

Jinxin Liu (iD), China

Ruonan Liu, China

Xiuquan Liu, China

Siliang Lu, China

Yixiang Lu (iD), China

R. Luo (iD), China

Tianshou Ma (iD), China

Nuno M. Maia (iD), Portugal

Abdollah Malekjafarian (iD), Ireland

Stefano Manzoni (iD), Italy

Stefano Marchesiello (iD), Italy

Francesco S. Marulo, Italy

Traian Mazilu (iD), Romania

Vittorio Memmolo (iD), Italy

Jean-Mathieu Mencik (iD), France

Laurent Mevel (iD), France

Letícia Fleck Fadel Miguel (iD), Brazil

FuRen Ming (iD), China

Fabio Minghini (iD), Italy

Marco Miniaci (iD), USA

Mahdi Mohammadpour (iD), United Kingdom

Rui Moreira (iD), Portugal

Emiliano Mucchi (iD), Italy

Peter Múčka (iD), Slovakia

Fehmi Najar, Tunisia

M. Z. Naser, USA

Amr A. Nassr, Egypt

Sundararajan Natarajan (iD), India

Toshiaki Natsuki, Japan

Miguel Neves (iD), Portugal

Sy Dzung Nguyen (iD), Republic of Korea

Trung Nguyen-Thoi (iD), Vietnam

Gianni Niccolini, Italy

Rodrigo Nicoletti (iD), Brazil

Bin Niu (iD), China

Leilei Niu, China

Yan Niu (iD), China

Lucio Olivares, Italy

Erkan Oterkus, United Kingdom

Roberto Palma (iD), Spain

Junhong Park (iD), Republic of Korea

Francesco Pellicano (iD), Italy

Paolo Pennacchi (iD), Italy

Giuseppe Petrone (iD), Italy

Evgeny Petrov, United Kingdom

Franck Poisson (iD), France

Luca Pugi (iD), Italy

Yi Qin (iD), China

Virginio Quaglini (iD), Italy

Mohammad Rafiee (iD), Canada

Carlo Rainieri (iD), Italy

Vasudevan Rajamohan (iD), India

Ricardo A. Ramirez-Mendoza (iD), Mexico

José J. Rangel-Magdaleno (iD), Mexico

Contents

Research Article

Influence of Wheel Profile Wear Coupled with Wheel Diameter Difference on the Dynamic Performance of Subway Vehicles

H. X. Li [ID],[1,2] **A. H. Zhu** [ID],[1,2] **C. C. Ma,**[1,2] **P. W. Sun,**[1,2] **J. W. Yang** [ID],[1,2] **and K. Q. Zhang**[1,2]

[1]*Beijing Key Laboratory of Performance Guarantee of Urban Rail Transit Vehicles,*
 Beijing University of Civil Engineering and Architecture, Beijing 100044, China
[2]*School of Mechanical-Electronic and Vehicle Engineering, Beijing University of Civil Engineering and Architecture,*
 Beijing 100044, China

Correspondence should be addressed to A. H. Zhu; zhuaihua@bucea.edu.cn

In view of the coexistence of wheel profile wear (WPW) and wheel diameter difference (WDD) on an actual subway line, a dynamic analysis method based on coupling between WPW and equivalent in-phase WDD was proposed. Based on the measurements from a subway vehicle in operation on this line, dynamics modeling and calculations were performed for a single carriage of this vehicle. Later, the interaction between the effects of WPW and equivalent in-phase WDD on the vehicle dynamic performance was analyzed, and the dynamic response in the presence of coupled damage was compared between the outer and inner wheels. Furthermore, the difference in the dynamic response caused by different positions of the larger-diameter wheels (i.e., on the inner track or outer track) was analyzed for the case where equivalent in-phase WDD occurred between the front and rear bogies. The results show that when the vehicle ran on a straight line, the coupling between WPW and WDD reduced the vehicle's stability but improved its ride comfort. When the vehicle traveled on a curved line, it showed reductions in the lateral wheel/rail contact force, derailment coefficient, axle lateral force, and wear index if the outer wheels had a larger diameter. As a result, the deterioration of the vehicle's dynamic performance due to the increasing degree of WPW slowed down, and its curve negotiation performance improved. Meanwhile, the outer wheels had significantly greater lateral wheel/rail contact force, derailment co-efficient, and wear index compared to the inner wheels. When a −1 mm WDD was coupled with the worn wheel profile for 14×10^4 kilometers traveled, the dynamic performance indexes of the vehicle were close to or even exceeded the corresponding safety limits. The findings can provide technical support for subway vehicle maintenance.

1. Introduction

During subway operation, longitudinal and lateral wheel/rail forces will arise from traction and braking, as well as the centrifugal effect in the process of curve negotiation, resulting in various types of damage to wheels and rails. Moreover, due to growing subway traffic flow and train speed, frequent starting and braking, and the increasing number of small-radius curved lines, wheels are suffering increasingly severe damage. In particular, wheels are often subject to more diverse, complex damage rather than one damage type. The major types of wheel damage include wheel profile wear (WPW), wheel diameter difference (WDD), and tread peeling. WPW and WDD usually coexist

as the most common coupled damage, which is difficult to solve, imposes high repair cost, and has a significant impact on the safety and comfort of subway vehicles. Therefore, studying the influence of WPW coupled with WDD on subway vehicle dynamics has practical significance.

For a subway vehicle in operation, its wheels are inevitably subject to tread and flange wear caused by wheel/rail contact and braking, resulting in changes in wheel profiles. As the distance traveled increases, the degree of wear tends to increase and wheel profiles tend to vary.

A great deal of research has investigated the influence of WPW on vehicle dynamics by theoretical, simulation, or experimental approaches. Cui et al. studied the influences of different wear forms on vehicle dynamics by field test

combined with simulations and analysis and found that the false flange created by wheel wear would endanger the operational safety of the vehicle [1]. Lu et al. created a dynamic model for a Type B metro vehicle with Universal Mechanism (UM), a software package for simulation of multibody system dynamics, and analyzed the influence of wheel wear on vehicle dynamic performance and the characteristics of wheel/rail contact damage [2]. Yao et al. studied the effects of wheel wear on the dynamics performance of a high-speed train and suggested that the vehicle system's transverse stability index linearly decreased as the depth of wheel wear increased [3]. S. Pradhan et al. [4] investigated the influences of various stages of wheel wear on the dynamic responses such as curving performance and then evaluated the critical speed and ride comfort of the railway vehicle on the simulated test track to justify the maintenance schedule. Sun et al. simulated the multipoint contact and non-Hertzian contact between worn wheel and rail using a modified Kik-Piotrowski method. The wheel/rail normal vertical force, wheel/rail creep force, and contact patch shape predicted with this method are in good agreement with the results of contact calculation [5]. By measuring tread and rail profiles, Zong et al. analyzed the impact of equivalent conicity on the nonlinear critical speed of metro vehicles [6]. Shi et al. experimentally tested the dynamic performance of a high-speed train running at 300 km/h and revealed that the vibration of axle box, frame, and car body tended to intensify gradually with increasing wheel wear [7]. Using a vehicle-turnout coupling dynamic model, Xiao et al. analyzed the dynamic response of a high-speed train with wheel wear when it passed a turnout. They found that wheel-rail wear caused an increase in wheel/rail vertical force and a decline in wheel/rail transverse force [8]. Xu et al. studied the influence of the increase in wheel wear on vehicle dynamics through simulation with SIMPACK, with wheel/rail contact being considered as the entry point. The results showed a marked decreasing trend in the vehicle's critical speed [9]. Xie et al. found that as the speed increased, the influence of wheel harmonic wear on vehicle stability became increasingly significant [10]. The stochastic model for vehicle-track systems provided by Xu and Zhai enables good analysis of dynamic response and reliability of a vehicle-track system in the presence of varying wheel wear and stochastic track irregularity [11]. Liu and Bruni investigated the influence of individual wheel profiles measured on a rail vehicle on the vehicle's dynamics in the context of multibody (MB) simulations [12].

In terms of the effect of WDD on dynamic performance, Lyu et al. showed that when the initial WDD was large, cracks and localized wear occurred soon and always on wheelsets with smaller diameters, and they can deteriorate the dynamic performance of vehicles [13]. Sun et al. analyzed the influence of WDD on the stability, safety, and comfort of a vehicle traveling along a bridge by simulation and suggested that WDD should be strictly controlled for high-speed trains [14]. Jiang et al. constructed a nonlinear dynamic model for a metro vehicle and then calculated the critical speed, stability, safety, and wear power of the vehicle for different WDDs. The results showed that with the

increase in coaxial WDD, the critical speed decreased sharply while the lateral stability and wear power increased significantly [15]. Yan et al. studied the influence of front-axle WDD, rear-axle WDD, equivalent in-phase WDD, and equivalent antiphase WDD on the safety of a locomotive during motion on straight line and curved line [16]. Based on a high-speed train and 12# turnout of a passenger dedicated line in China, Chen et al. developed a vehicle-turnout dynamic model and systematically analyzed the stability, safety, and ride comfort of a high-speed vehicle passing through a turnout for different types and magnitudes of WDD. They suggested that the operational limits for in-phase and antiphase WDDs be set at 2 mm and 3 mm, respectively and the limit for coaxial WDD above which primary and secondary maintenance is needed be set at 1.5 mm [17]. Based on an analysis of the types of WDD, Ma et al. discussed the influence of WDD on the stress state and movement of wheelsets [18]. He et al. suggested that WDD can lead to a significant increase in lateral wheel/rail contact force for a locomotive running on a straight line [19]. Wang et al. found that the yaw angle of wheelset, lateral displacement, wear power, and creep force of wheelset sharply increased with greater WDD [20]. Liu et al. analyzed the influence of coaxial WDD on a locomotive's dynamic performance. The results revealed that the coaxial WDD changed the position of wheel-rail contact and increased the equivalent stress of the rail, which could impair the locomotive's dynamic performance [21]. Based on an electric locomotive equipped with three-axle bogies, Zhang et al. investigated the influence of WDD at different axles on locomotive dynamic performance. The results showed that both derailment coefficient and wheel unloading rate increased with increasing WDD at the first axle and decreased with increasing WDD at the other two axles [22]. By analyzing the forces acting on a bogie with WDD, Chi et al. theoretically inferred that the existence of WDD changed the balance position of the wheelset center and thereby changed the wheel/rail contact relationship and affected the vehicle system's stability [23].

These researchers have looked at the influence of WPW or WDD on vehicle dynamics from various perspectives and offered insights into how to solve relevant dynamic performance problems. Research related to WPW focused mainly on how wear depth, harmonic wear, and crater wear affect vehicle dynamic performance, and research related to WDD emphasized the effect of the type and range of WDD.

However, most of these studies only considered the influence of a single type of wheel damage on vehicle dynamics, neglecting the coexistence of multiple damage types and the interaction between the effects of different damage types on vehicle dynamics. The present study analyzed the data on wheel damage measured on a specific subway line and found that WPW and equivalent in-phase WDD are the main types of wheel damage in vehicles running on this line. So, WPW and equivalent in-phase WDD were considered together to further analyze the influence of coupled wheel damage on vehicle dynamic performance.

Moreover, the existing research only considered front bogie, neglecting a real situation where both front and rear

bogies have WDD. So, the present study considered the occurrence of equivalent in-phase WDD at the front and rear bogies and then analyzed the difference in dynamic response caused by different positions of the larger-diameter wheels, i.e., on the inner track or outer track.

Additionally, in vehicle dynamics modeling, these researchers only considered wheel damage in a single wheelset and set other wheelsets as standard ones. This cannot accurately reflect the actual characteristics of wheel damage. The present study not only considered the characteristics of damage in all wheels based on measured data but also compared the dynamic responses of the inner and outer wheels.

2. Analysis of Measured Wheel Data

A subway vehicle operating on a subway line has been tracked in this study. This vehicle consists of 6 carriages, each having 8 wheels. The profiles and diameters of these 48 wheels have been measured since the beginning of the vehicle's operation. The wheel profile and diameter data were collected when the distance traveled reached 5×10^4, 8×10^4 and 14×10^4 km.

2.1. Measured Wheel Profiles. Wheel/rail contact can be divided into three regions, as shown in Figure 1. Region A is the contact region between wheel tread and railhead. Wheel/rail contact in this region usually occurs when a vehicle travels on a straight line or a large-radius curve. Region B is the region of contact between wheel flange and track corner, which often occurs when a vehicle runs on a small-radius curve. In region C, wheel/rail contact is highly unlikely to occur.

The profiles of the subway vehicle's wheels were tracked and analyzed. It was found that wheel wear was located largely in region A, as shown in Figure 1. The wear in this region is called tread wear. The test vehicle in this study has 6 carriages, and 1 carriage was selected for dynamic modeling to allow for more time-efficient simulations and calculations. An analysis of the measurements found that the differences in maximum tread wear depth between the 6 carriages were about 10%, and the worst wheel wear occurred in the No. 2 carriage. So, No. 2 carriage was selected for dynamics modeling. The measured profile of this carriage's 8 wheels was used for its dynamics model in order to allow the results to reflect its actual status.

Figure 2 illustrates the maximum tread wear depths in the 8 wheels measured when the distance traveled reached 5×10^4, 8×10^4, and 14×10^4 km. The left wheels were numbered 1, 3, 5, and 7, and the right ones were numbered 2, 4, 6, and 8.

In order to reduce cuspidal points on tread profile and prevent accumulation of errors during curve fitting, a data processor based on cubic spline interpolation algorithm was compiled in MATLAB software to smooth the wheel tread data [24]. The computational formula is

$$y(x) = f(x) + \varepsilon(x), x \in [a, b], \tag{1}$$
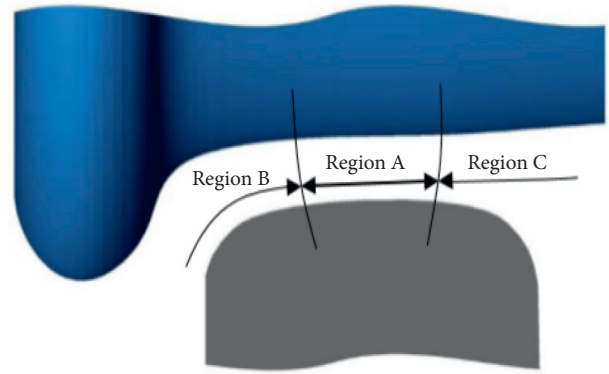
Figure 1: Wheel/rail contact regions.
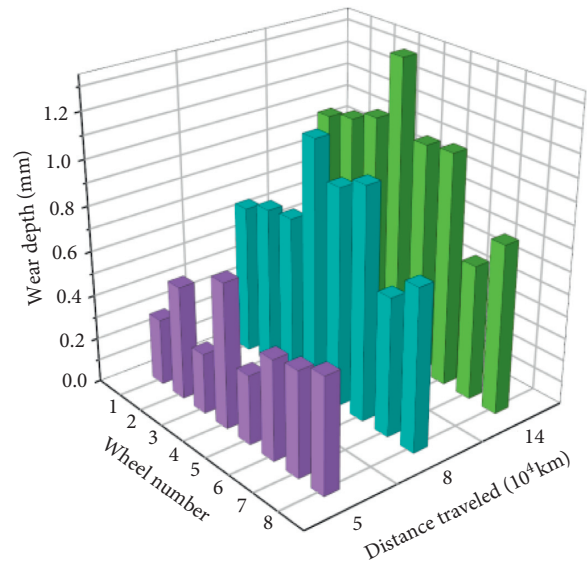
Figure 2: Measured tread wear depths.

where $f(x)$ is the cubic spline smooth curve, $\varepsilon(x)$ is the random error, $y(x)$ is the experimental data, and $[a, b]$ is the range of abscissa of the wheel profile.

Then, the 8 wheels' profiles for 5×10^4, 8×10^4, and 14×10^4 km traveled shown in Figure 3 were used for subsequent modeling.

2.2. Analysis of the WDD Data. For a subway vehicle, the degree of wear varies between wheels due to the complex, variable conditions during actual operation. Figure 4 shows the four types of WDD for two-axle bogies, with "v" at the top indicating the direction of vehicle movement. They are as follows: (I) front WDD (the left and right wheels on the front axle have different diameters), (II) rear WDD (the left and right wheels on the rear axle have different diameters), (III) equivalent in-phase WDD (the smaller-diameter wheels on the front and rear axles are on the same side), and (IV) equivalent antiphase WDD (the smaller-diameter wheels on the front and rear axles are on opposite sides) [25]. According to the literature

(a)

(b)

(c)
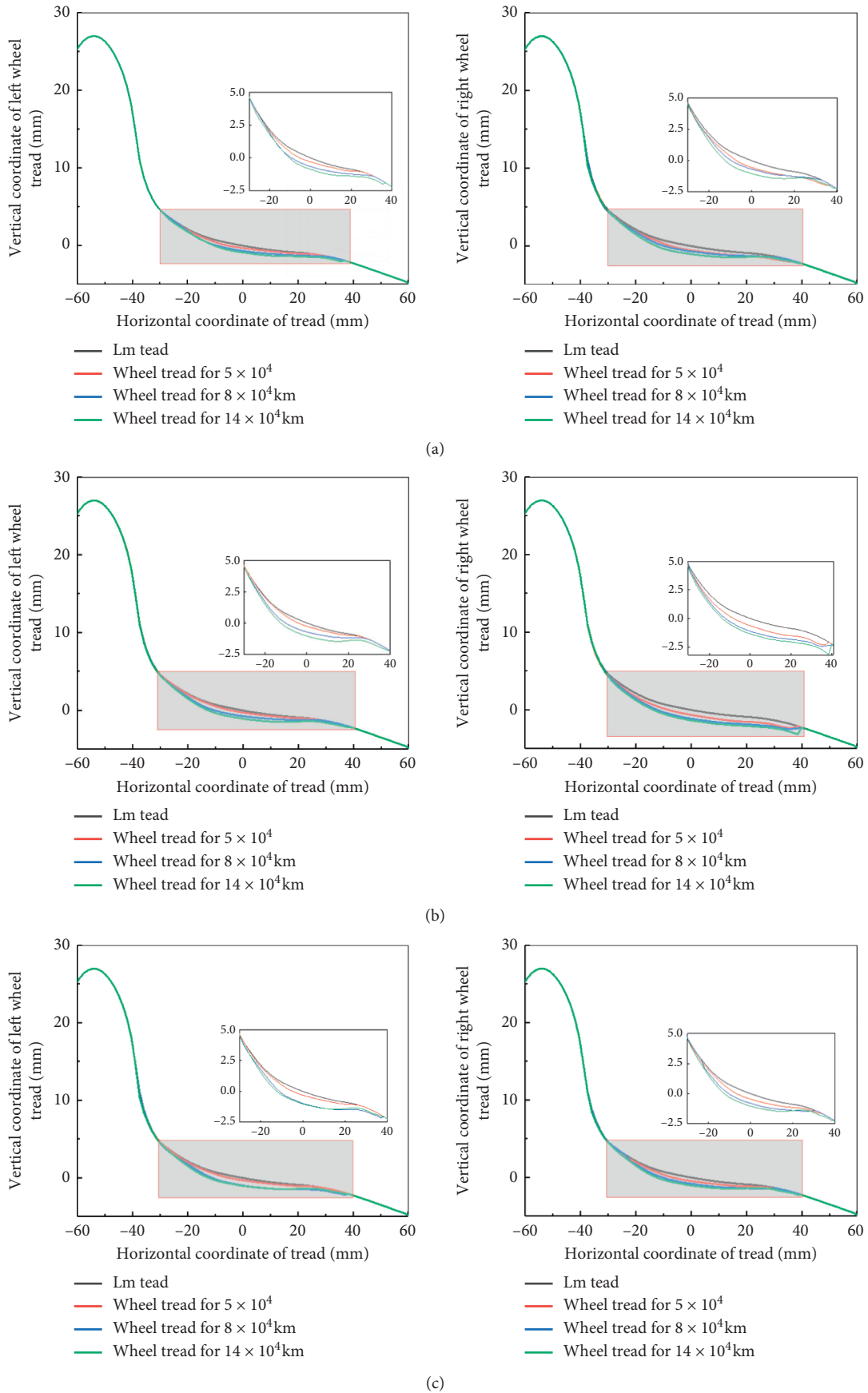
Figure 3: Continued.
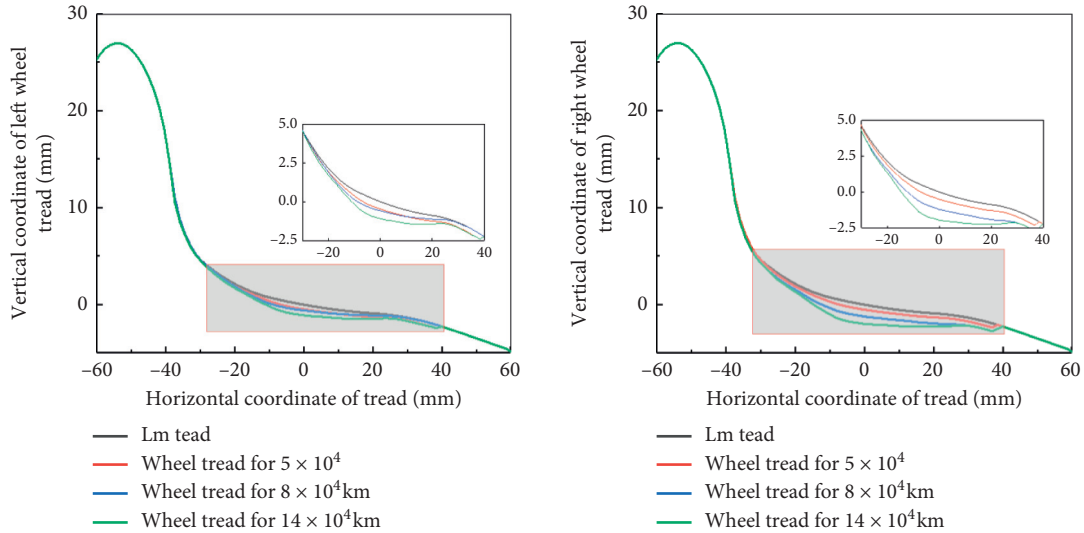
(d)

FIGURE 3: Measured wheel profiles. (a) First-axle wheel profiles. (b) Second-axle wheel profiles. (c) Third-axle wheel profiles. (d) Fourth-axle wheel profiles.
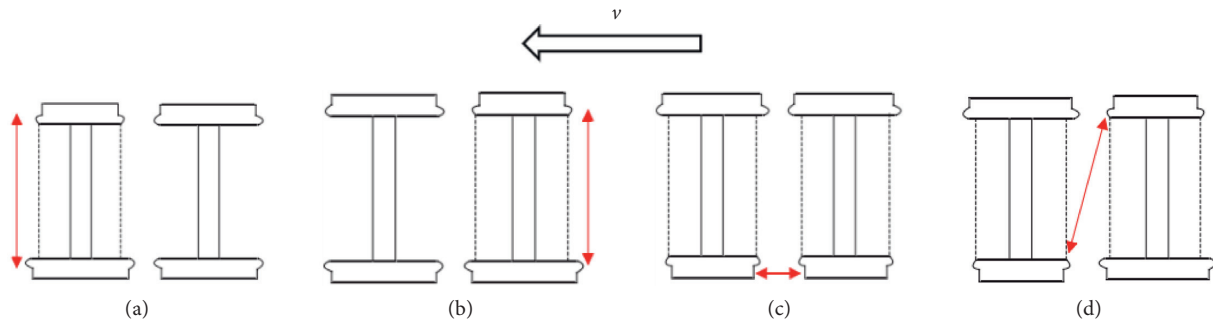
FIGURE 4: Types of WDD: (a) front WDD, (b) rear WDD, (c) equivalent in-phase WDD, and (d) equivalent antiphase WDD.

[26–27], of the four types of WDD, equivalent in-phase WDD has the greatest influence on the curve negotiation performance of vehicles.

The diameters of wheels of a subway vehicle were tracked. This wheel diameter measuring instrument is used for measuring the diameter of a wheel's rolling circle. It works by three-point indirect measurement and shows readings on a mechanical indicator, which allows users to get diameter reading directly. It is characterized by small measurement error, high indication stability, low weight, and ease of use.

An analysis of the measured diameter data reveals that there was equivalent in-phase WDD between the front and rear bogies of each carriage after a long-term operation on the same line. In other words, the smaller-diameter wheels of the front and rear bogies were on the same side, as illustrated in Figure 5. For this reason, equivalent in-phase WDD was applied to modeling to study its effect on vehicle dynamic performance.

WDD refers to the difference between the nominal rolling radii of the left and right wheels. A wheelset's diameter difference is defined by

$$\Delta D = D_{\text{outer}} - D_{\text{inner}}, \qquad (2)$$

where D_{inner} is the diameter of the wheel on the inner track (inner wheel); D_{outer} is the diameter of the wheel on the outer track (outer wheel); and $\Delta D < 0$ indicates that the inner wheel diameter is greater than that of the outer wheel diameter.

According to a relevant regulation of China, a wheelset needs to be repaired when its coaxial diameter difference reaches 1 mm. Given the possibility of machining error, the technical specification for wheelset assembly allows WDD of less than 0.3 mm [28]. Table 1 provides the values of equivalent in-phase WDD set in this study.

3. Dynamics Models for the Vehicle-Track System

3.1. Vehicle Dynamics Model. A vehicle dynamics model was constructed based on the parameters of the Type B vehicle tracked. It consists primarily of 1 vehicle body, 2 frames, 4 wheelsets, 8 axle boxes, and primary and secondary suspension systems. The vehicle body, frames, and wheelsets are
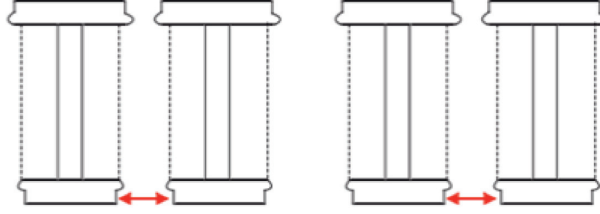
FIGURE 5: Equivalent in-phase WDD between the front and rear bogies.

TABLE 1: Wheel diameter difference setting.

Condition	Left wheel (outer) diameter (mm)	Right wheel (inner) diameter (mm)	WDD (mm)
1	839	840	−1
2	839.2	840	−0.8
3	839.5	840	−0.5
4	839.8	840	−0.2
5	840	840	0
6	840	839.8	0.2
7	840	839.5	0.5
8	840	839.2	0.8
9	840	839	1

all treated as rigid bodies, and each has six degrees of freedom (DOFs), including surging, swaying, heaving, rolling, pitching, and yawing. The whole vehicle has 50 DOFs in total. The dynamic equation of motion for the vehicle is as follows [29]:

$$M\ddot{X} + C\dot{X} + KX = P, \tag{3}$$

where M, C, and K are the mass matrix, damping matrix, and stiffness matrix, respectively, for the vehicle system; X is the generalized displacement; and P is the generalized load.

The vehicle dynamics model is shown in Figure 6, and the main parameters of the vehicle are presented in Table 2 [30].

The track was simulated with standard UIC60 rail and German high-speed spectrum was applied for track excitation. The subway line was simulated with two line types: straight line and curved line, with each being 1000 m long in total. The curved line is C-shaped and composed of five parts, which are a straight segment, a transition curve, a circular curve, a transition curve, and a straight segment in sequence. The circular curve has a radius of 300 m. The composition is shown in Table 3. Moreover, the curved line was set as a right-turning line. Along the direction of vehicle movement, the left wheels were designated as the outer wheels and the right wheels as the inner wheels. If its direction was changed to left-turning because the wheel diameter difference changes symmetrically from −1 mm to 1 mm, the dynamic performance change rule is the same, and only the inner wheel and outer wheel are exchanged.

Based on the actual operational characteristics of the test line, variable velocity was set for the vehicle to simulate its acceleration, coasting, and deceleration, and the maximum velocity was set at 65 km/h. Then, the functional relationship between vehicle velocity v and distance traveled s is obtained:
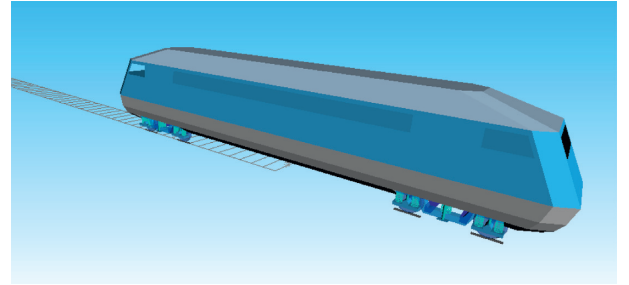
FIGURE 6: Vehicle dynamics model.

$$v(s) = \begin{cases} -2.76 \times 10^{-4}s^2 + 0.276s, & (0 < s \le 360; 630 < s \le 1000), \\ 65, & (360 < s \le 630). \end{cases} \tag{4}$$

The piecewise velocity function $v(s)$ above can be used to simulate the process of velocity change as the initially static vehicle starts by traction, then coasts, and finally brakes to stop along a 1000 m curved line.

Hertz's theory is used for solving normal contact problems, and Kalker's simplified theory and the corresponding FASTSIM algorithm are applied to calculate the distribution and magnitude of the tangential creep forces within the contact patch.

3.2. Model of Coupling between WPW and WDD.

During modeling of vehicle dynamics, the wheel wear data measured when the distance traveled reached 5×10^4, 8×10^4, and 14×10^4 km were imported into the wheel profile database to obtain worn wheel profiles, which are represented by $S1$, $S2$, and $S3$, respectively (Table 4). Then, worn wheel profile models were constructed by applying the profile data shown in Figure 3 to the eight wheels of each carriage.

TABLE 2: Main parameters of the vehicle.

Parameter	Value	Unit
Vehicle body mass	33859	kg
Vehicle body's moment of inertia in roll	73105	kg·m^2
Vehicle body's moment of inertia in pitch	1157173	kg·m^2
Vehicle body's moment of inertia in yaw	1171980	kg·m^2
Frame mass	2103	kg
Frame's moment of inertia in roll	1333	kg·m^2
Frame's moment of inertia in pitch	864	kg·m^2
Frame's moment of inertia in yaw	2131	kg·m^2
Wheelset mass	1018	kg
Wheelset's moment of inertia in roll	546.7	kg·m^2
Wheelset's moment of inertia in pitch	75	kg·m^2
Wheelset's moment of inertia in yaw	546.7	kg·m^2
Primary suspension system's vertical stiffness	1.3	MN/m
Primary suspension system's vertical damping coefficient	1840	N.s/m
Secondary suspension system's vertical damping coefficient	25 (0.15 m/s)	kN·s/m
Secondary suspension system's lateral damping coefficient	58 (0.1 m/s)	kN·s/m

TABLE 3: C-shaped line composition.

Number	Line type	Length (m)
1	Straight line	245
2	Transition curve	55
3	R300 circular curve	400
4	Transition curve	55
5	Straight line	245

TABLE 4: Worn wheel profiles for different distances traveled.

Distance traveled	5×10^4 km	8×10^4 km	14×10^4 km
Worn wheel profile	S1	S2	S3

Later, the WDD model was built by setting wheel diameters using the Geometry module in SIMPACK. In accordance with Table 1, the WDD was set at 9 values, including −1 mm, −0.8 mm, −0.5 mm, −0.2 mm, 0 mm, 0.2 mm, 0.5 mm, 0.8 mm, and 1 mm.

After that, the coupling between WPW and WDD was modeled by applying the diameter values to corresponding worn wheel profiles in the vehicle dynamics model.

3.3. Validation of the Vehicle Dynamics Model. Ride comfort is an important factor considered in assessing the comfort of vehicles. Ride comfort index and vibration acceleration are widely adopted to evaluate the dynamic performance of vehicles around the world [31]. The ride comfort index of a vehicle, W, can be calculated as follows [32].

$$W = 0.896 \sqrt[10]{\frac{a^3}{f} F(f)}, \tag{5}$$

where a is the vibration acceleration (cm/s^2); f is the frequency of vibration (Hz); and $F(f)$ is the correction factor related to f.

After the vehicle dynamics model was constructed based on the parameters of the actual vehicle and the line status, the vertical acceleration and ride comfort index of the model were calculated. The results were then compared with the measured data to verify the reliability of the model so as to ensure accurate results of the subsequent simulation.

A vibration test was conducted on the studied vehicle, and the test data were collected with COINV DASP, a software package developed by the China Orient Institute of Noise and Vibration. In accordance with the Railway vehicles, specification for evaluation of the dynamic performance and accreditation test (GB5599-1985), an accelerometer was mounted on the floor to the left of the front bogie (1 m from the bogie pivot center) to measure the vehicle's acceleration and the sampling frequency was 1024 Hz. The acceleration data obtained are plotted in Figure 7.

The simulated acceleration was compared with the measured acceleration and then the ride comfort index was calculated from the simulated and measured data using equation (5).

As can be seen in Table 5, the maximum peak vertical acceleration obtained by simulation is slightly smaller than the measured value. The reason is that some parts of the vehicle's structure were simplified in modeling. However, the amplitudes of the simulated and measured values varied in similar ways. The simulated time of the maximum peak is quite close to the measured value, suggesting the high reliability of the vehicle dynamics model proposed in the paper.

4. Influence of WPW Coupled with WDD on the Dynamic Performance of a Vehicle Running on a Straight Line

Three worn wheel profiles for 5×10^4, 8×10^4, and 14×10^4 km traveled (see Figure 3 and Table 4) and nine WDDs between −1 mm and +1 mm (Table 1) were set based on the measured data from the test vehicle. Later,
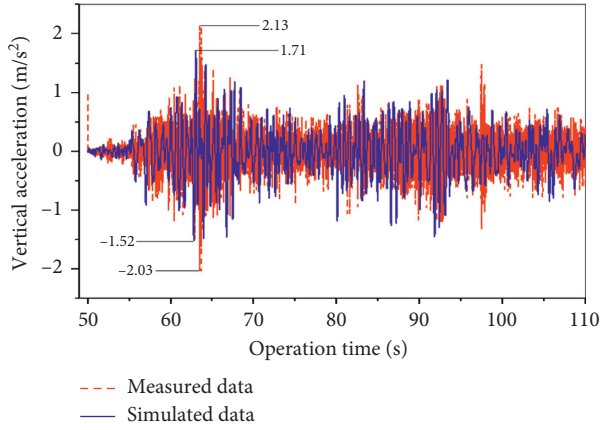
FIGURE 7: Comparison of vertical acceleration.

TABLE 5: Comparison of simulated and measured data.

Acceleration value	Measured value A (s)	Simulated value B (s)	Rate of change $100x(A - B)/A$ (%)
Maximum peak vertical acceleration (m/s^2)	2.13	1.71	19.72
	−2.03	−1.52	25
Time of the maximum peak	63.443 s (2.13 m/s^2)	62.164 s (1.71 m/s^2)	2.02
	63.441 s (−2.03 m/s^2)	62.168 s (−1.52 m/s^2)	2.01
Ride comfort index	2.2107	2.1659	2.03

the vehicle dynamics model shown in Figure 6 was used to calculate and analyze the influence of WPW coupled with equivalent in-phase WDD on the stability and ride comfort of the vehicle.

4.1. Hunting Stability. Hunting stability is an extremely important aspect of vehicle dynamic performance. Critical speed is the most direct indicator for hunting stability assessment. When a vehicle runs at a normal speed, it is necessary to ensure the overall stability of the vehicle system and protect it from instability; otherwise, the vehicle will snake heavily, thus affecting its operational quality and safety.

In this paper, the critical speed was calculated using the acceleration reduction method. At first, sinusoidal excitation was applied to rails on the straight line and a force was exerted on the vehicle body (The magnitude is half the weight of the vehicle body and in the opposite direction of the vehicle movement). Then, the vehicle started to move and its equilibrium position during vibration was observed. The vehicle velocity at this position was defined as the critical speed. As shown in Figure 8, the equilibrium point in condition S1 occurred at 171 km/h, so the critical speed was 171 km/h.

Figure 9 illustrates the critical speed for different degrees of WPW coupled with different WDDs. The following are shown in Figure 9:

(1) It is clear from the figure that for a given WDD, increasing the degree of WPW gradually reduced the critical speed and thereby the vehicle stability. When the WDD was −1, −0.8, −0.5, −0.2, 0, 0.2, 0.5, 0.8, and 1 mm, the critical speed for worn wheel profile S3 decreased by 32.3%, 30.3%, 35.1%, 33.7%, 33.3%, 32.9%, 31.5%, 33.8%, and 36.3%, respectively, compared with that for S1. The rate of decrease differs slightly between different WDDs.

(2) For a given worn wheel profile, the critical speed in the presence of WDD was lower that in the absence of WDD. Besides, as the absolute value of WDD increased, the critical speed tended to decline and had a roughly symmetric distribution. This trend is most marked for S1, where the critical speed for a −1 mm WDD ($(D_{\text{inner}} > D_{\text{outer}})$) decreased by 47 km/h compared to the critical speed for a 0 WDD. In condition S3, when WDD was −1, −0.8, 0.8, and 1 mm, the vehicle's critical speed was 86, 92, 96, and 91 km/h, respectively, which are all below the maximum allowable speed for running along the studied line, 100 km/h. The actual maximum speed of a vehicle running on a straight line is restricted by its critical speed. If the actual speed exceeds the four critical levels, it will snake heavily and lose lateral stability, leading to passenger discomfort and even derailment in a worse-case scenario.

(3) Whether the larger-diameter wheels are on the inner side or outer side has little influence on the critical speed. As the WDD changed, the critical speed had an approximately symmetrical distribution.

The analysis above demonstrates that the critical speed tended to decline with increasing WDD and WPW. This is primarily because the presence of WDD caused the rolling wheelsets to deviate from the centerline of the track and thereby increased wheelsets' lateral displacement and angle of offset. Consequently, the geometry of wheel/rail contact was altered and the critical speed declined. Meanwhile, as the equivalent conicity increased with the increasing degree of WPW, the nonlinear critical speed of the vehicle gradually declined.

4.2. Vehicle Ride Comfort. The operational performance of trains is commonly measured by the ride comfort index, which can be graded in accordance with Table 6.

Figure 10 demonstrates the influence of different degrees of WPW coupled with different WDDs on the vehicle's ride comfort. Figures 10(a) and 10(b) illustrate the lateral ride comfort index and vertical ride comfort index, respectively.

(1) For a given WDD, the ride comfort index tended to increase with increasing the degree of WPW in both the vertical and lateral directions. When the WDD

(a)

(b)
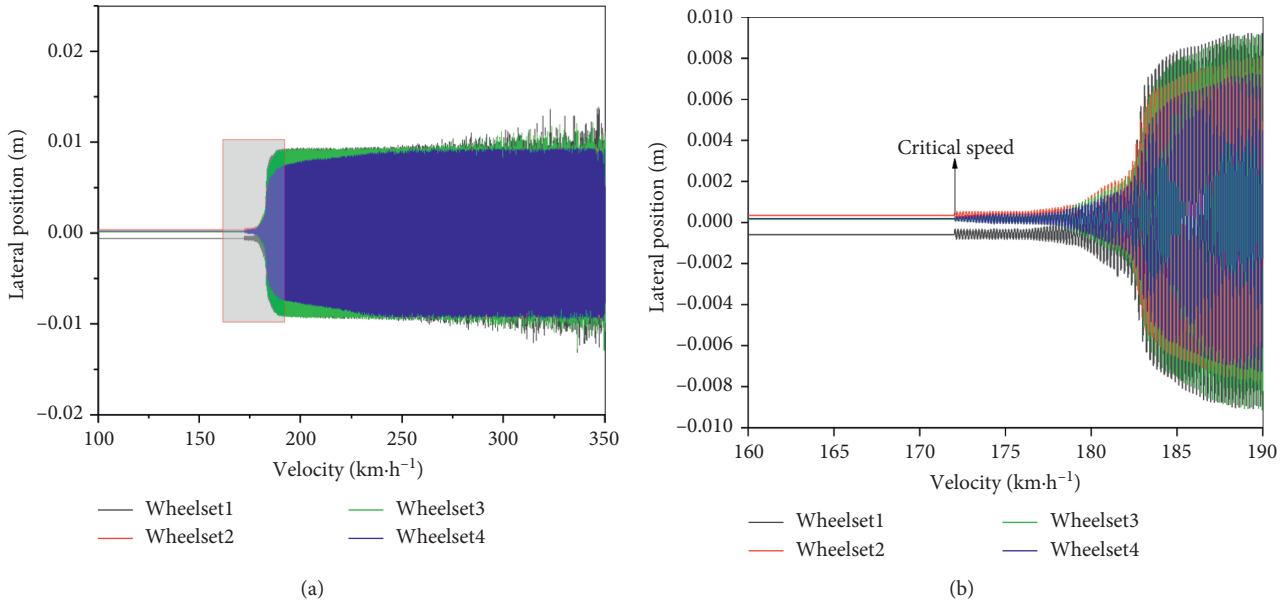
FIGURE 8: Schematic diagram of critical speed. (a) Critical speed in condition $S1$. (b) Detail.
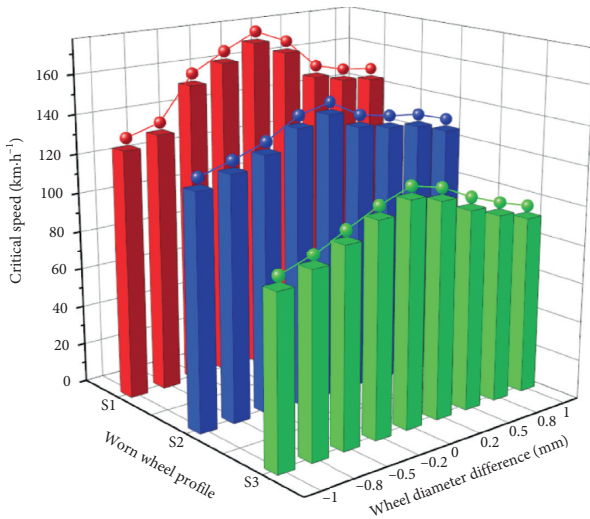
FIGURE 9: Critical speed.

TABLE 6: Vehicle ride comfort index and grading.

Grade	Rating	Ride comfort index		
		Carriage	Locomotive	Freight car
1	Excellent	<2.5	<2.75	<3.5
2	Good	2.5~2.75	2.75~3.10	3.5~4.0
3	Fair	2.75~3.0	3.1~4.0	4.0~4.25

was −1, −0.8, −0.5, −0.2, 0, 0.2, 0.5, 0.8, and 1 mm, the lateral ride comfort index for worn wheel profile $S3$ increased 18.5%, 19%, 19.1%, 21.1%, 23%, 20.8%, 17.2%, 16.9%, and 15.9%, respectively, compared to that for $S1$. The corresponding increases in the vertical ride comfort index were 25.9%, 27.3%, 30.5%, 38.2%, 45.1%, 41.5%, 39.9%, 38.3%, and

30.6%, greater than the increases in the lateral ride comfort index. Moreover, as the absolute value of WDD increased, the increase in the ride comfort index caused by profile change tended to decline slightly. This indicates that the presence of WDD can inhibit the negative effect of profile change on the ride comfort index to some extent.

(2) Figure 11 illustrates how the vibration acceleration varied with the degree of WPW when the WDD was 0. It was found that the vertical and lateral accelerations increased with greater WPW, which is consistent with the trend in the ride comfort index described in (1).

(3) For a given worn wheel profile, as the absolute value of WDD increased, the lateral and vertical ride comfort indexes declined compared to those for 0 WDD, and their distributions are approximately symmetric. An inference is that a proper WDD can help improve the ride comfort of vehicles. In addition, the approximately symmetric distribution suggests that whether the larger-diameter wheels are on the inner side or outer side has little effect on the ride comfort index.

As the degree of WPW increased, the amplitudes of vertical and lateral accelerations expanded, increasing the ride comfort index. In the presence of WDD, the creep forces on the left and right wheels caused the wheelsets to yaw clockwise, resulting in lateral displacement of wheelsets. When equivalent in-phase WDD occurred between the front and rear wheelsets of a bogie, the front and rear wheelsets would move towards the same side, which will not cause a significant deflection of the bogie. Therefore, a very small angle of offset between the front and rear wheelsets will help improve the ride comfort of the vehicle system [33].
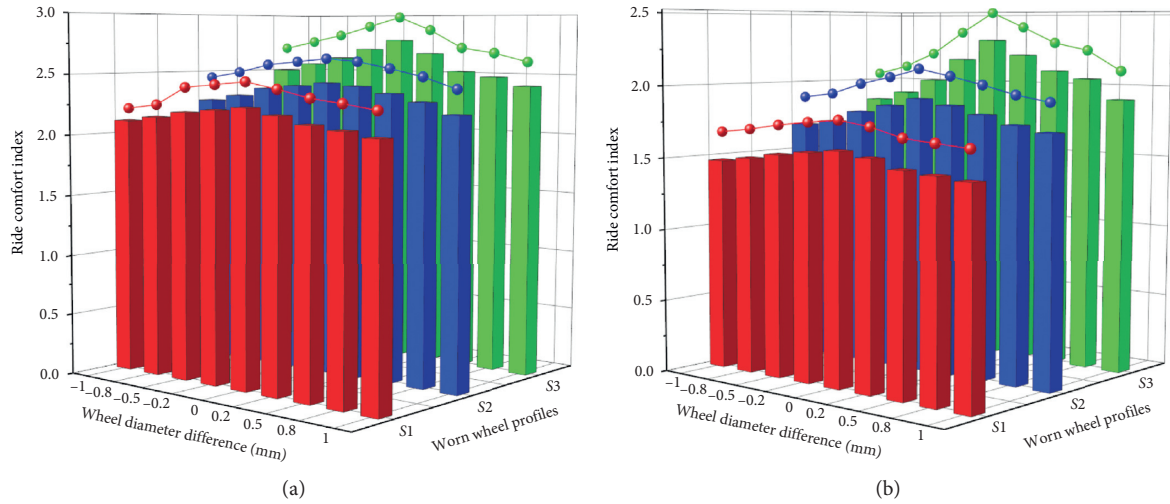
Figure 10: Ride comfort index. (a) Lateral ride comfort index. (b) Vertical ride comfort index.
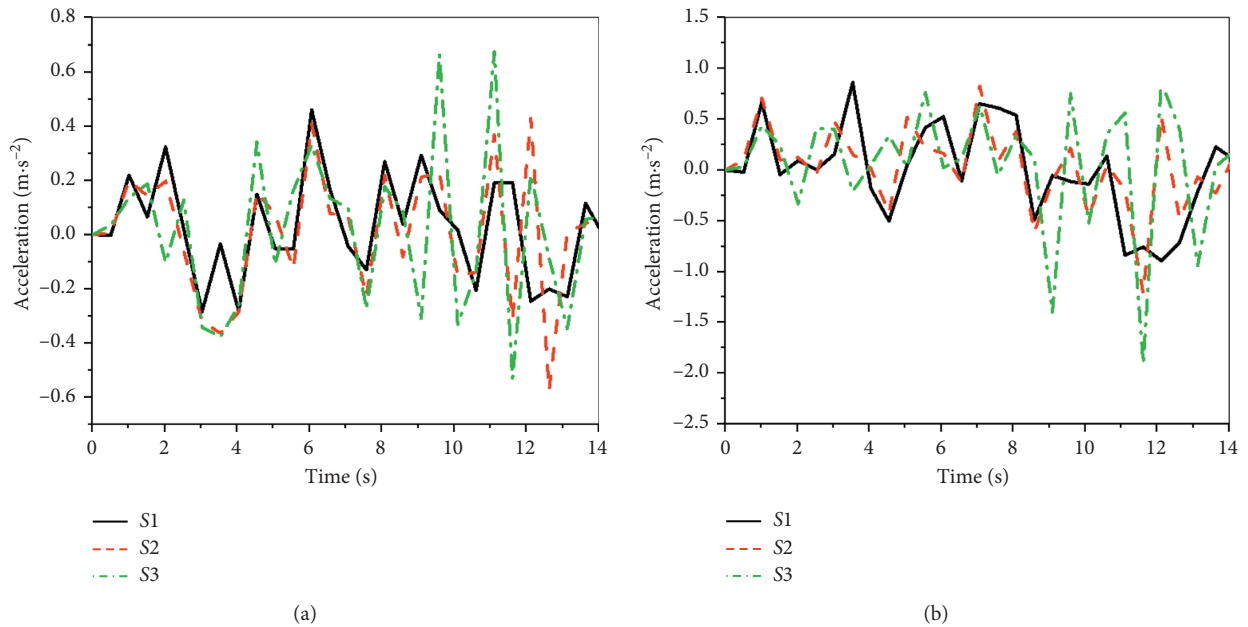
Figure 11: Vibration acceleration. (a) Vertical acceleration. (b) Lateral acceleration.

5. Influence of WPW Coupled with WDD on the Vehicle's Curve Negotiation Performance

Three worn wheel profiles for 5×10^4, 8×10^4, and 14×10^4 km traveled (denoted as $S1$, $S2$, and $S3$) and nine WDDs between −1 mm and +1 mm (Table 1) were set based on the measured data from the test vehicle, the same as in Section 4. Then, the vehicle dynamics model shown in Figure 6 was used to calculate and analyze the influence of WPW coupled with equivalent in-phase WDD on lateral wheel/rail contact force, derailment coefficient, axle lateral force, and wear index.

5.1. Wheel/Rail Lateral Force. Figure 12 shows the lateral wheel/rail contact force for different degrees of WPW coupled with different WDDs.

The following are shown in Figure 12:

(1) For a given WDD, the peak lateral wheel/rail contact force increased as the degree of WPW increased (i.e., as the wheel profile changed from $S1$ to $S2$ and then to $S3$). This increase was especially noticeable on outer wheels, where the lateral wheel/rail contact force was 1.67 times greater than that on inner wheels. Table 7 shows the increase in peak lateral wheel/rail contact force on outer wheels due to
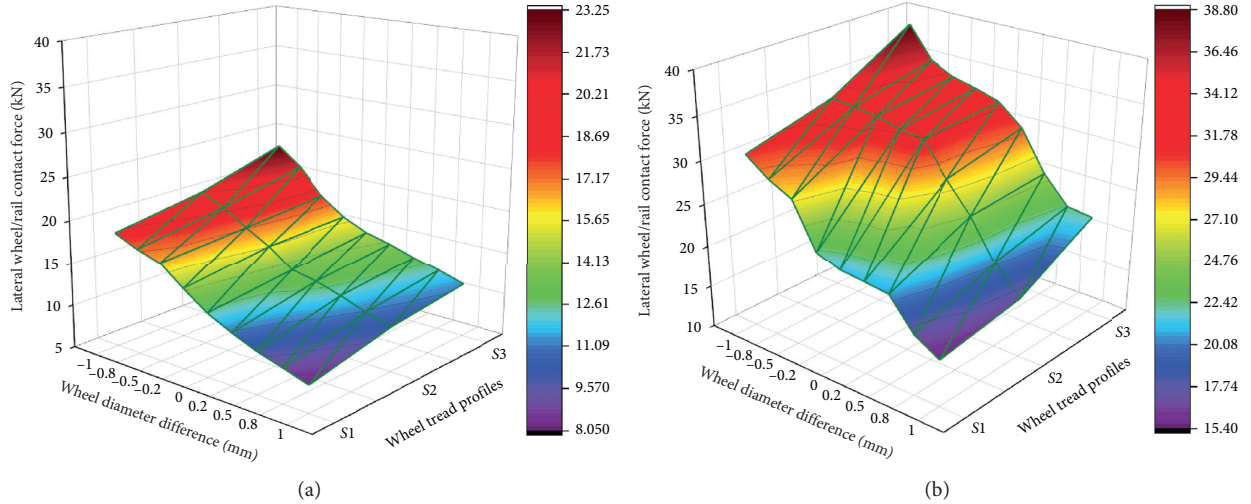
FIGURE 12: Lateral wheel/rail contact force. (a) Inner wheel (right wheel). (b) Outer wheel (left wheel).

TABLE 7: Increase in peak lateral wheel/rail contact force on outer wheels due to profile change from $S1$ to $S3$.

WDD	−1 (%)	−0.8 (%)	−0.5 (%)	−0.2 (%)	0 (%)	0.2 (%)	0.5 (%)	0.8 (%)	1 (%)
Increase	26.4	22.4	23.6	49.5	52.7	43.5	23.3	30.1	41.8

profile change from $S1$ to $S3$ for different WDD (−1, −0.8, −0.5, −0.2, 0, 0.2, 0.5, 0.8, and 1 mm).

(2) For different worn wheel profiles, the lateral wheel/rail contact force was relatively small when outer wheels had larger diameters than inner wheels' (WDD > 0). As can be seen in Table 7, the increase in lateral wheel/rail contact force for zero WDD was higher than those for nonzero WDD. This suggests that the presence of WDD reduced the peak lateral wheel/rail contact force and suppressed its increase due to profile change to some extent.

(3) When the larger-diameter wheels were on the inner side (i.e., WDD < 0), the lateral wheel/rail contact force was relatively larger. When a -1 mm WDD was coupled with profile $S3$, the peak lateral wheel/rail contact force on the outer wheels reached up to 38.74 kN, close to the safety limit of 41.29 KN.

After wheels began to wear, highly nonlinear contact occurred between wheel and rail and wheel/rail interaction deteriorated, significantly increasing the amplitude of the wheel/rail lateral force. As the presence of WDD caused lateral movement of the wheelset, the lateral creepage between wheel and rail tended to increase. When the larger-diameter wheels were on the inner side, the lateral creep was in the same direction as the centrifugal force. When the larger-diameter wheels were on the outer side, the lateral creep was in the opposite direction of the centrifugal force, thereby reducing the wheel/rail lateral force.

5.2. Derailment Coefficient. Figure 13 shows the derailment coefficient for different degrees of WPW coupled with different WDDs.

The following can be seen from Figure 13:

(1) For a given WDD, the derailment coefficient of both the left and right wheels increased with the increasing degree of WPW, and this trend was more marked for the outer wheel (left wheel). The increases in derailment coefficient due to profile change from $S1$ to $S3$ for different WDDs (−1, −0.8, −0.5, −0.2, 0, 0.2, 0.5, 0.8, and 1 mm) are presented in Table 8. It is clear that the increase in derailment coefficient grew sharply when the WDD reached 0.8 mm and 1 mm.

(2) When the larger-diameter wheels were on the outer side (i.e., WDD > 0), the derailment coefficient was relatively low, indicating that the vehicle's stability against derailment can be improved by positioning larger-diameter wheels on the outer side. When the larger-diameter wheels were on the inner side (i.e., WDD < 0), the derailment coefficient was relatively high. When a −1 mm WDD was coupled with the worn wheel profile $S3$, the peak derailment coefficient was 0.84, higher than the safety limit of 0.8.

(3) The derailment coefficient of outer wheels (left wheels) was higher, and its peak value was 1.91 times greater than inner wheels.

The variation pattern of derailment coefficient is similar to that of wheel/rail lateral force. This is because WPW and WDD have a greater effect on wheel/rail lateral

(a)

(b)
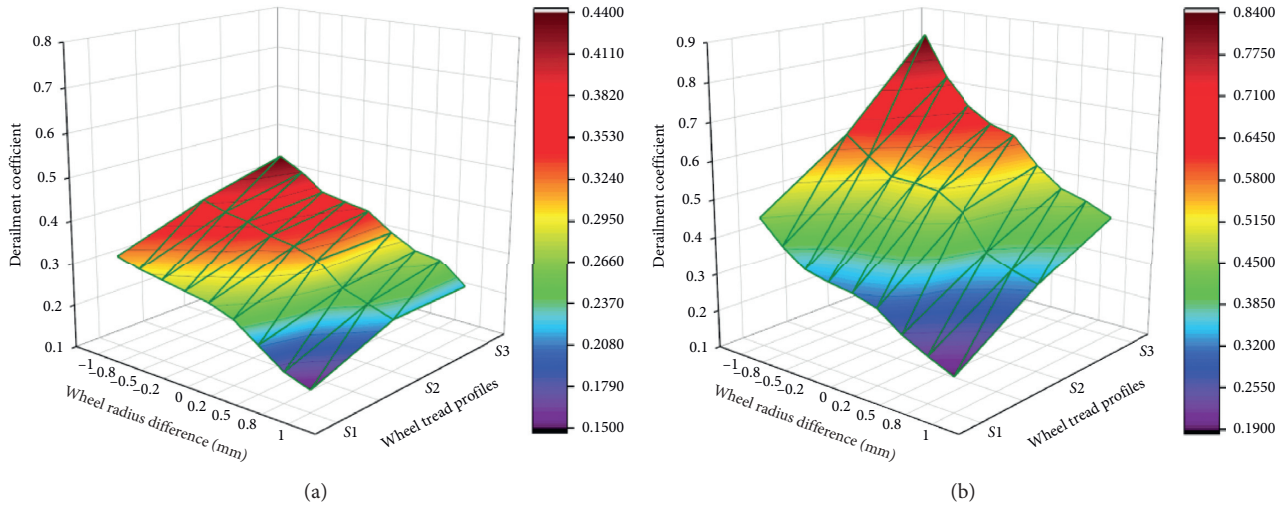
Figure 13: Derailment coefficient. (a) Inner wheel (right wheel). (b) Outer wheel (left wheel).

Table 8: Increase in peak derailment coefficient of outer wheels due to profile change from $S1$ to $S3$.

WDD	−1 (%)	−0.8 (%)	−0.5 (%)	−0.2 (%)	0 (%)	0.2 (%)	0.5 (%)	0.8 (%)	1 (%)
Increase	86.3	86.6	87.4	87.8	91	76.7	89.7	109.1	125.2

force than on wheel/rail vertical force, and derailment coefficient is the ratio of wheel/rail lateral force to wheel/rail vertical force.

5.3. Axle Lateral Force.
Figure 14 depicts the axle lateral force for different degrees of WPW coupled with different WDDs. As shown in the figure,

(1) For a given WDD, with the increase in the degree of WPW, the axle lateral force increased at a growing rate. The increases in axle lateral force due to profile change from $S1$ to $S3$ for different WDDs (−1, −0.8, −0.5, −0.2, 0, 0.2, 0.5, 0.8, and 1 mm) are presented in Table 9.

(2) It is clear from Figure 14 and Table 9 that as the WDD changed from -1 mm to 1 mm (i.e., as the difference between outer wheel diameter and inner wheel diameter increased), the magnitude and growth rate of axle lateral force declined at a decreasing rate. This suggests that when the outer wheel diameter was larger than the inner wheel diameter, the growth in axle lateral force due to increased profile wear was slowed down to some degree. If inner wheels had a greater diameter, the growth in axle lateral force would speed up.

(3) When a −1 mm WDD was coupled with worn wheel profile $S3$, the peak axle lateral force reached 37.51 kN, which approaches the safety limit of 37.75 kN. This suggests that the vehicle exerted relatively large lateral forces on the tracks in this case, which could cause lateral track movement and even derailment.
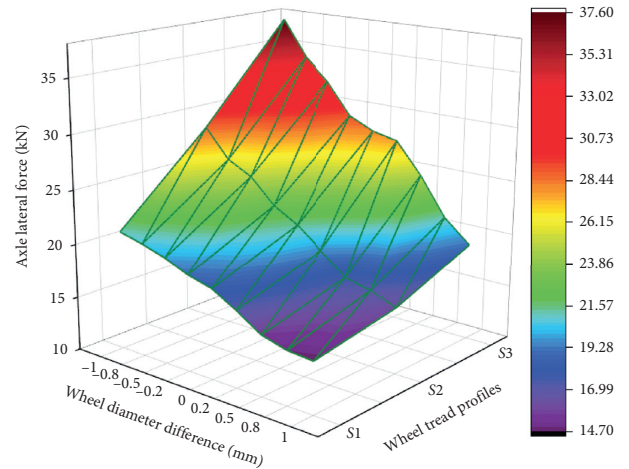
Figure 14: Axle lateral force.

Axle lateral force is mainly affected by the wheel/rail lateral force and also related to the force transferred from the bogie to the axle. The analysis results show that the variation law of axle lateral force is similar to that of wheel/rail lateral force.

5.4. Wear Index.
Elkins's wear index is calculated by summing the scalar products of creep force and creepage on all contact patches.

Figure 15 depicts the wear index for different degrees of WPW coupled with different WDDs.

The following can be seen from Figure 15:

TABLE 9: Increase in peak axle lateral force on outer wheels due to profile change from $S1$ to $S3$.

WDD	−1 (%)	−0.8 (%)	−0.5 (%)	−0.2 (%)	0 (%)	0.2 (%)	0.5 (%)	0.8 (%)	1 (%)
Increase	57.4	52.3	49.2	45.5	45.1	43.7	41.7	36.5	26.9
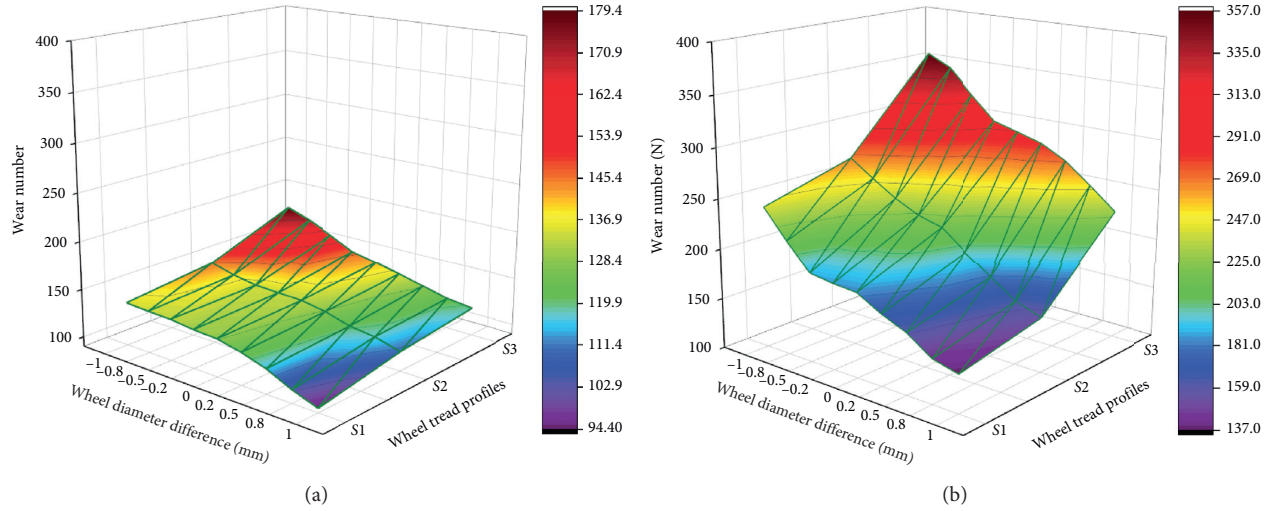
FIGURE 15: Wear index. (a) Inner wheel (right wheel). (b) Outer wheel (left wheel).

TABLE 10: Increase in the wear index of outer wheels due to profile change from $S1$ to $S3$.

WDD	−1 (%)	−0.8 (%)	−0.5 (%)	−0.2 (%)	0 (%)	0.2 (%)	0.5 (%)	0.8 (%)	1 (%)
Increase	47.9	61.6	70.1	60.6	58.4	66.6	68.9	74.6	67.1

(1) The wear index of both the left and right wheels increased with increasing degree of WPW. The outer (left) wheels had a greater wear index, and the peak wear index was about 1.99 times that of the inner wheels. Table 10 shows the increase in wear index of the outer wheels due to profile change from $S1$ to $S3$ for different WDDs (−1, −0.8, −0.5, −0.2, 0, 0.2, 0.5, 0.8, and 1 mm).

(2) When the larger-diameter wheels were on the outer side (i.e., WDD > 0), the wear index was relatively low, indicating that the resistance to wheel wear can be improved by positioning larger-diameter wheels on the outer side. When the larger-diameter wheels were on the inner side (i.e., WDD < 0), the wear index was relatively high. In the case where a −1 mm WDD was coupled with worn wheel profile $S3$, the wear index reached up to 356.78 N, indicating extremely severe wheel/rail wear.

As the degree of WPW increased, the wheel/rail interaction deteriorated and wheel/rail wear increased. When the inner wheels had a larger diameter than the outer wheels, the yaw angle and lateral creepage of the wheelset increased with increasing WDD and wheel/rail wear increased under the combined action of centrifugal forces.

6. Conclusions

Wheel profile wear and equivalent in-phase wheel diameter difference coexist on the studied subway line. This study investigated the influence of WPW coupled with WDD on vehicle dynamics, compared the dynamic responses of outer and inner wheels, and then analyzed the vehicle's dynamic performance for different positions of the larger-diameter wheels. The study can lead to the following conclusions:

(1) The dynamic performance of the vehicle during running on a straight line can be characterized as follows:

(i) In the presence of WPW coupled with WDD, the vehicle's ride comfort index decreased as the absolute value of WDD increased. This suggests that WDD can slow down the deterioration of ride comfort index caused by increasing WPW and improve the vehicle's ride comfort to some extent. However, the coupled damage reduced the critical speed and undermined hunting stability. The critical speed for the worn wheel profile for 14×10^4 km was lower than the maximum allowable speed for running on a straight line (100 km/h) when WDD was −1, −0.8, 0.8, and 1 mm.

(ii) Whether the larger-diameter wheels are on the inner side or outer side had little influence on the vehicle's critical speed and ride comfort index.

(2) The curve negotiation performance of the vehicle has the following characteristics:

(i) In the presence of WPW coupled with WDD, the vehicle showed increases in the lateral wheel/rail contact force, derailment coefficient, axle lateral force, and wear index and deterioration of curve negotiation performance when the larger-diameter wheels were on the inner side. When the larger-diameter wheels were on the outer side, the lateral wheel/rail contact force, derailment coefficient, axle lateral force, and wear index declined, indicating that the coupled damage can improve the vehicle's dynamic performance if the outer wheel diameter is larger than inner wheel diameter.

(ii) In the presence of WPW coupled with WDD, the outer wheels had significantly greater lateral wheel/rail contact force, derailment coefficient, and wear index compared to the inner wheels, and their peak values were 1.67, 1.91, and 1.99 times greater, respectively, than those on the inner side.

(iii) When the worn wheel profile for 14×10^4 kilometers traveled was coupled with -1 mm WDD, the peak lateral wheel/rail contact force and peak axle lateral force on the outer side reached up to 38.74 kN and 37.51 kN, respectively, which are close to corresponding safety limits. The peak derailment coefficient was 0.84, higher than the safety limit of 0.8. The wear index was as high as 356.78 N, indicating that the wheels were badly worn.

(3) During the maintenance of subway vehicles, the maintenance personnel should check the coupling of different types of wheel damage in addition to wheel damage detection. Moreover, special attention should be paid to the curve negotiation performance of outer wheels when the inner wheels have greater diameters than outer wheels. After the distance traveled reaches 14×10^4 km, the personnel should check whether the lateral wheel/rail contact force, derailment coefficient, and axle lateral force exceed the safety limits.

Data Availability

The data used to support the findings of this study are available from the first author upon request.

Conflicts of Interest

The authors declare that there are no conflicts of interest regarding the publication of this paper.

References

[1] D. Cui, L. Li, H. Wang, Z. Wen, and J. Xiong, "High-speed EMU wheel re-profiling threshold for complex wear forms from dynamics viewpoint," *Wear*, vol. 338-339, pp. 307–315, 2015.

[2] W. J. Lu, G. Q. Tao, P. Wang et al., "Influence of wheel wear on wheel-rail contact behavior and dynamic performance of metro vehicle," *Engineering Mechanics*, vol. 34, no. 08, pp. 222–231, 2017.

[3] Y. M. Yao, G. F. Li, and W. C. Ding, "Influences of wheel wear on dynamics performance of vehicles based on Archard model," *China Mechanical Engineering*, vol. 28, no. 19, pp. 2311–2317+2324, 2017.

[4] S. Pradhan, A. K. Samantaray, and R. Bhattacharyya, "Prediction of railway wheel wear and its influence on the vehicle dynamics in a specific operating sector of Indian railways network," *Wear*, vol. 406-407.

[5] Y. Sun, S. Y. Zhu, and W. M. Zhai, "Influence of tread hollow-worn wheel on wheel/rail interaction," *Journal of Mechanical Engineering*, vol. 54, no. 04, pp. 109–116, 2018.

[6] R. L. Zong, M. R. Hou, and H. M. Dai, "Study on impact of wheel rail wear on nonlinear critical speed of metro vehicles," *Modern Urban Transit*, vol. 7, pp. 56–60, 2018.

[7] H. L. Shi, S. Qu, D. F. Zhang et al., "Dynamic Response Performance Analysis of High-speed Trains on Track," *Journal of the China Railway Society*, vol. 41, no. 10, pp. 30–37, 2019.

[8] Q. Xiao, C. Li, C. Chang et al., "Research on Turnout Passing Performance of High-speed Train with Different Wheel Wear States," *Journal of the China Railway Society*, vol. 42, no. 08, pp. 51–59, 2020.

[9] L. Xu, D.L Cheng, C. Xu et al., "Effect of Wheel Wear on Dynamics Performance of 350 km/h EMU," *Science Technology and Engineering*, vol. 20, no. 17, pp. 7046–7051, 2020.

[10] J.P. Xie, Z. Y. Chen, Y. Pan et al., "Influence of wheel harmonic wear on wheel-rail vertical force and vehicle stability," *Journal of Central South University (Science and Technology)*, vol. 51, no. 07, pp. 2013–2020, 2020.

[11] L. Xu and W. M. Zhai, "Stochastic analysis model for vehicle-track coupled systems under joint random irregularities of wheel treads and track irregularities," *Journal of the China Railway Society*, vol. 42, no. 02, pp. 79–85, 2020.

[12] B. Liu and S. Bruni, "Influence of individual wheel profiles on the assessment of running dynamics of a rail vehicle by numerical simulation: a case study," *Vehicle System Dynamics*, pp. 1–20, 2021.

[13] K. K. Lyu, K. Y. Wang, and L. Ling, "Influence of wheel diameter difference on surface damage for heavy-haul locomotive wheels: Measurements and simulations," *International Journal of Fatigue*, vol. 132, pp. 1–10, 2020.

[14] S. G. Sun, L. N. Li, J. L. Zhou, and W. Li, "Influence of wheel diameter difference on safety and stationarity of vehicles crawling over the curved bridge," *Applied Mechanics and Materials*, vol. 209-211, pp. 2117–2120, 2012.

[15] Y. P. Jiang, M. R. Chi, C. Zhou et al., "Influence of Wheel Radius Difference Combination on the Dynamic Performance of Metro Vehicles," *Lubrication Engineering*, vol. 44, no. 10, pp. 115–120, 2019.

[16] S. Yan, Y. Jiang, and H. Wang, "Analysis of Influence of Wheel Diameter Difference on Safety Performance of Locomotive," *Journal of Chongqing University of Technology (Natural Science)*, vol. 33, no. 08, pp. 30–37, 2019.

[17] R. Chen, J. Y. Chen, P. Wang et al., "Effect of Wheel Diameter Difference on Wheel-rail Contact Geometry and Vehicle Running Behavior in Turnout Area," *Journal of the China Railway Society*, vol. 40, no. 05, pp. 123–130, 2018.

[18] W. Ma, R. M. Zou, and S. H. Luo, "Influence of Wheel Diameter Difference on Wheel/Rail Interaction of Locomotive under Coasting and Electric Braking Conditions," *Journal of Mechanical Engineering*, vol. 51, no. 14, pp. 115–121, 2015.

[19] C. Y. He, R. R Song, and W. H. Ma, "Influence of Wheel Diameter Difference to Wheel/rail Lateral Force of the Locomotive on Tangent Track," *Journal of Chongqing University of Technology(Natural Science)*, vol. 25, no. 07, pp. 57–63, 2011.

[20] C. Wang, W. H. Ma, S. H. Luo et al., "Study on Wheel Wear of the Subway Vehicle Based on Radius Difference," *Railway Locomotive & Car*, vol. 33, pp. 87–91, 2013.

[21] S. Y. Liu, Y. S. Xu, J. Zhang et al., "Influence of Wheel Diameter Difference on the Locomotive Dynamic Performance and Wheel Rail Contact," *Science Technology and Engineering*, vol. 17, no. 28, pp. 125–130, 2017.

[22] Z. C. Zhang, G. Li, G. F Chu et al., "Simulation Analysis of the Influence of Wheel Diameter Difference on the Locomotive Dynamic Performance," *Railway Locomotive & Car*, vol. 33, no. 02, pp. 11–16, 2013.

[23] M. R. Chi, W. H. Zhang, and J. Zeng, "Influence of wheel diameter difference on the stability of vehicle system," *China railway Science*, vol. 6, pp. 65–70, 2008.

[24] K. Evely, O. Peeter, and W. Gui, "Cubic Spline Histopolation," *Mathematical Modelling and Analysis*, vol. 22, pp. 514–527, 2017.

[25] R. Zou, W. Ma, and S. Luo, "Influence of the wheel diameter difference on the wheel/rail dynamic contact relationship of the heavy haul locomotive," *Australian Journal of Mechanical Engineering*, vol. 16, no. 2, pp. 98–108, 2018.

[26] N. N. Wang, S. H. Luo, and W. H. Ma, "Influence of wheel-diameter difference on dynamic curving performance of vehicle system," *Railway Locomotive & Car*, vol. 30, no. 02, pp. 47–49, 2010.

[27] Y. F. Zhang and J. Li, "Effect of wheel diameter difference on passing of small radius curve in mountainous track passenger train," *Journal of Huaqiao University(Natural Science)*, vol. 39, no. 04, pp. 489–495, 2018.

[28] R. H. Li, Y. Z. Song, and H. B. Xu, "Influence of initial wheel radius difference on the dynamic performance of high-speed train," *Railway Locomotive & Car*, vol. 2, pp. 14–18, 2015.

[29] P. Han, W. H. Zhang, Y. Li et al., "Influence of wheelset wear and wheel radius difference on dynamics performances of high-speed train," *Journal of Traffic and Transportation Engineering*, vol. 13, no. 06, pp. 47–53, 2013.

[30] A. Zhu, C. Fu, J. Yang et al., "Research on the wheel wear of metro vehicles based on the time-varying passenger flow," *Industrial Lubrication and Tribology*, vol. 71, no. 9, pp. 1038–1046, 2019.

[31] J. Wang, J. Yang, Y. Zhao, Y. Bai, and Y. He, "Nonsmooth dynamics of a gear-wheelset system of railway vehicles under traction/braking conditions," *Journal of Computational and Nonlinear Dynamics*, vol. 15, no. 8, 8 pages, 2020.

[32] X. M. Zhang, X. B. Xie, and S. B. Yang, "Author Index," *Vehicle Thermal Management Systems Conference and Exhibition (VTMS10)*, vol. 29, pp. 661–663, 2011.

[33] M. R. Chi, W. H. Zhang, J. Zeng et al., "Influence of wheel-diameter difference on running security of vehicle system," *Journal of Traffic and Transportation Engineering*, vol. 8, no. 5, 2008.

Research Article

Dynamic Model and Dynamic Response of Automobile Dual-Mass Flywheel with Bifilar-Type Centrifugal Pendulum Vibration Absorber

Lei Chen [iD],[1] Jianming Yuan [iD],[2] Hang Cai,[3] and Jinmin Hu[4]

[1]*School of Mechanical and Electronic Engineering, Wuhan University of Technology, Wuhan 430070, China*
[2]*School of Logistics Engineering, Wuhan University of Technology, Wuhan 430070, China*
[3]*HaiTong Investment Group, Chongqing 404100, China*
[4]*Shenzhen Road Rover Technology Co., Ltd, Shenzhen 518000, China*

Correspondence should be addressed to Jianming Yuan; whtu_yjm@163.com

Compared with dual-mass flywheel (DMF) and DMF with simple-type centrifugal pendulum vibration absorber (CPVA), DMF with bifilar-type CPVA has a better damping performance in the whole speed range of engine. The related research mainly focused on local models, such as dynamic model of DMF and dynamic model of CPVA, and the effect of the curvature path of CPVA on the damping performance. The reported models and methods are not sufficient for the system of DMF coupled with bifilar CPVA. Aiming at the deficiency of local models and the limitation of bench test, an integral model for DMF with bifilar CPVA is proposed and the real vehicle test is carried out in this study. Involving the moment of inertia of the centrifugal pendulum, the model considers the nonlinearities of DMF and bifilar CPVA. Afterward, the dynamic model of the automobile power transmission system equipped with the DMF with bifilar-type CPVA is built, and the dynamic responses of the system are investigated under idling and driving conditions. According to the simulation results, DMF with bifilar-type CPVA shows better vibration reduction performance in full-speed range. Moreover, the key structural parameters R and l influencing the damping performance of DMF with bifilar CPVA are discussed. The results show that the sum of R and l is directly proportional to the damping effect. Finally, real vehicle tests under idling and driving conditions (engine speed from 750 r/min to 3400 r/min) are carried out. The test results show that the 2nd order engine speed fluctuations are attenuated by more than 80% by DMF with bifilar CPVA with engine speed lower than 2000 r/min and are attenuated by more than 90% with engine speed higher than 2000 r/min. The experimental results are basically consistent with the simulation results, which verify the validity of the model.

1. Introduction

There are many sources of vehicle vibrations and noises, such as the engine, the tire, the transmission, and the road surface [1], in which the engine contributes the most [2]. In addition, the vibrations and noises caused by the engine will further produce transmission vibrations and noises [3]. Global emission regulation requires the automotive manufacturers to develop engines with lower level emissions. The development of the turbocharged three-cylinder engine is a strategy to meet this goal. However, the natural structural characteristics bring a greater challenge on NVH performance than the four-cylinder engine [4]. In order to attenuate the torsional vibrations caused by the engine, torsional vibration dampers are employed to vehicle power transmissions.

Palliative devices, such as clutch predampers and dual-mass flywheel, have been used to mitigate the effect of transmitted engine torsional oscillations [5]. Equipping a clutch predamper (CTD) is the traditional way to attenuate the torsional vibration of the powertrain. However, limited by the space and the large stiffness of the elastic element, the damping effect is poor [6]. As a new kind of automobile torsional damper, DMF (dual-mass flywheel) has the

functions of the single-mass flywheel and the CTD [7]. With reasonable mass distribution and torsional stiffness, a DMF can reduce the natural frequency of the powertrain below the common speed and thus attenuate the torsional vibrations under idling and driving conditions [8]. The circumferential long arc spring-type DMF is the most widely used, and the technology is the most mature [9]. The structural characteristics and working principle of DMF determine that the DMF is suitable for low-speed vibration reduction, but the damping performance of the DMF in the high-speed region is decreased [10].

The natural frequency of the centrifugal pendulum damper (CPVA) is related to the rotational speed, which shows excellent damping performance in the whole speed range and has been widely used in the aviation field [11]. The centrifugal pendulums have been applied to the large torsional angle clutch and DMF since 2008, which can attenuate the vibration of the main harmonic excitation of the engine. Cirelli [11] analyzed the variation law of velocity and acceleration of a parallel and trapezoidal bifilar centrifugal pendulum from the perspective of kinematics. Accordingly, a linear dynamic model of bifilar centrifugal pendulum was developed. Some studies by Li Wei and Long Yan [12] suggested that the natural frequency of a DMF with CPVA was proportional to the rotating speed, and the vibration of engine fire frequencies could be absolutely eliminated theoretically by adjusting the parameters of the centrifugal pendulum. Wu Huwei and Wu Guangqiang [13] found that the large angular clutch with CPVA could reduce not only the natural frequency of the vehicle powertrain but also the torsional vibration amplitude of the engine. Hässler and Kooy [14] experimentally investigated the damping performance of a DMF and a clutch with CPVA. They discovered that the clutch with CPVA showed a better damping performance than the DMF in the speed region above 2000 r/min, whereas the result was reversed when the engine speed was below 2000 r/min. Seong-Young Song [15] established a linear dynamic model of a clutch with simple CPVA. The model was employed to analyze the dynamic response, and the results showed that the clutch with CPVA could attenuate the torsional vibration of vehicle powertrain. The experimental results also demonstrated the finding. Chen Long and Shi Wenku [16] created the simulation models of DMF, clutch, and DMF with CPVA, and they found the DMF with CPVA possessed the best damping performance. Rao and Sujatha [17] proposed the design strategy to reduce the 1st and 2nd order axial vibrations by using circular path pendulum absorbers and analytically solved the equations of motion at the 2nd order. The authors in [18] analyzed the stability of a simple CPVA and a bifilar CPVA from the perspective of kinematics. They found that the simple CPVA was prone to instability due to the large swing angle in the high-speed range, while the bifilar CPVA showed a better angle constraint and better stability. Shi and Parker [19] developed an analytical model of CPVA systems with equally spaced, identical absorbers and investigated the structure of the modal vibration properties, and then, the critical speeds and flutter instability of the system were studied numerically and analytically based on the model.

Marco Cirelli et al. [20] applied the methodology of Desoyer and Slibar to solve the dynamics of the centrifugal pendulum with cycloidal and epicycloidal pendulum paths, and the numerical simulations confirmed the better damping capabilities of the cycloidal and epicycloidal centrifugal pendula with respect to the classic circular path. Mayet and Ulbrich [21] proposed a general approach for the design of tautochronic pendulum vibration absorbers, and the method could deal with a large variety of nonbifilar centrifugal vibration absorber designs, which provide application-related optimal performance and resolve some of the existing design limitations. The authors in [22] provided an analytical proof of the optimal tuning of centrifugal pendulum vibration absorbers (CPVAs) to reduce in-plane translational and rotational vibration for a rotor with N cyclically symmetric substructures attached to it, and the solutions showed that the rotor translational vibration at order j was reduced when one group of CPVAs was tuned to order j_{N-1} and the other was tuned to order j_{N+1}. Pier Paolo Valentin and Marco Cirelli et al. [23] analyzed a methodology for designing compliant centrifugal dampers based on the arrangement of a collection of leaf flexure hinges connecting peripheral masses. The pseudorigid surrogate model was deduced taking into account second-order kinematic invariants and Euler–Savary equations, thus providing second-order approximation of the relative motion.

The above literatures show that the natural frequency of the centrifugal pendulum torsional damper is correlated with the engine speed. In addition, the harmonic order of the torsional vibration can be tuned when the ratio of l to R is equal to a certain harmonic order of the engine, in which l is the distance of the center of mass to the suspension point of the CPVA and R represents the distance of the connecting point of the CPVA to the rotating center. It is clear that a number of the combinations of l and R can meet the above tuning requirement. Therefore, whether the different combinations of l and R affect the damping performance needs to be discussed. Both DMF and CPVA show nonlinear dynamic characteristics. When they are combined together, the dynamic model of the whole system should consider their dynamic characteristics. Since the damping performance should be observed in the powertrain system, the dynamic model of the powertrain system equipping the DMF with CPVA should be developed. Recently, the CPVA and DMF are usually studied separately. Furthermore, most of the studies focus on local linear models of the CPVA, and the studies focusing on the dynamic responses of the powertrain involving CPVA are rarely mentioned. During the operation of the CPVA, some literatures [12] suggested that the moment of inertia could be neglected when modeling CPVA since the mass was so tiny. Nevertheless, the mass of the bifilar CPVA can theoretically be designed to be larger than that of the simple CPVA [18]; hence, the moment of inertia of the bifilar CPVA cannot be neglected. In the aspect of model validation, most of the research studies only give numerical simulation, bench test for local model of a shock absorber, and low-speed vehicle test.

According to the research results of the above literatures, there are two main problems that need to be supplemented,
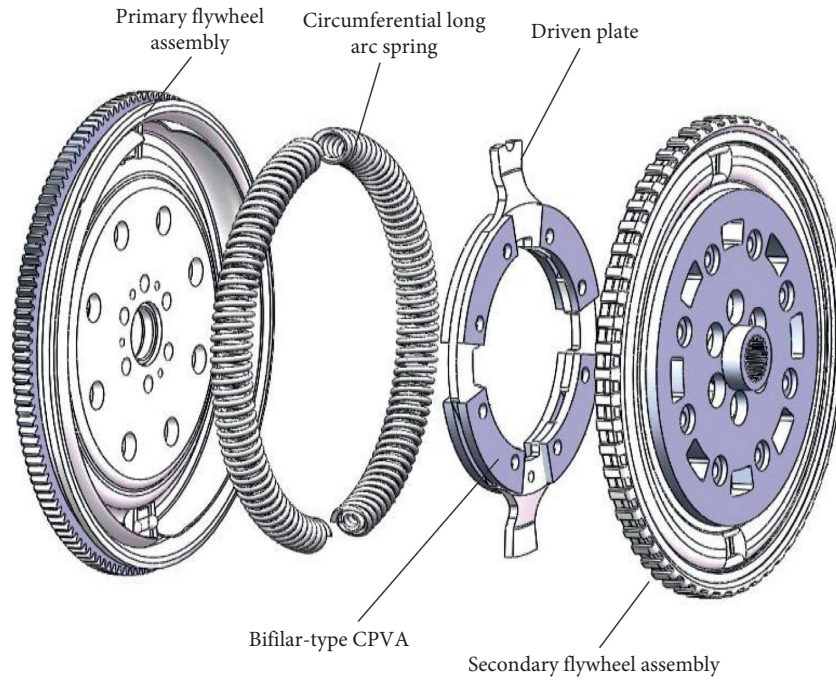
Figure 1: Schematic diagram of the DMF with bifilar CPVA.
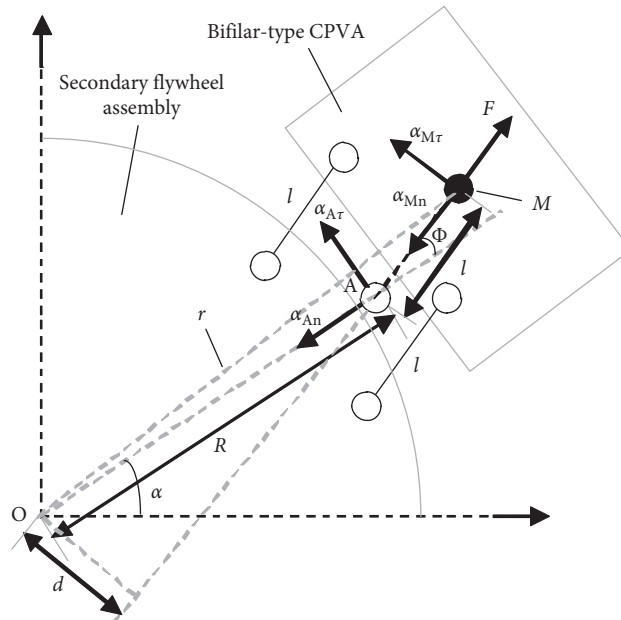
Figure 2: Simplified model of the bifilar CPVA. O: rotary center of the secondary flywheel; A: equivalent connection point of the CPVA; M: center of mass of CPVA; α: rotation angle of the secondary flywheel; ϕ: the swing angle of the CPVA relative to the secondary flywheel; R: distance between the equivalent connecting point of the CPVA and the rotary center of secondary flywheel; l: distance from the equivalent connecting point of the CPVA to its centroid; F: centrifugal force of the CPVA; d: force arm of centrifugal force; r: distance from the centroid of the CPVA to point; m: mass of the bifilar CPVA.

that is, the dynamic model of DMF with bifilar CPVA and the model validation. As for the dynamic model of DMF with bifilar CPVA, there are few published literatures about DMF and CPVA as an ensemble; in fact, DMF and CPVA need to be analyzed as an entirety, which means the integral dynamic model should contain the dynamic models of DMF

and bifilar CPVA. Moreover, the different combinations of l and R affecting the damping performance must be discussed. With regard to model validation, numerical simulation, bench test for local model of a shock absorber, and low-speed vehicle test were applied to verify the dynamic model in the above literatures; theoretically, it is more sufficient

that the real vehicle experiment covering full working speed of engine as far as possible is used to verify the effectiveness of the model.

The objective of this study is to establish the integral dynamic model of the powertrain matching DMF with bifilar CPVA and consummate the model validation. Firstly, a nonlinear integral dynamic model involving the moment of inertia of the CPVA, the nonlinearity of bifilar CPVA, and the nonlinearity of DMF is developed. Then, the model is used in modeling the automobile power transmission system. Additionally, the damping performance of the DMF with bifilar CPVA is theoretically investigated, and the influence of different combinations of R and l on the damping performance is discussed. Finally, the model is validated by real vehicle tests covering the full working speed range of engine (from 750r/min to 3400r/min).

2. Linear Dynamic Model of Secondary Flywheel with a Bifilar CPVA

A basic DMF consists of two separated flywheel assemblies connected by a spring-damping damper, as shown in Figure 1. The primary flywheel assembly mainly includes a starting gear ring, a signal ring, a cover, and a primary flywheel. The secondary flywheel assembly mainly comprises a driven plate, a seal disc, and a secondary flywheel. The primary assembly is connected to the engine crankshaft, and the secondary assembly is connected to the clutch. Thus, power from the engine can be initially transmitted to the primary assembly and then to the secondary assembly by compressing the arc springs through the driven plate. Finally, the power reaches the power transmission leading to car driving. As shown in Figure 1, on the basis of the structure of the DMF, the bilifar CPVAs are symmetrically installed on the driven plate in circumferential direction.

With reference to Figure 2, the dynamic equations for the bifilar-type CPVA have been deduced as follows:

$$a_{A\tau} = R\ddot{a}, \tag{1}$$

$$a_{An} = R\dot{a}^2, \tag{2}$$

$$a_{M\tau} = l(\ddot{a} + \ddot{\phi}), \tag{3}$$

$$a_{Mn} = l(\dot{a} + \dot{\phi})^2, \tag{4}$$

where $a_{A\tau}$ and $a_{M\tau}$ denote the tangential acceleration of A and M relative to A, respectively, and a_{An} and a_{Mn} represent the normal acceleration of A and M relative to A, respectively.

The absolute tangential acceleration of $M \cdot a_{M\tau}^0$ can be expressed as follows [18, 19]:

$$a_{M\tau}^0 = a_{M\tau} + a_{A\tau} \cos(\phi) + a_{An} \sin(\phi). \tag{5}$$

Combining equations (1), (2), (3), and (4) with equation (5), $a_{M\tau}^0$ can be rewritten as

$$a_{M\tau}^0 = l(\ddot{a} + \ddot{\phi}) + R\ddot{a} \cos(\phi) + R\dot{a}^2 \sin(\phi). \tag{6}$$
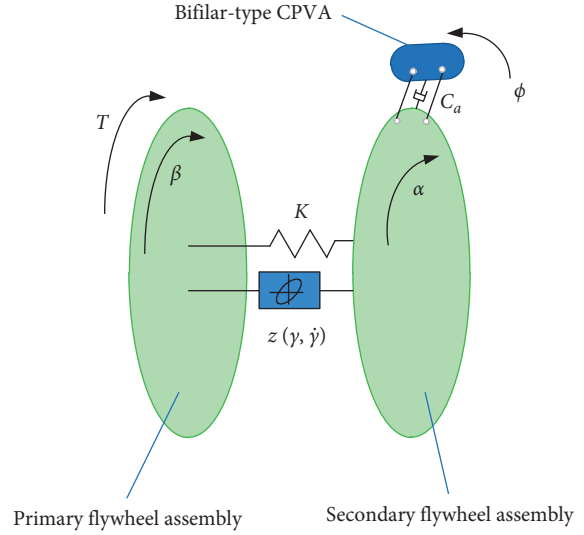

FIGURE 3: Dynamic model of the DMF with a bifilar-type CPVA.
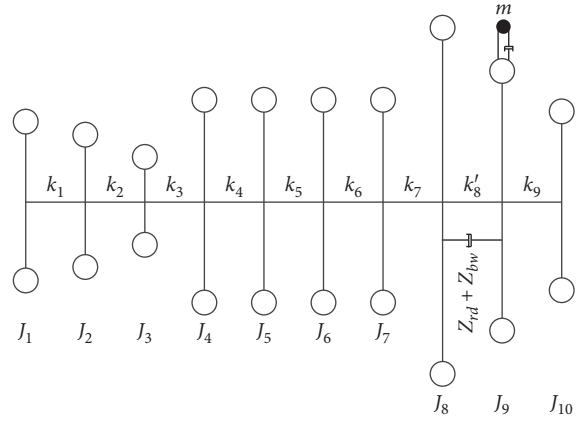
FIGURE 4: Torsional vibration model of power transmission under the idling condition.
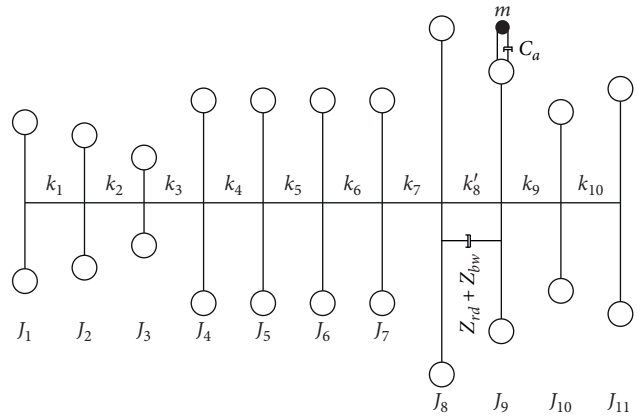
FIGURE 5: Torsional vibration model of power transmission under the driving condition.

Thus, the equation of motion of the bilifar CPVA can be given by

TABLE 1: Structural parameters of the power transmission.

Names of elements	Inertia	Value of inertia (Kg•m^2)	Torsional stiffness	Value of torsional stiffness (N•m/rad)
Driven part of rubber damper	J_1	4.795E − 3	K_1	14320
Driving part of rubber damper	J_2	2.038E − 3	K_2	74636
Accessories	J_3	9.74E − 5	K_3	356181
Cylinder 1	J_4	4.715E − 3	K_4	358936
Cylinder 2	J_5	4.712E − 3	K_5	361005
Cylinder 3	J_6	4.712E − 3	K_6	359750
Cylinder 4	J_7	4.69E − 3	K_7	1872000
Primary flywheel assembly	J_8	0.075	K'_8	165 (under idling condition); 750 (under driving condition)
Secondary flywheel assembly	J_9	0.0125	K_9	99213
Input shaft of gearbox	J_{10}	7.312E − 3	K_{10}	48650
Transmission shaft system	J_{11}	0.02684		

TABLE 2: Model parameters of the DMF with the bifilar CPVA.

Names of elements	Value	Unit	Remark
R	76	mm	
l	19	mm	
m	1	Kg	
I	0.004	Kg.m^2	
C_a	0.1	N•m/(rad/s)	
C_s	0.1	N•m/(rad/s)	
μ	−0.1022	Null	
λ	0.59185	Null	
η	5.1488	Null	
	0.24975	Null	Engine speed < 1000 r/min
b	0.4002	Null	1000 r/min ≤ engine speed < 2000 r/min
	0.49455	Null	Engine speed ≥ 2000 r/min
C	2.85	Null	

TABLE 3: Simulation algorithm.

Algorithm
Step 1: identify parameters of the Bouc–Wen model $(\mu, \lambda, \eta, \mathbf{b}, \mathbf{c})$ from equation (27) based on test data and then obtain $\mathbf{Z}(\gamma, \dot{\gamma})$
Step 2: prepare parameters in Tables 1 and 2, engine speed ω_e, and excitation torque T_1, T_2, T_3, T_4
Step 3: construct the vector Y of state variables of the system $\mathbf{Y} = \begin{bmatrix} \alpha_1 \\ \dot{\alpha}_1 \\ \vdots \\ \phi \\ \dot{\phi} \\ \vdots \\ \alpha_{11} \\ \dot{\alpha}_{11} \end{bmatrix}$
Step 4: establish the system state equation from equations (45) and (46)
Step 5: use Runge–Kutta algorithm to solve the system state equation in Matlab software platform

$$m\left(l(\ddot{a} + \ddot{\phi}) + R\ddot{a}\cos(\phi) + R\dot{a}^2 \sin(\phi)\right) = mg \sin(\phi). \quad (7)$$

Because the secondary flywheel rotary speed is approximately equal to the engine rotary speed, that is, $R\dot{a}^2 \gg g$, then equation (7) can be reduced as

$$l\ddot{\phi} + (l + R \cos(\phi))\ddot{a} + R\dot{a}^2 \sin(\phi) = 0. \quad (8)$$

Assume that the average rotary speed of the secondary flywheel is μ. Suppose that the amplitude and frequency of

the rotary speed fluctuation of the secondary flywheel are A_0 and ω, respectively. The rotation angle of the secondary flywheel is expressed as

$$a = \mu t + A_0 \sin(\omega t). \quad (9)$$

Assuming that A_0 and Φ are tiny, then $\dot{a} \approx \mu$, $\sin(\phi) \approx \phi$ and $\cos(\phi) \approx 1$; equation (8) can be obtained as

$$\ddot{\phi} + \frac{R}{1}\mu^2 \phi \frac{(1 + R)}{1} A_0 \omega^2 \sin(\omega t). \quad (10)$$
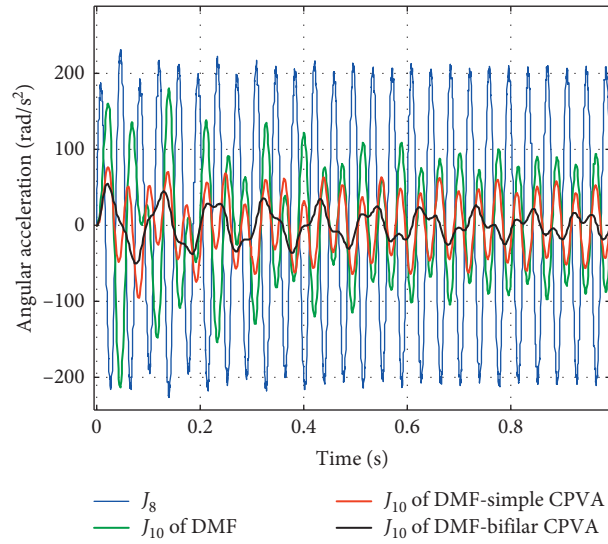
FIGURE 6: Angular acceleration curves of J_8 and J_{10} under the idling condition.

(a)

(b)

(c)

(d)
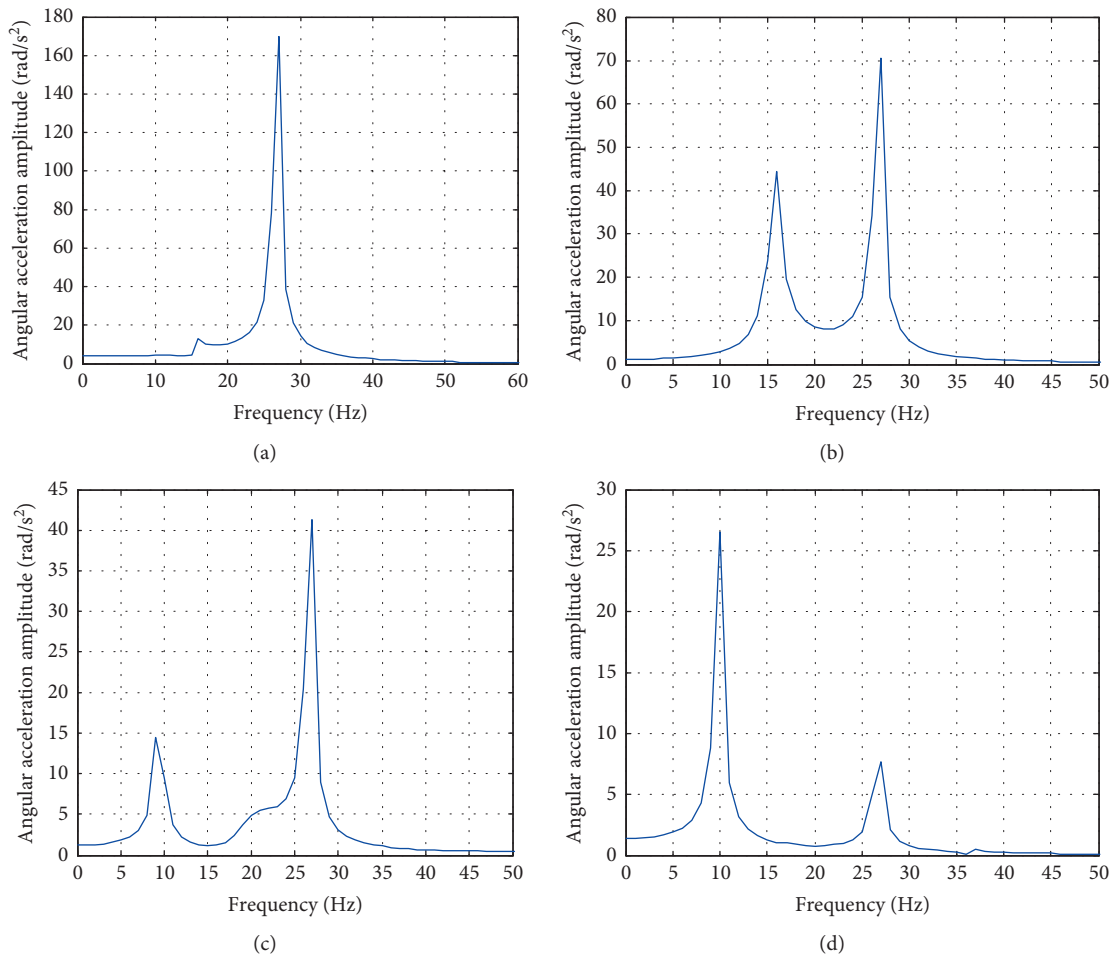
FIGURE 7: Spectra of J_8 and J_{10} under the idling condition. (a) spectrum of J_8 and (b) spectrum of J_{10} of DMF; (c) spectrum of J_{10} of DMF with simple CPVA; (d) spectrum of J_{10} of DMF with bifilar CPVA.
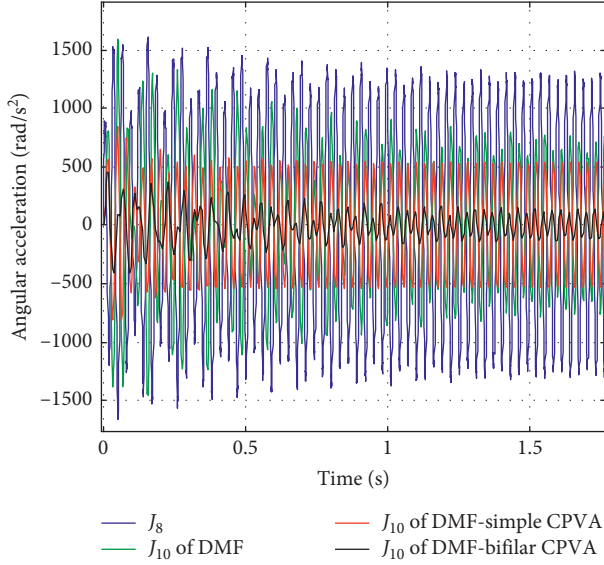
FIGURE 8: Angular acceleration curves of J_8 and J_{10} at 1000 r/min of engine speed.

FIGURE 10: Angular acceleration curves of J_8 and J_{10} at 2000 r/min of engine speed.

FIGURE 9: Angular acceleration curves of J_8 and J_{10} at 1500 r/min of engine speed.
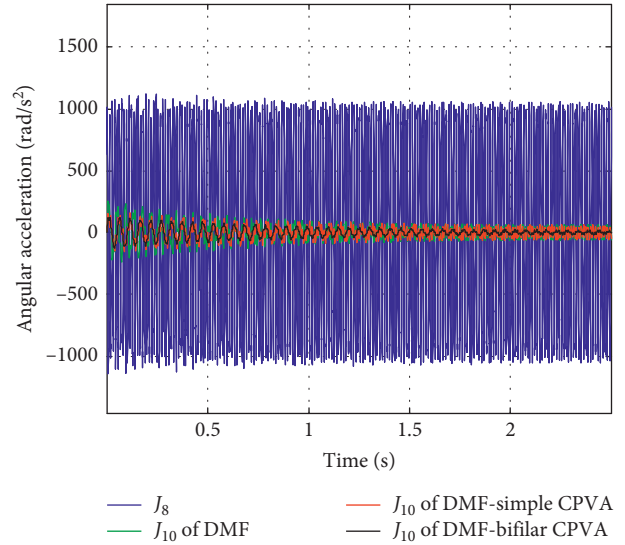
FIGURE 11: Angular acceleration curves of J_8 and J_{10} at 2500 r/min of engine speed.

The steady-state solution of equation (10) is expressed as

$$\ddot{\phi} = \frac{R+l}{R\mu^2 - l\omega^2} A_0 \omega^2 \sin(\omega t) = -\frac{R+l}{R\mu^2 - l\omega^2} \ddot{a}. \quad (11)$$

Also, the natural frequency of the bifilar CPVA ω_n can be given by

$$\omega_n = \mu \sqrt{\frac{R}{l}}. \quad (12)$$

Referring to Figure 2, the centrifugal torque T acting on the secondary flywheel by the bifilar CPVA can be described as

$$T = m(\dot{a} + \dot{\phi})^2 r \ d, \quad (13)$$

where

$$r = \sqrt{R^2 + l^2 - 2Rl \ \cos(\pi - \phi)}. \quad (14)$$

$$d = R \ \sin(\phi). \quad (15)$$

Let $\sin(\phi) \approx \phi$, $\cos(\phi) \approx 1$, $\dot{\alpha} \approx \mu$, $\mu \gg \dot{\phi}$, $\dot{\alpha} \gg \dot{\phi}$, then
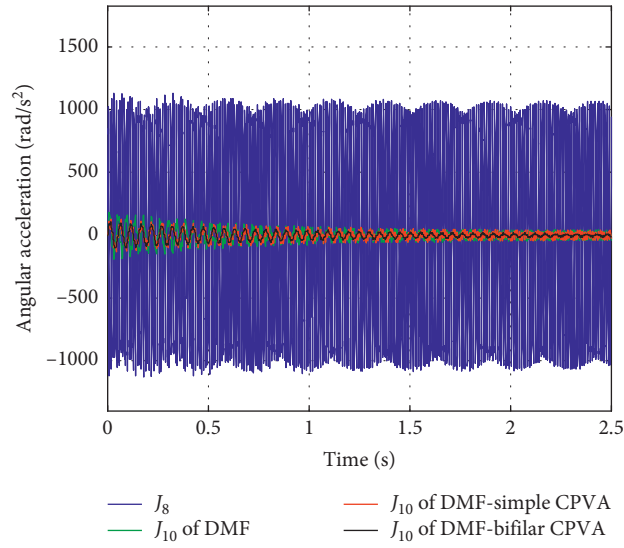
FIGURE 12: Angular acceleration curves of J_8 and J_{10} at 3000 r/min of engine speed.

(a)

(b)

(c)

(d)
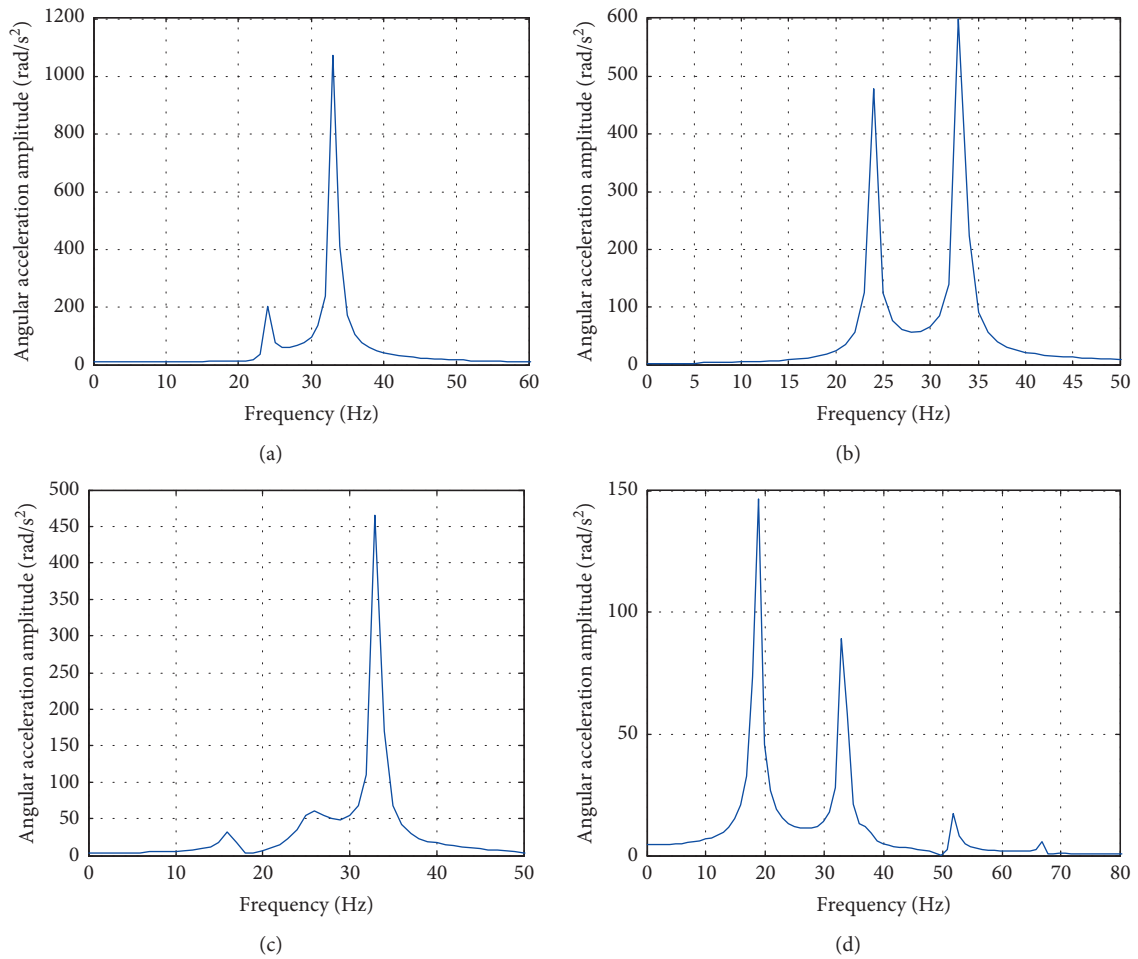
FIGURE 13: Spectra of J_8 and J_{10} at 1000 r/min of engine speed: (a) spectrum of J_8 and (b) spectrum of J_{10} of DMF; (c) spectrum of J_{10} of DMF with simple CPVA; (d) spectrum of J_{10} of DMF with bifilar CPVA.
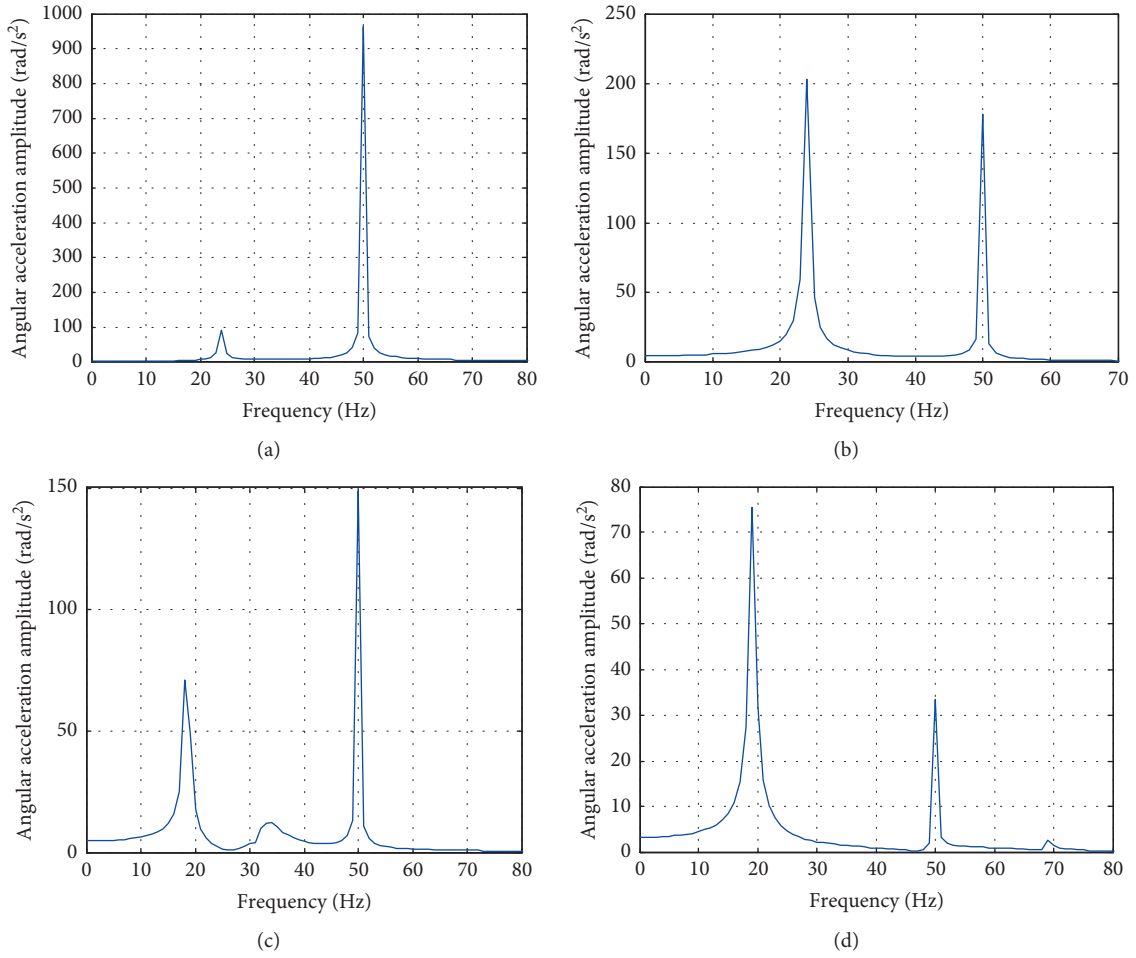
FIGURE 14: Spectra of J_8 and J_{10} at 1500 r/min of engine speed: (a) spectrum of J_8 and (b) spectrum of $J10$ of DMF; (c) spectrum of $J10$ of DMF with simple CPVA; (d) spectrum of $J10$ of DMF with bifilar CPVA.
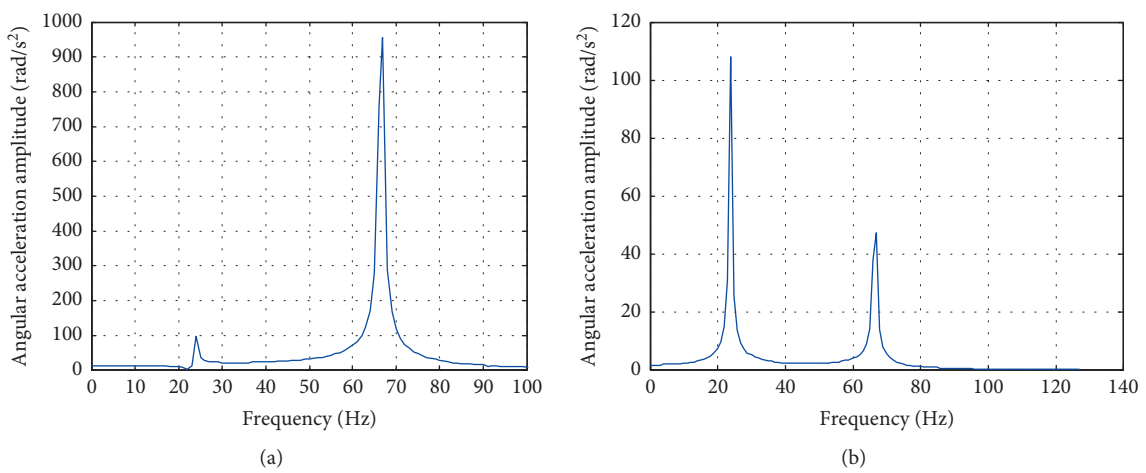
FIGURE 15: Continued.
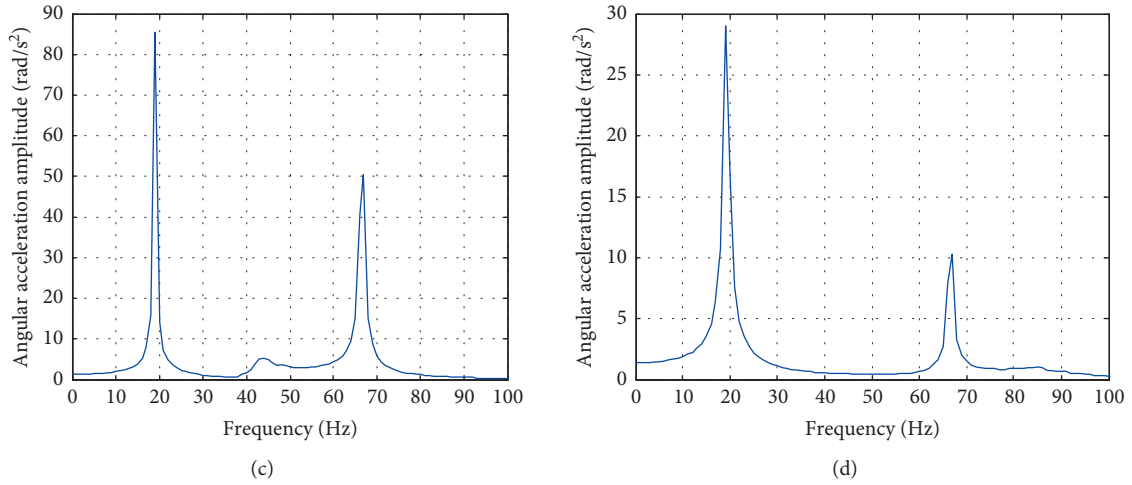
FIGURE 15: Spectra of J_8 and J_{10} at 2000 r/min of engine speed: (a) spectrum of J_8 and (b) spectrum of J_{10} of DMF; (c) spectrum of J_{10} of DMF with simple CPVA; (d) spectrum of J_{10} of DMF with bifilar CPVA.
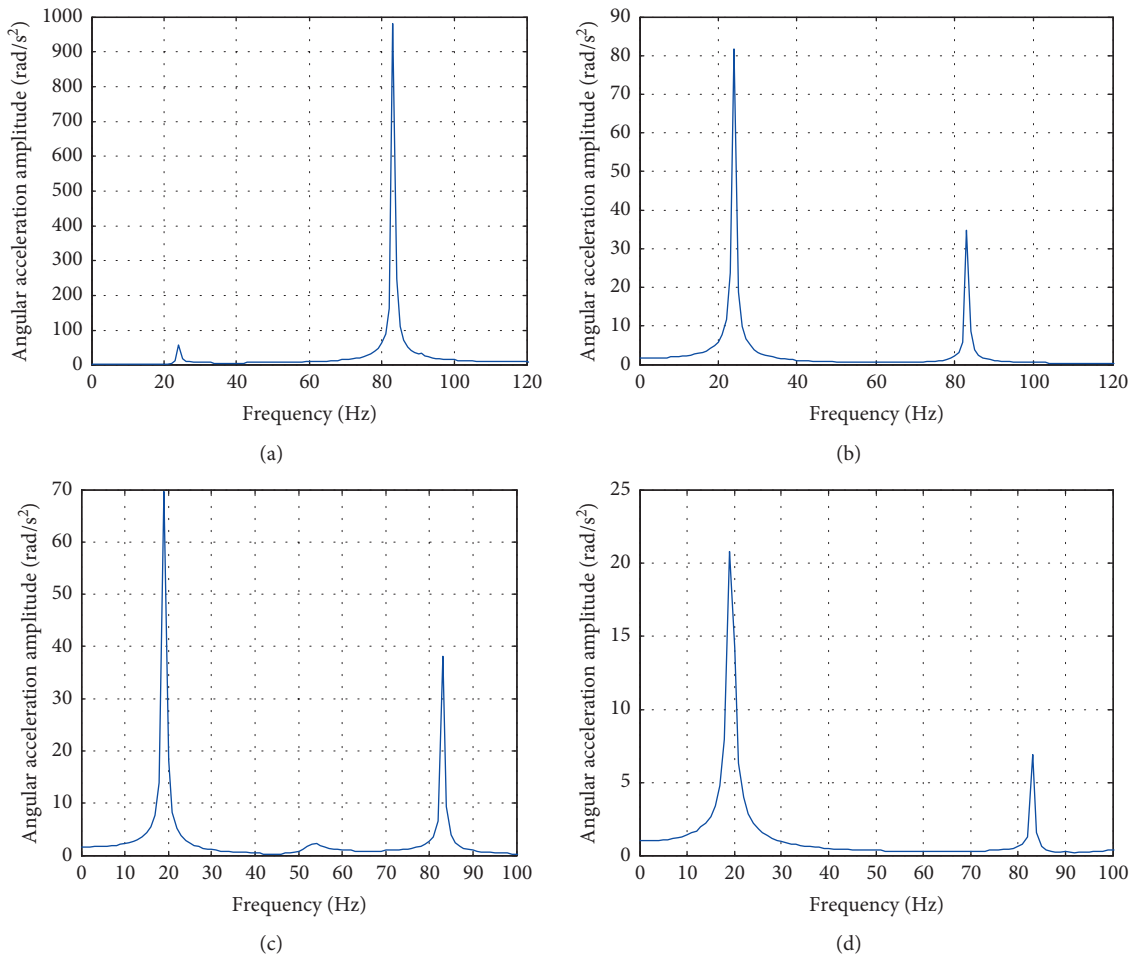
FIGURE 16: Spectra of J_8 and J_{10} at 2500 r/min of engine speed: (a) spectrum of J_8 and (b) spectrum of J_{10} of DMF; (c) spectrum of J_{10} of DMF with simple CPVA; (d) spectrum of J_{10} of DMF with bifilar CPVA.

$$T = m(R + l)\mu^2 R\phi. \tag{16}$$

By substituting equation (11) into equation (16), we can get

$$T = -\frac{m(R + l)^2}{1 - (\omega/\mu)2(l/R)}\ddot{\alpha}. \tag{17}$$

According to equation (17), the equivalent moment of inertia of the bifilar CPVA J_e is shown as

$$J_e = -\frac{m(R + l)^2}{1 - (\omega/\mu)2(l/R)}. \tag{18}$$

Let the excitation harmonic order of the engine be ε, then

$$\frac{\omega}{\mu} = \varepsilon. \tag{19}$$

If

$$1 - \left(\frac{\omega}{\mu}\right)^2 \frac{l}{R} = 0, \tag{20}$$

then $J_e = \infty$. In this case, ε meets the following condition:

$$\varepsilon = \sqrt{\frac{R}{l}}. \tag{21}$$

Based on the above discussion, the natural frequency of the bifilar CPVA is related to the engine speed, which means that the bifilar CPVA can attenuate the torsional vibration in full speed range of engine. When $\sqrt{(R/l)}$ is equal to ε by adjusting the ratio of R and l, the bifilar CPVA is equivalent to a flywheel with infinite moment of inertia; that is, the εth harmonic-order torque fluctuation from the engine can be theoretically eliminated completely by the bifilar CPVA.

3. Nonlinear Dynamic Model of DMF with a Bifilar CPVA

3.1. Nonlinear Dynamic Model of DMF.
The mechanical model of the DMF with a bifilar CPVA is shown in Figure 3, in which the moment of inertia and the angular displacement of the primary flywheel assembly are J_p and β, respectively; the moment of inertia and the angular displacement of the secondary flywheel assembly are J_s and α, respectively; the moment of inertia of the bifilar CPVA is I; the torsional stiffness of the DMF is K; and the damping coefficient of the bifilar CPVA is C_a.

During the operation of the DMF, the friction between the spring and slide contains Coulomb friction and viscous friction, which characterizes hysteresis nonlinearity [10]. The author of this paper has created the nonlinear dynamic model of the DMF [24], in which the improved Bouc–Wen model was used to describe the nonlinear hysteresis torque. The dynamic equations of the DMF have been deduced as follows:

$$\begin{bmatrix} J_p & 0 \\ 0 & J_s \end{bmatrix}\begin{bmatrix} \ddot{\beta} \\ \ddot{\alpha} \end{bmatrix} + \begin{bmatrix} K & -K \\ -K & K \end{bmatrix}\begin{bmatrix} \beta \\ \alpha \end{bmatrix} + \begin{bmatrix} Z(\gamma, \dot{\gamma}) \\ -Z(\gamma, \dot{\gamma}) \end{bmatrix} = \begin{bmatrix} T \\ 0 \end{bmatrix}, \tag{22}$$

$$\gamma(t) = \beta(t) - \alpha(t), \tag{23}$$

$$Z(\gamma, \dot{\gamma}) = Z_{r\,d}(\dot{\gamma}) + Z_{bw}(\gamma, \dot{\gamma}), \tag{24}$$

$$Z_{r\,d}(\dot{\gamma}) = C_s \cdot |\dot{\gamma}|^b \cdot \text{sign}(\dot{\gamma}), \tag{25}$$

$$\begin{aligned} Z_{bw}(\gamma, \dot{\gamma}) = \eta \cdot \dot{\gamma}(t) - \lambda \cdot |\dot{\gamma}(t)| \cdot Z_{bw}(\gamma, \dot{\gamma}) \\ \cdot |Z_{bw}(\gamma, \dot{\gamma})|^{c-1} - \mu \cdot \dot{\gamma}(t) \cdot |Z_{bw}(\gamma, \dot{\gamma})|^c, \end{aligned} \tag{26}$$

where μ, λ, η, c, and b are the Bouc–Wen model parameters to be determined, $Z(\gamma, \dot{\gamma})$ is the frictional torque in the DMF, and T is the input torque of the primary flywheel assembly. On the basis of the model, $Z(\gamma, \dot{\gamma})$ can be given by

$$Z(\gamma, \dot{\gamma}) = \frac{1}{2}\left(T - J_p \cdot \ddot{\beta} + J_s \cdot \ddot{\alpha}\right) - K(\beta - \alpha). \tag{27}$$

Thus, the parameters of the Bouc–Wen model can be identified based on the dynamic test data, and the identification method has been described in the literature [20].

3.2. Nonlinear Dynamic Model of the DMF with Bifilar CPVA.
Referring to Figure 2, the coordinates of $M(x_M, y_M)$ are expressed as

$$x_M = R\cos(\alpha) + l\cos(\alpha + \phi), \tag{28}$$

$$y_M = R\sin(\alpha) + l\sin(\alpha + \phi). \tag{29}$$

Then,

$$\dot{x}_M = R\dot{\alpha}\sin(\alpha) - l(\dot{\alpha} + \dot{\phi})\sin(\alpha + \phi), \tag{30}$$

$$\dot{y}_M = R\dot{\alpha}\cos(\alpha) + l(\dot{\alpha} + \dot{\phi})\cos(\alpha + \phi). \tag{31}$$

Thus, the velocity of M can be obtained from the following equation:

$$|v_M|^2 = (\dot{x}_M)^2 + (\dot{y}_M)^2 = R^2\dot{\alpha}^2 + 2Rl\dot{\alpha}(\dot{\alpha} + \dot{\phi})\cos(\phi) + l^2(\dot{\phi} + \dot{\alpha})^2. \tag{32}$$

The kinetic energy U of the DMF with the bifilar CPVA can be written as

$$\begin{aligned} U &= \frac{1}{2}J_p\beta^2 + \frac{1}{2}(J_s + I)\dot{\alpha}^2 + \frac{1}{2}m|v_M|^2 \\ &= \frac{1}{2}J_p\beta^2 + \frac{1}{2}(J + I)\dot{\alpha}^2 + \frac{1}{2}mR^2\dot{\alpha}^2 \\ &\quad + mRl\dot{\alpha}(\dot{\alpha} + \dot{\phi})\cos(\phi) + \frac{1}{2}ml^2(\dot{\phi} + \dot{\alpha})^2. \end{aligned} \tag{33}$$

Since the gravitational potential energy of the system is too small compared with the elastic potential energy, the potential energy V can be given by
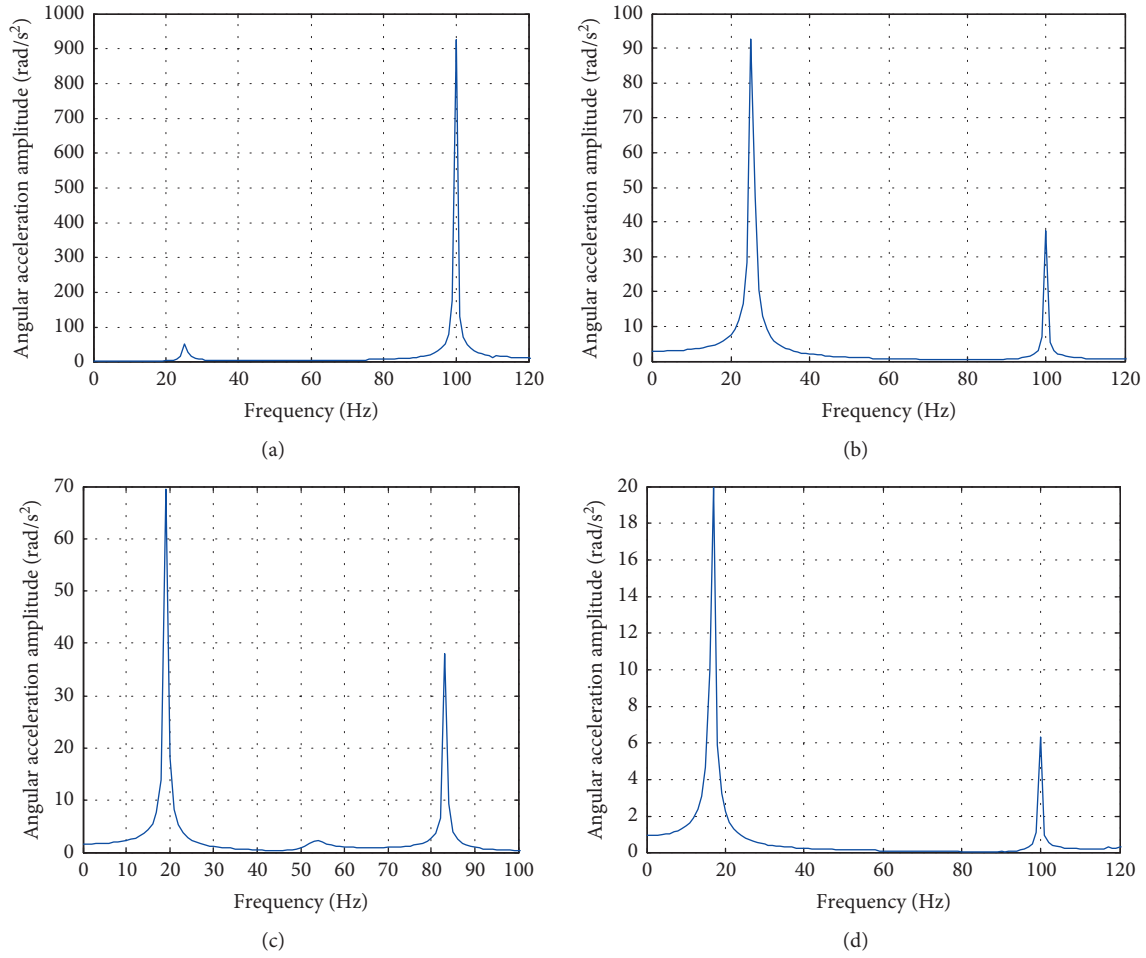
Figure 17: Spectra of J_8 and J_{10} at 3000 r/min of engine speed: (a) spectrum of J_8 and (b) spectrum of J_{10} of DMF; (c) spectrum of J_{10} of DMF with simple CPVA; (d) spectrum of J_{10} of DMF with bifilar CPVA.

Table 4: The overall angular acceleration amplitudes corresponding to different rotational speeds.

Engine speed (r/min)	J_8 (rad/s^2)	DMF J_{10} (rad/s^2)	DMF with simple CPVA J_{10} (rad/s^2)	DMF with bifilar CPVA (rad/s^2)
800	210.0	90.00	53.00	30
1000	1350	800.0	495.0	152.0
1500	1065	250.0	165.0	80.00
2000	1030	115.00	92.00	31.00
2500	1030	95.00	85.00	23.00
3000	1030	96.00	85.00	21.00

Table 5: The 2nd order angular acceleration amplitudes corresponding to different rotational speeds.

Engine speed (r/min)	J_8 (rad/s^2)	DMF J_{10}(rad/s^2)	DMF with simple CPVA J_{10} (rad/s^2)	DMF with bifilar CPVA (rad/s^2)
800	170	70.00	42.00	26
1000	1100	600.0	465.0	80.0
1500	980	175.0	150.0	35.00
2000	950	50.00	50.00	12.00
2500	960	36.00	37.00	8.00
3000	930	37.00	37.00	7.00
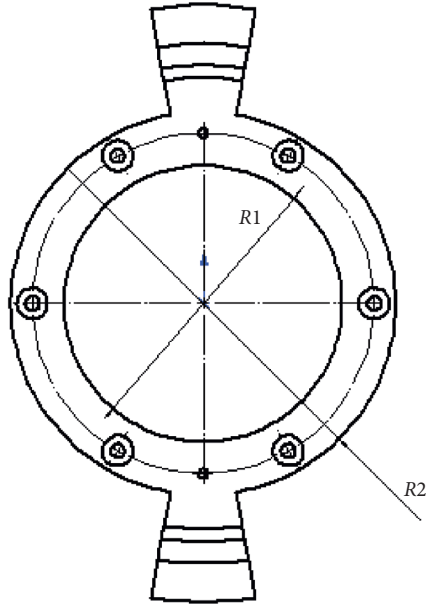
FIGURE 18: Structure diagram of the driven plate.
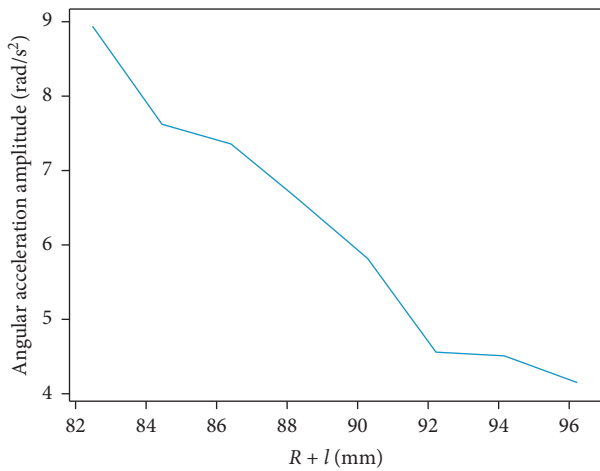
FIGURE 19: Variation in angular acceleration amplitude of J_{10} with $R + l$.

FIGURE 20: Sensors layout of real vehicle test.
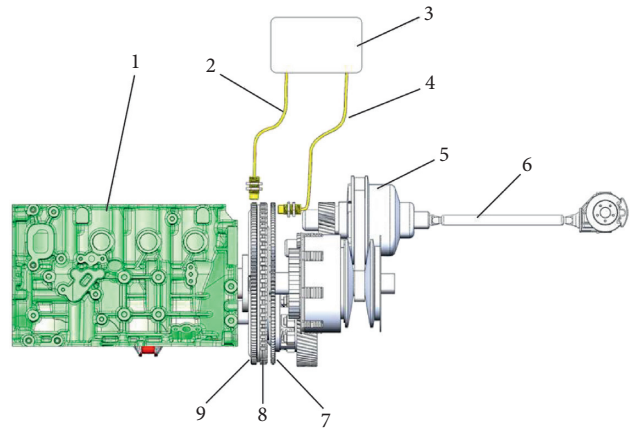
FIGURE 21: Schematic diagram of electromagnetic rotating speed sensors arrangement. 1, engine; 2, the no. 1 sensor; 3, Siemens data acquisition instrument; 4, the no. 2 sensor; 5, CVT gearbox; 6, transmission shaft; 7, the signal gear on the input shaft of the gearbox; 8, DMF; 9, the signal gear on the primary flywheel.

$$V = \frac{1}{2} k (\beta - \alpha)^2. \tag{34}$$

Then, the Lagrangian L of the system is described as

$$L = U - V = \frac{1}{2} J_p \dot{\beta}^2 + \frac{1}{2} (J_s + I) \dot{\alpha}^2 + \frac{1}{2} m R^2 \dot{\alpha}^2$$
$$mRl\dot{\alpha}(\dot{\alpha} + \dot{\phi})\cos(\phi) + \frac{1}{2} m l^2 (\dot{\phi} + \dot{\alpha})^2 - \frac{1}{2} k (\beta - \alpha)^2. \tag{35}$$

For the primary flywheel assembly, the generalized force M_1 is given by

$$M_1 = T - Z(\gamma, \dot{\gamma}). \tag{36}$$

For the secondary flywheel assembly, the generalized force M_2 is described as

$$M_2 = Z(\gamma, \dot{\gamma}). \tag{37}$$

For the bifilar CPVA, the generalized force M_3 is shown as

$$M_3 = -C_a \dot{\phi}. \tag{38}$$

Using Lagrangian mechanics, the Lagrangian equations of motion are expressed as

FIGURE 22: Digital acquisition hardware inside the car.

(a)

(b)
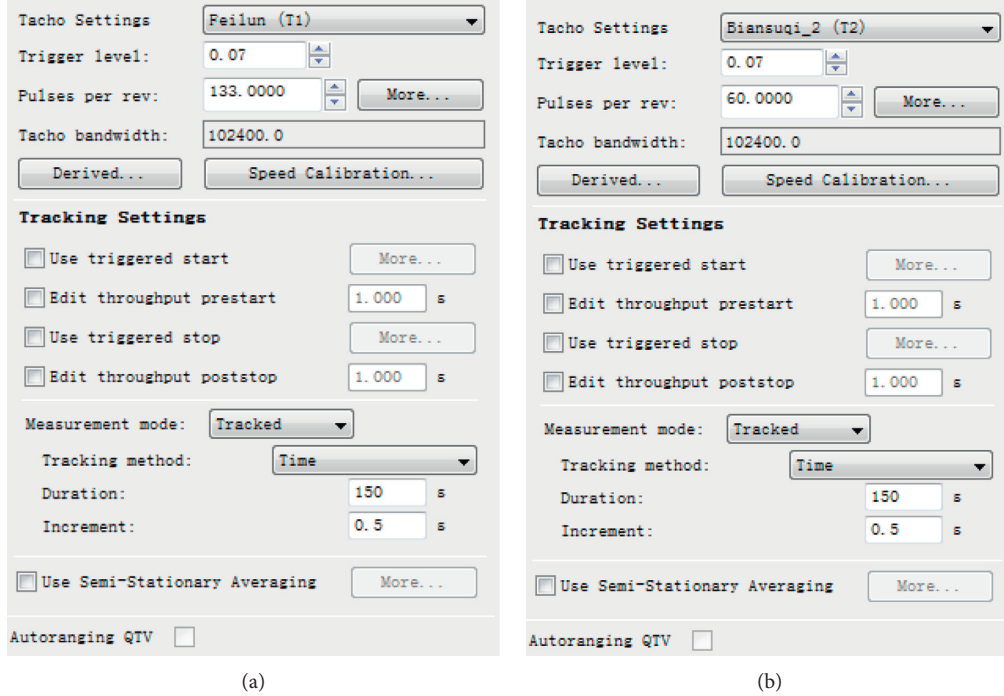
FIGURE 23: Measurement tracking setting: (a) tracking setting of rotating speed signal channel of the primary flywheel; (b) tracking setting of rotating speed signal channel of the input shaft of the gearbox.

$$\frac{d}{dt}\left(\frac{\partial L}{\partial \dot{\beta}}\right) - \frac{\partial L}{\partial \beta} = M_1, \tag{39}$$

$$\frac{d}{dt}\left(\frac{\partial L}{\partial \dot{\alpha}}\right) - \frac{\partial L}{\partial \alpha} = M_2, \tag{40}$$

$$\frac{d}{dt}\left(\frac{\partial L}{\partial \dot{\phi}}\right) - \frac{\partial L}{\partial \phi} = M_3. \tag{41}$$

Substituting equation (35) into equations (39), (40), and (41), the nonlinear dynamic model of the DMF with bifilar CPVA can be obtained as

$$J_p \ddot{\beta} + K(\beta - \alpha) = T - Z(\gamma, \dot{\gamma}), \tag{42}$$

$$\left(J_s + m\left(l^2 + R^2\right) + 2mRl\,\cos(\phi) + I\right)\ddot{\alpha}$$
$$+ m\left(l^2 + Rl\,\cos(\phi)\right)\ddot{\phi} - mRl\,\sin(\phi)\dot{\phi}^2 \tag{43}$$
$$- 2mRl\,\sin(\phi)\dot{\alpha}\dot{\phi} + k(\alpha - \beta) = Z(\gamma, \dot{\gamma}),$$

$$m\left(l^2 + Rl\,\cos(\phi)\right)\ddot{\alpha} + ml^2\ddot{\phi} + mRl\,\sin(\phi)\dot{\phi}^2 = -C_a\dot{\phi}. \tag{44}$$

3.3. Dynamic Model of Power Transmission System.
Referring to the structural parameters of a certain vehicle with a four-cylinder and four-stroke engine, the torsional vibration models of 10 degrees of freedom and 11 degrees of freedom of the power transmission system with the DMF with bifilar CPVA are developed, respectively, under idling and driving conditions, as depicted in Figures 4 and 5 .

In Figures 4 and 5, J_i is the moment of inertia of each rotating element of the vehicle powertrain, K_i is the torsional stiffness of each elastic element, and C_a is the viscous damping coefficient between the bifilar CPVA and the secondary flywheel assembly. The specific meanings and values of these parameters are listed in Tables 1 and 2 . The equations of motion of the power transmission system are deduced as follows:

(a)   (b)
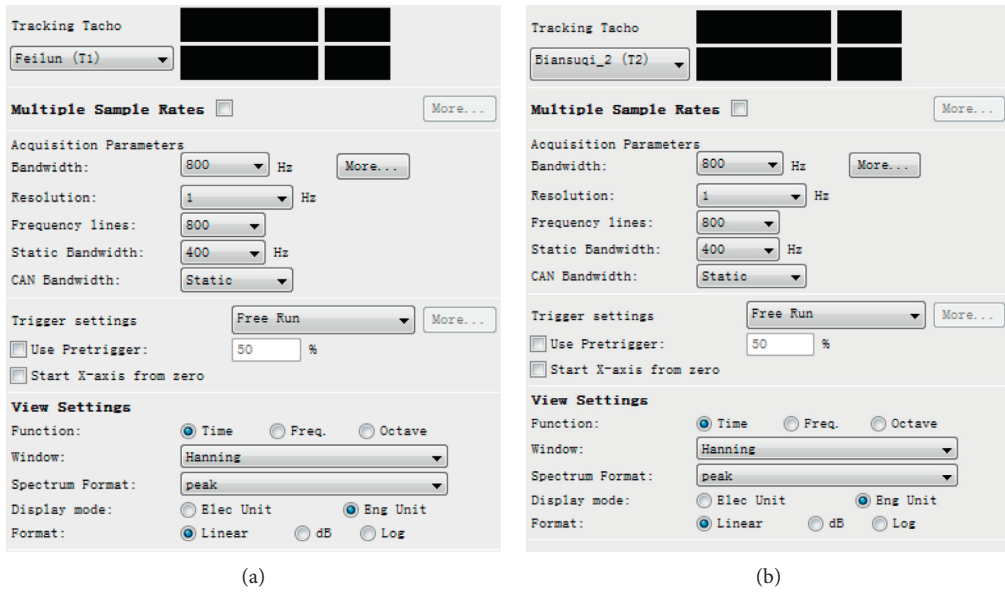
FIGURE 24: Acquisition setup: (a) acquisition setting of rotating speed signal channel of the primary flywheel; (b) acquisition setting of rotating speed signal channel of the input shaft of the gearbox.

FIGURE 25: Measurement channels setting.
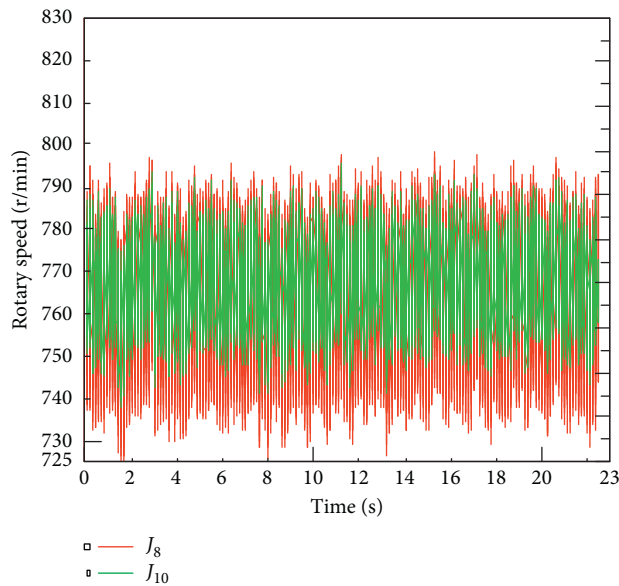
FIGURE 26: The speed curves of the primary flywheel and the input shaft of the gearbox matching the DMF under the idling condition.
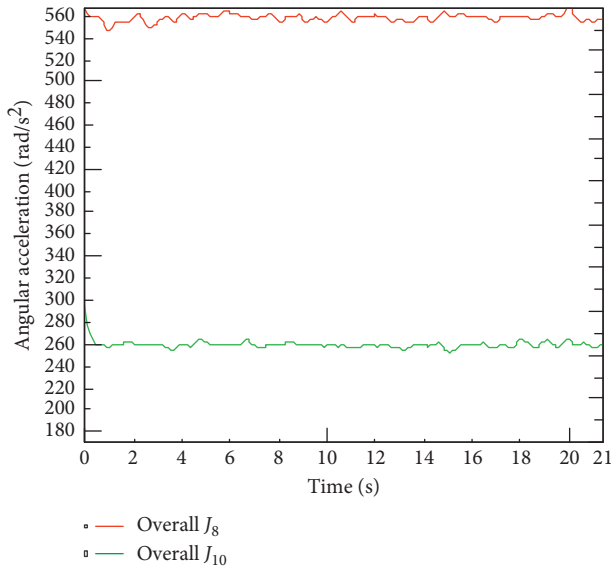
FIGURE 27: The overall angular acceleration curves of the primary flywheel and the input shaft of the gearbox matching the DMF under the idling condition.
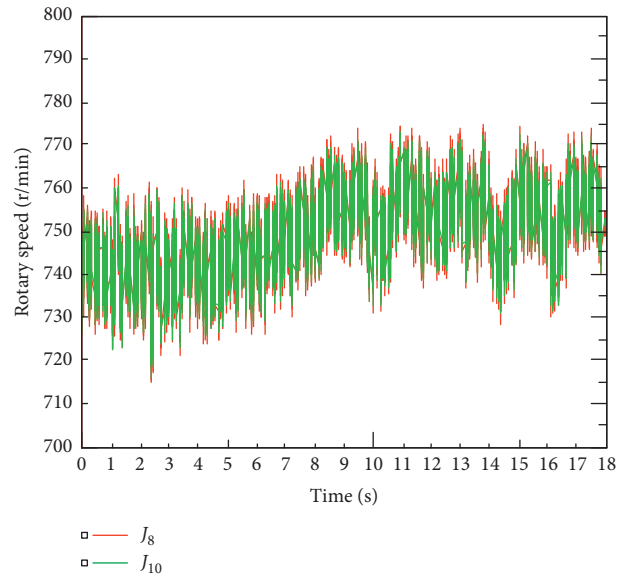
FIGURE 29: The rotary speed curves of the primary flywheel and the input shaft of the gearbox matching the DMF with the bifilar CPVA under the idling condition.
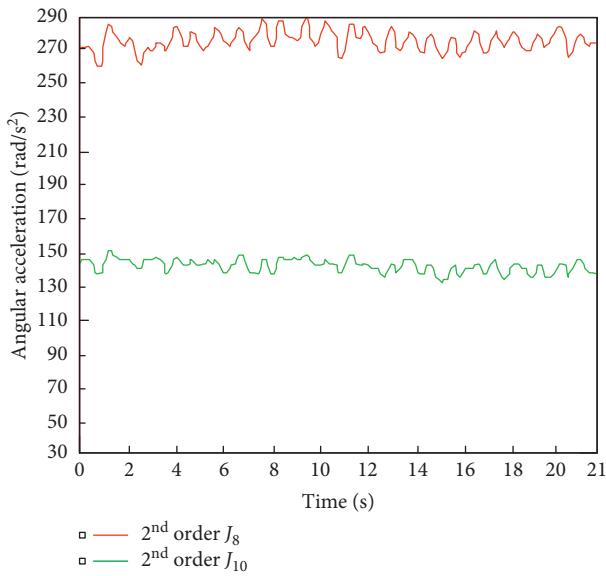
FIGURE 28: The 2nd order angular acceleration curves of the primary flywheel and the input shaft of the gearbox matching the DMF under the idling condition.

TABLE 6: Angular acceleration amplitudes under the idling condition for the powertrain with the DMF.

Items	J_8 (rad/s^2)	J_{10}(rad/s^2)
The overall angular acceleration	550	260
The 2nd order angular acceleration	280	140
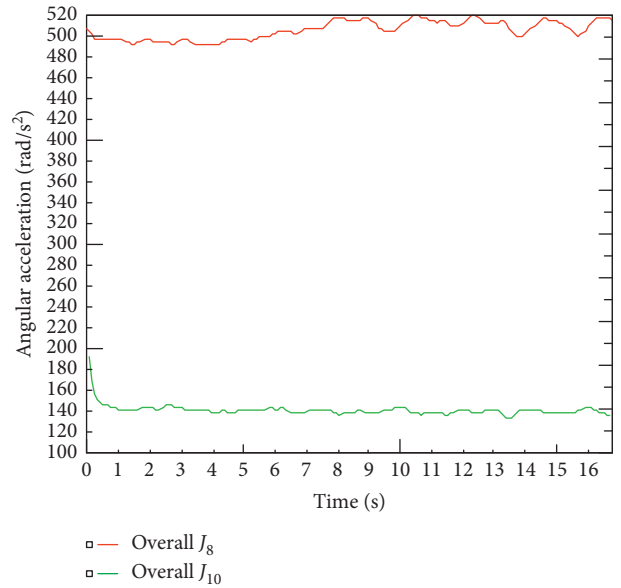
FIGURE 30: The overall angular acceleration curves of the primary flywheel and the input shaft of the gearbox matching the DMF with the bifilar CPVA under the idling condition.

$$\begin{cases} J_1\ddot{\alpha}_1 + k_1(\alpha_1 - \alpha_2) = 0 \\ J_2\ddot{\alpha}_2 - k_1(\alpha_1 - \alpha_2) + k_2(\alpha_2 - \alpha_3) = 0 \\ J_3\ddot{\alpha}_3 - k_2(\alpha_2 - \alpha_3) + k_3(\alpha_3 - \alpha_4) = 0 \\ J_4\ddot{\alpha}_4 - k_3(\alpha_3 - \alpha_4) + k_4(\alpha_4 - \alpha_5) = T_1 \\ J_5\ddot{\alpha}_5 - k_4(\alpha_4 - \alpha_5) + k_5(\alpha_5 - \alpha_6) = T_2 \\ J_6\ddot{\alpha}_6 - k_5(\alpha_5 - \alpha_6) + k_6(\alpha_6 - \alpha_7) = T_3 \\ J_7\ddot{\alpha}_7 - k_6(\alpha_6 - \alpha_7) + k_7(\alpha_7 - \alpha_8) = T_4 \\ J_8\ddot{\alpha}_8 - k_7(\alpha_7 - \alpha_8) + k_8(\alpha_8 - \alpha_9) = -Z(\gamma, \dot{\gamma}) \\ J_9 + I + m(l^2 + R^2) + 2mRl\cos(\phi)\alpha_9 + (ml^2 + mRl\cos(\ddot{\phi}))\ddot{\phi} - mRl\sin(\phi)\dot{\phi}^2 \\ \quad -2mRl\sin(\phi)\dot{\alpha}_9\dot{\phi} + k_8(\alpha_9 - \alpha_8) + k_9(\alpha_9 - \alpha_{10}) = Z(\gamma, \dot{\gamma}) \\ (ml^2 + mRl\cos(\phi))\ddot{\alpha}_9 + ml^2\ddot{\phi} + mRl\sin(\phi)\dot{\alpha}_9^2 = -C_a\dot{\phi} \\ J_{10}\ddot{\alpha}_{10} - k_9(\alpha_9 - \alpha_{10}) = 0, \end{cases} \tag{45}$$

$$\begin{cases} J_1\ddot{\alpha}_1 + k_1(\alpha_1 - \alpha_2) = 0 \\ J_2\ddot{\alpha}_2 - k_1(\alpha_1 - \alpha_2) + k_2(\alpha_2 - \alpha_3) = 0 \\ J_3\ddot{\alpha}_3 - k_2(\alpha_2 - \alpha_3) + k_3(\alpha_3 - \alpha_4) = 0 \\ J_4\ddot{\alpha}_4 - k_3(\alpha_3 - \alpha_4) + k_4(\alpha_4 - \alpha_5) = T_1 \\ J_5\ddot{\alpha}_5 - k_4(\alpha_4 - \alpha_5) + k_5(\alpha_5 - \alpha_6) = T_2 \\ J_6\ddot{\alpha}_6 - k_5(\alpha_5 - \alpha_6) + k_6(\alpha_6 - \alpha_7) = T_3 \\ J_7\ddot{\alpha}_7 - k_6(\alpha_6 - \alpha_7) + k_7(\alpha_7 - \alpha_8) = T_4 \\ J_8\ddot{\alpha}_8 - k_7(\alpha_7 - \alpha_8) + k_8(\alpha_8 - \alpha_9) = -Z(\gamma, \dot{\gamma}) \\ J_9 + I + m(l^2 + R^2) + 2mRl\cos(\phi)\alpha_9 + (ml^2 + mRl\cos(\ddot{\phi}))\ddot{\phi} - mRl\sin(\phi)\dot{\phi}^2 \\ \quad -2mRl\sin(\phi)\dot{\alpha}_9\dot{\phi} + k_8(\alpha_9 - \alpha_8) + k_9(\alpha_9 - \alpha_{10}) = Z(\gamma, \dot{\gamma}) \\ (ml^2 + mRl\cos(\phi))\ddot{\alpha}_9 + ml^2\ddot{\phi} + mRl\sin(\phi)\dot{\alpha}_9^2 = -C_a\dot{\phi} \\ J_{10}\ddot{\alpha}_{10} - k_9(\alpha_9 - \alpha_{10}) + k_{10}(\alpha_{10} - \alpha_{11}) = 0 \\ J_{11}\ddot{\alpha}_{11} - k_{10}(\alpha_{10} - \alpha_{11}) = 0, \end{cases} \tag{46}$$

where α_i is the angular displacement of each rotating element, ϕ is the swing angle of the bifilar CPVA, and T_i is the excitation torque acting on the crankshaft.

4. Simulation Analysis

The parameters of the dynamic models of the power transmission system with the DMF of the bifilar CPVA are listed in Tables 1 and 2, which are from the vehicle manufacturer Dongfeng Xiaokang Automobile Co. Ltd.

The algorithm to solve the equations of motion and simulate the dynamic behaviors is summarized in Table 3. The purpose of the simulation is to compare the damping performance of the DMF with bifilar CPVA, the DMF with simple CPVA, and the DMF under idling and driving conditions. The amplitude of the angular acceleration of the input shaft of the gearbox (J_{10}) is used as an index to predict the damping performance [1]. The dynamic model of the simple CPVA engaged in the simulation is referred to the literatures [12, 18, 19].

In the following simulation analysis, all acceleration amplitudes refer to the half of the peak-to-peak amplitudes. In addition, we cannot obtain the actual excitation torque values of the engine from the engine manufacturer, and the excitation torque values in the following simulation under idling and driving conditions are set by the way of estimation.

4.1. Dynamic Response under the Idling Condition. Under the idling condition, the engine speed commonly is around 800 r/min and thus $\omega_e = 800$ r/min. Simultaneously, the vehicle is equipped with a four-cylinder and four-stroke engine; accordingly, the main harmonic-order ε of the excitation from the engine is 2. In addition, the ignition sequence of the engine is 1, 3, 4, and 2. Therefore, the
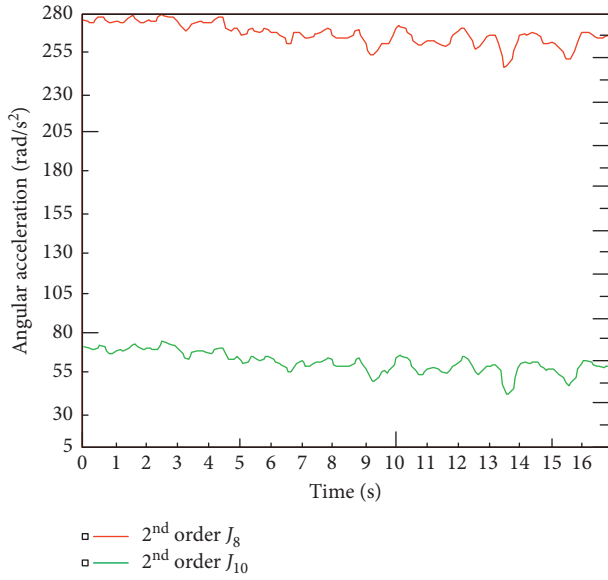
FIGURE 31: The 2nd order angular acceleration curves of the primary flywheel and the input shaft of the gearbox matching the DMF with the bifilar CPVA under the idling condition.

TABLE 7: Angular acceleration amplitudes under the idling condition of the powertrain matching the DMF with the bifilar CPVA.

Items	J_8 (rad/s²)	J_{10} (rad/s²)
The overall angular acceleration	510	150
The 2nd order angular acceleration	270	65
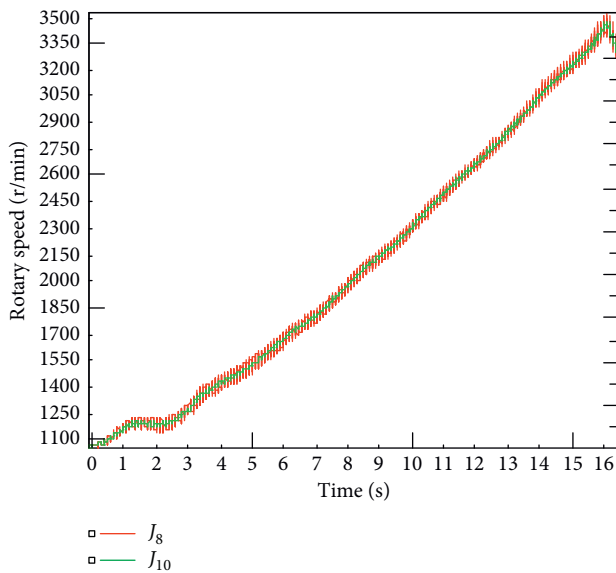
FIGURE 32: The rotary speed curves of the primary flywheel and the input shaft of the gearbox matching the DMF with the bifilar CPVA under driving conditions.
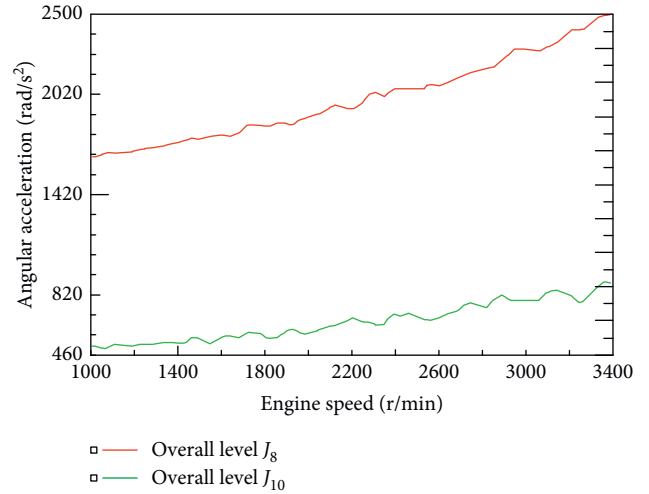

FIGURE 33: The overall angular acceleration curves of the primary flywheel and the input shaft of the gearbox matching the DMF with the bifilar CPVA under driving conditions.
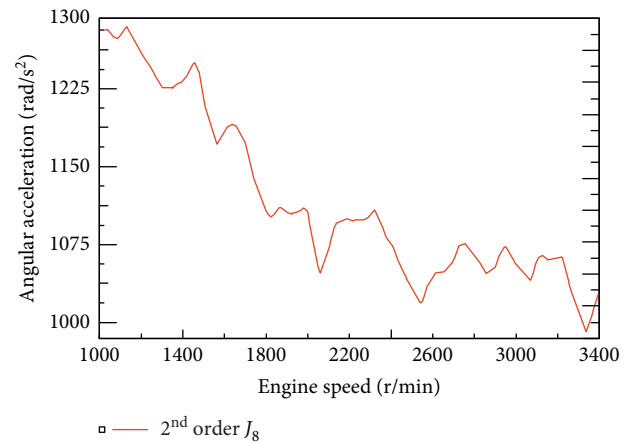
FIGURE 34: The 2nd order angular acceleration curve of the primary flywheel matching with the bifilar CPVA under driving conditions.
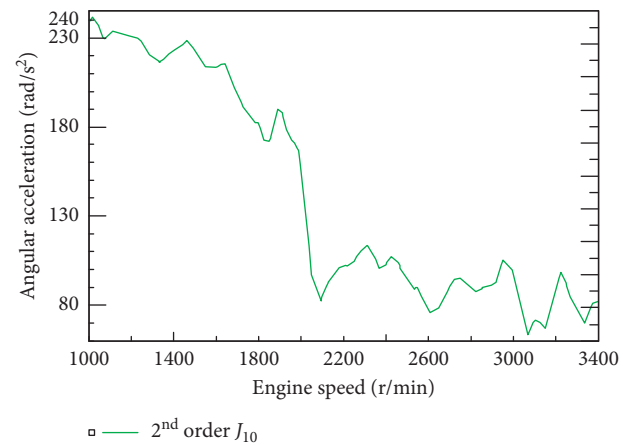
FIGURE 35: The 2nd order angular acceleration curve of the input shaft of the gearbox matching the DMF with the bifilar CPVA under driving conditions.

TABLE 8: The 2nd order angular acceleration amplitudes under the driving condition for the powertrain matching the DMF with the bifilar CPVA.

Engine speed (r/min)	J_8 (rad/s^2)	J_{10} (rad/s^2)
1000	1300	240
1500	1170	225
2000	1055	152
2500	1020	90
3000	1060	93
3400	1040	83
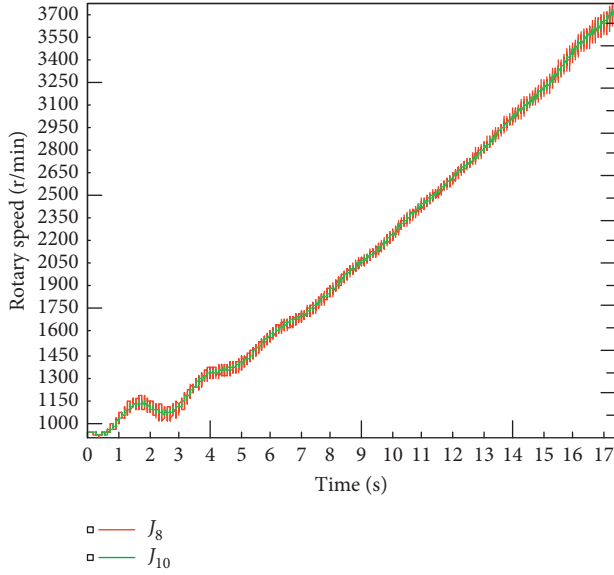
FIGURE 36: The rotary speed curves of the primary flywheel and the input shaft of the gearbox matching the DMF under driving conditions.
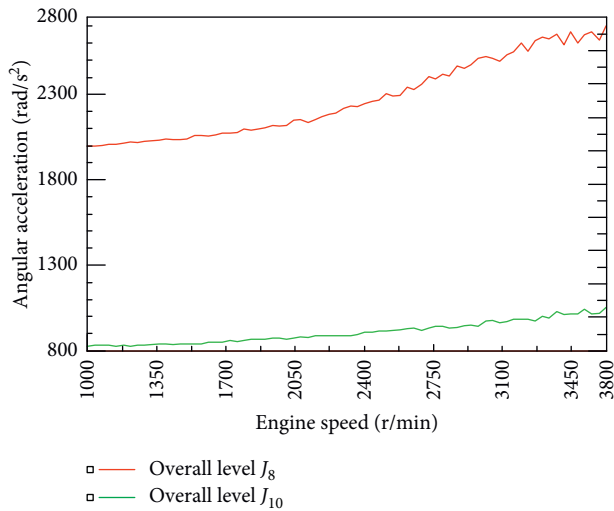

FIGURE 37: The overall angular acceleration curves of the primary flywheel and the input shaft of the gearbox matching the DMF under driving conditions.
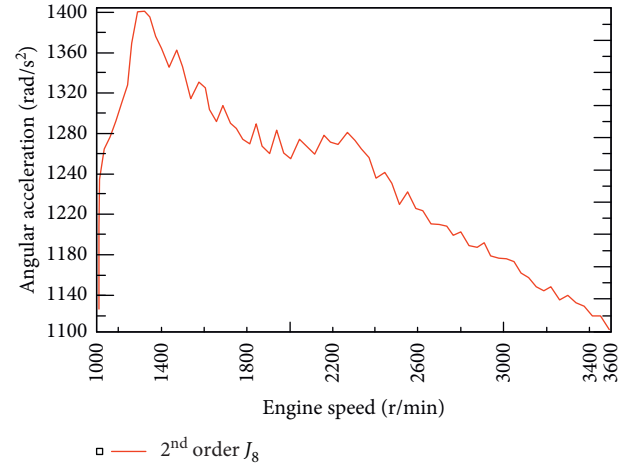
FIGURE 38: The 2nd order angular acceleration curve of the primary flywheel matching without the CPVA under driving conditions.

excitation torques T_1, T_2, T_3, and T_4 are expressed as follows, where $T_e = 5N \cdot m$:

$$
\begin{cases}
T_1 = T_e \sin\left((\varepsilon \cdot \omega_e \cdot 2\pi/60) \cdot t\right) \\
T_2 = T_e \sin\left((\varepsilon \cdot \omega_e \cdot 2\pi/60) \cdot t + 4\pi\right) \\
T_3 = T_e \sin\left((\varepsilon \cdot \omega_e \cdot 2\pi/60) \cdot t + \pi\right) \\
T_4 = T_e \sin\left((\varepsilon \cdot \omega_e \cdot 2\pi/60) \cdot t + 3\pi\right).
\end{cases}
\tag{47}
$$

According to the parameters (Table 3), the simulation algorithm is carried out and the angular accelerations are obtained, as shown in Figure 6, where the blue curve represents the angular acceleration of the primary flywheel assembly J_8, the green curve represents the angular acceleration of the input shaft of the gearbox J_{10} with the DMF, the red curve represents the angular acceleration of the input shaft of the gearbox J_{10} with the DMF with the simple CPVA, and the black curve represents the angular acceleration of the input shaft of the gearbox J_{10} with the DMF with the bifilar CPVA.

In the steady-state region, the overall angular acceleration amplitude of J_8 is 210 rad/s^2, the overall angular acceleration amplitude of J_{10} of DMF is 90 rad/s^2, the overall angular acceleration amplitude of J_{10} of DMF with simple CPVA is 53 rad/s^2, and the overall angular acceleration amplitude of J_{10} of DMF with bifilar CPVA is 30 rad/s^2. In order to get a better view of the angular
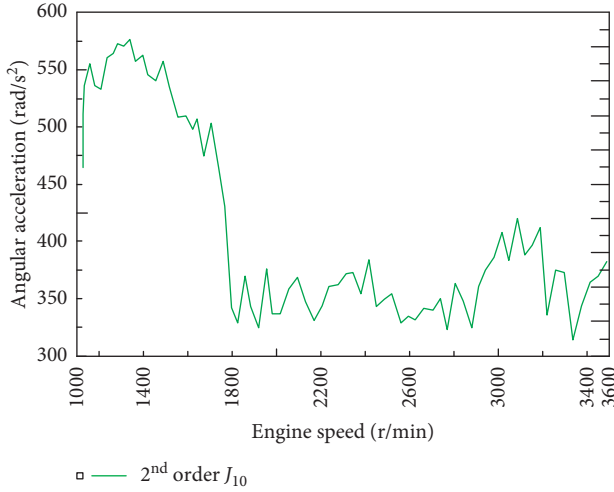
FIGURE 39: The 2nd order angular acceleration curve of the input shaft of the gearbox matching the DMF under driving conditions.

TABLE 9: The 2nd order angular acceleration amplitudes under the driving condition for the powertrain matching the DMF.

Engine speed (r/min)	J_8 (rad/s^2)	J_{10} (rad/s^2)
1000	1240	475
1500	1380	550
2000	1240	350
2500	1230	350
3000	1180	375
3400	1130	360

acceleration, the FFT of the acceleration signals has been plotted (see Figure 7).

4.2. Simulation under the Driving Condition.

Under the driving condition, the simulations are carried out at five different speeds, that is, $\omega_e = 1000$ r/min, $\omega_e = 1500$ r/min, $\omega_e = 2000$ r/min, $\omega_e = 2500$ r/min, and $\omega_e = 3000$ r/min. The excitation torques T_1, T_2, T_3, and T_4 are expressed as equation (47), where $T_e = 25 N m$ and $\varepsilon = 2$ The time-domain dynamic response results are shown in Figures 8–12 , respectively, where the blue curve represents the angular acceleration of the primary flywheel assembly J_8, the green curve represents the angular acceleration of the input shaft of the gearbox J_{10} with the DMF, the red curve represents the angular acceleration of the input shaft of the gearbox J_{10} with the DMF with the simple CPVA, and the black curve represents the angular acceleration of the input shaft of the gearbox J_{10} with the DMF with the bifilar CPVA. The FFT results of the acceleration signals are plotted in Figures 13–17 .

Under the working condition of engine speed (1000 rpm), the overall angular acceleration amplitude of J_8 is 1350 rad/s^2, the overall angular acceleration amplitude of J_{10} of DMF is 800 rad/s^2, the overall angular acceleration amplitude of J_{10} of DMF with simple CPVA is 495 rad/s^2, and the overall angular acceleration amplitude of J_{10} of DMF

with bifilar CPVA is 152 rad/s^2. The FFT of the acceleration signals is obtained in Figure 13.

Under the working condition of engine speed (1500 rpm), the overall angular acceleration amplitude of J_8 is 1065 rad/s^2, the overall angular acceleration amplitude of J_{10} of DMF is 250 rad/s^2, the overall angular acceleration amplitude of J_{10} of DMF with simple CPVA is 165 rad/s^2, and the overall angular acceleration amplitude of J_{10} of DMF with bifilar CPVA is 80 rad/s^2. The FFT of the acceleration signals is been shown in Figure 14.

Under the working condition of engine speed (2000 rpm), the overall angular acceleration amplitude of J_8 is 1030 rad/s^2, the overall angular acceleration amplitude of J_{10} of DMF is 115 rad/s^2, the overall angular acceleration amplitude of J_{10} of DMF with simple CPVA is 92 rad/s^2, and the overall angular acceleration amplitude of J_{10} of DMF with bifilar CPVA is 31 rad/s^2. The FFT of the acceleration signals is given in Figure 15.

Under the working condition of engine speed (2500 rpm), the overall angular acceleration amplitude of J_8 is 1030 rad/s^2, the overall angular acceleration amplitude of J_{10} of DMF is 95 rad/s^2, the overall angular acceleration amplitude of J_{10} of DMF with simple CPVA is 85 rad/s^2, and the overall angular acceleration amplitude of J_{10} of DMF with bifilar CPVA is 23 rad/s^2. The FFT of the acceleration signals is plotted as Figure 16.

Under the working condition of engine speed (3000 rpm), the overall angular acceleration amplitude of J_8 is 1030 rad/s^2, the overall angular acceleration amplitude of J_{10} of DMF is 96 rad/s^2, the overall angular acceleration amplitude of J_{10} of DMF with simple CPVA is 85 rad/s^2, and the overall angular acceleration amplitude of J_{10} of DMF with bifilar CPVA is 21 rad/s^2. The FFT of the acceleration signals is plotted as Figure 17.

4.3. Analysis of Simulation Results.

Considering the simulation results of different speed conditions, the overall angular acceleration amplitudes of J_8 and J_{10}, which are the total dynamic responses of the power transmission system, are listed in Table 4 based on the simulation results. In the light of the FFT results, the 2nd order angular acceleration amplitudes of J_8 and J_{10} are summarized in Table 5 for engine speed 800 rpm, 1000 rpm, 1500 rpm, 2000 rpm, 2500 rpm, and 3000 rpm, and the 2nd order harmonic frequencies are 26.7 Hz, 33.3 Hz, 50 Hz, 66.7 Hz, 83.3 Hz, and 100 Hz, respectively.

The simulation results both in the idling and driving conditions show that the DMF with the bifilar CPVA shows best effect on the attenuation of engine speed fluctuation in a speed range of 800 to 3000 r/min. When the engine speed is lower than 1500 r/min, the effect of the DMF with simple CPVA on the attenuation of engine speed fluctuation is better than that of the DMF; however, the damping effect is basically the same as the DMF when the engine speed is higher than 1500 r/min. Furthermore, since the square root of the ratio of R and l from Table 2 is equal to 2, the 2nd harmonic-order excitation of the engine could be attenuated completely according to

TABLE 10: Attenuation rate of the angular acceleration under the idling condition.

Damper	Attenuation rate of the overall angular acceleration (%)	Attenuation rate of the 2nd order angular acceleration (%)
DMF	53	50
DMF with bifilar CPVA	70.5	76

TABLE 11: Attenuation rate of the 2nd order angular acceleration under the driving condition.

Condition	DMF attenuation rate of the 2nd order angular acceleration (%)	DMF with the bifilar CPVA attenuation rate of the 2nd order angular acceleration (%)
1000 r/min	62	82.5
1500 r/min	60	80.8
2000 r/min	71	85.6
2500 r/min	71	91.1
3000 r/min	68	91.2
3400 r/min	68	92
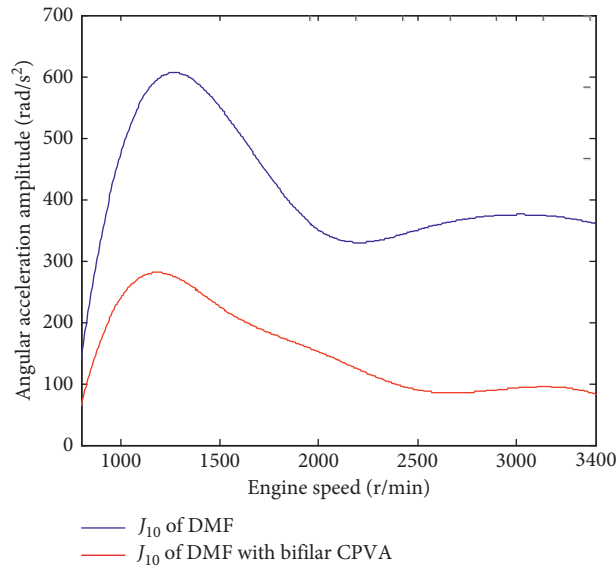
FIGURE 40: Comparison of the 2nd order angular acceleration amplitudes of J_{10} in the input shaft of the gearbox in the test.

equation (21). However, the simulation results demonstrate that the 2nd harmonic-order excitation is not completely eliminated, which is attenuated by more than 90%.

To summarize, the DMF with the bifilar CPVA shows the best damping effect in the whole speed range. Furthermore, in the low-speed region, the vibration reduction effect of the DMF with simple CPVA is better than that of the DMF, whereas they show the same damping performance in the high-speed region. In addition, the εth harmonic-order excitation from the engine

cannot be attenuated completely but can be attenuated by more than 90% when the square root of the ratio of R and l is equal to ε.

5. Discussion on the Influence of R and l on Damping Performance

The linear dynamic model of the bifilar CPVA suggests that the εth harmonic-order excitation from the engine can theoretically be eliminated completely on the condition that the R and l of the bifilar CPVA satisfy equation (21). Al-
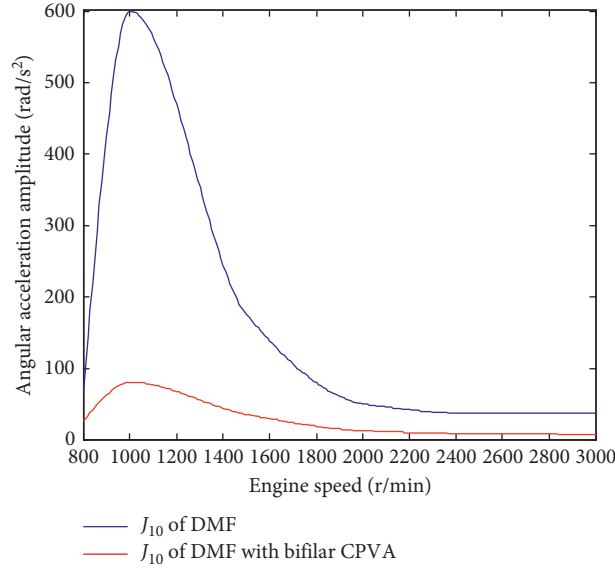
FIGURE 41: Comparison of the 2nd order angular acceleration amplitudes of J_{10} in the input shaft of the gearbox in the simulation.

though the simulation results demonstrate that the DMF with bifilar CPVA does not achieve the theoretical damping performance with R and l satisfying equation (21), and its damping effect on the torsional vibration from the engine is still excellent, which indicates that the ratio of R to l satisfying equation (21) has significant influence on the vibration reduction effect of the DMF with bifilar CPVA. Indeed, in the case, there are many combinations of R and l.

Since the bifilar CPVA is installed on the driven plate of the DMF (Figure 18), the size of R and l of the bifilar CPVA is limited by the size of the driven plate. Let the inner and outer diameters of the driven plate be, respectively, R_1 and R_2, then

$$0.5R_1 \leq R \leq 0.5R_2. \tag{48}$$

With reference to equation (21), the relationship between R and l satisfies

$$\frac{R}{l} = \varepsilon^2. \tag{49}$$

Thus,

$$\frac{1 + \varepsilon^2}{2\varepsilon^2} R_1 \leq R + l \leq \frac{1 + \varepsilon^2}{2\varepsilon^2} R_2. \tag{50}$$

The constraint conditions of the system are shown in equation (50), the design variable of the system is $R + l$, and then, the objective function of the system is given by

$$f(\ddot{\alpha}_{10}) = \min f(\dot{\alpha}_1 \ldots \dot{\alpha}_{11}, \alpha_1 \ldots \alpha_{11}, \dot{\phi}, \phi), \tag{51}$$

where $f(\dot{\alpha}_1 \ldots \dot{\alpha}_{11}, \alpha_1 \ldots \alpha_{11}, \dot{\phi}, \phi)$ is the system state equation from equations (45) and (46): $R_1 = 132$ mm and $R_2 = 154$ mm.

For the four-cylinder and four-stroke engine, ε is equal to 2. Based on the above model, the angular acceleration amplitude of J_{10} varying with the structural parameter $R + l$ of the bifilar CPVA can be plotted in Figure 19 by using Newton's method.

The result shows that, under the above constraints, the amplitude of the angular acceleration of J_{10} is inversely proportional to $R + l$; that is, the damping effect of the DMF with the bifilar CPVA is directly proportional to $R + l$.

6. Real Vehicle Tests

In this section, the real vehicle tests are carried out for power transmissions matching the DMF with the bifilar CPVA and the DMF. The test vehicle is a Fengguang series SUV of Dongfeng Xiaokang automobile company. As for the test vehicle, the maximum torque and the maximum speed of the four-cylinder and four-stroke engine are 220 Nm and 6000 r/min, respectively, which is equipped with a CVT from Aisin Seiki Company. Figure 20 shows the sensor layout on the power transmission. Two electromagnetic rotating speed sensors, in which the model number is ONOSOKKI-MP-910, are mounted on the housing of the gearbox, where the no. 1 sensor is pointed to the signal gear on the primary flywheel and the no. 2 sensor is pointed to the signal gear on the input shaft of the gearbox, and the arrangement details of these two sensors are shown in Figure 21. It should be noted that there was no signal gear on the input shaft of the gearbox. In order to test the rotational speed of the input shaft, a signal gear was processed and installed on the input shaft of the gearbox. The signals of rotating speed are acquired by Siemens data acquisition instrument (Figure 22), of which the type is LMS SCADAS302VB.

During the tests, the rotating speed signals of the output shaft of the engine and the input shaft of the gearbox are tested under the idling and driving conditions, and the angular acceleration signals can be obtained by derivative of speed signals to time. The rotating speed signals of the electromagnetic rotating speed sensor are similar to the sinusoidal wave. Let the rotating speed of the gear be ω (r/min), the number of teeth of the gear be z_g,

and the frequency of the signals be f(Hz), then ω will be $\omega = 60 * f/z_g$. Meanwhile, the collected data were processed by Siemens LMS Test.Lab 14A, and then, tracking settings for two signal channels are shown in Figure 23, where the number of teeth of the signal gear on the primary flywheel is 133 and the number of teeth of the signal gear on the input shaft of the gearbox is 60. The acquisition parameters are shown in Figure 24, where the acquisition bandwidth is 800 Hz and sampling frequency is 2000 Hz. In Figure 25, tacho1 and tacho2 are the rotating speed signal channel of the primary flywheel and the rotating speed signal channel of the input shaft of the transmission, respectively.

The angular acceleration of the primary flywheel and the angular acceleration of the input shaft of the gearbox are measured under the idling condition and driving condition during the real vehicle experiment. Under the idling condition, the engine speed is maintained around 750 r/min for about 20 seconds; simultaneously, the angular acceleration of the primary flywheel and the angular acceleration of the input shaft of the gearbox are measured by the two electromagnetic rotating speed sensors. Under the driving condition, the gearbox is in the forward gear position, and then, the engine speed is evenly accelerated from 1000 r/min to about 3500 r/min by stepping on the accelerator pedal and the whole process is about 17 seconds. During the change in engine speed, the angular acceleration of the primary flywheel and the angular acceleration of the input shaft of the gearbox are recorded by the two electromagnetic rotating speed sensors. Under the driving condition, the engine speed range in this test is mainly based on the following two factors:

(1) The maximum speed of the engine is 6000 r/min, and then the engine speed range, 1000 r/min~3400 r/min, is the common engine speed range, which basically covers the low-speed zone and high-speed zone.

(2) At present, there is no mass production capacity of DMF with bifilar CPVA in China. The DMF with bifilar CPVA used in this experiment is a sample, and the reliability and fatigue experiments have not been done, so this experiment does not cover the whole engine speed range.

In the following test data analysis, all acceleration amplitudes refer to the half of the peak-to-peak amplitudes.

6.1. Real Vehicle Test under the Idling Condition. For the powertrain with the DMF, the engine speed is around 750 r/min under the idling condition, as shown in Figure 26, in which the red and green curves represent the engine speed and the speed of the input shaft of the gearbox, respectively. Obviously, the fluctuating range of the engine speed is from 730 r/min to 790 r/min. Figure 27 shows the overall angular acceleration under the idling condition, in which the red and green curves, respectively, present the overall angular acceleration of the primary flywheel and the input shaft of the gearbox. Furthermore, the 2nd order angular acceleration

can be obtained by harmonic tracking, as shown in Figure 28, where the red and green curves, respectively, present the 2nd order angular acceleration of the primary flywheel and the input shaft of the gearbox.

According to the test results for the powertrain with the DMF under the idling condition, the specific data are shown in Table 6, which indicates that the overall and 2nd angular acceleration of the engine are attenuated by 53% and 50%, respectively.

For the powertrain matching the DMF with the bifilar CPVA, the engine speed is also around 750 r/min under the idling condition, as shown in Figure 29, in which the red and green curves represent the engine speed and the input shaft of the gearbox rotary speed, respectively; obviously, the fluctuating range of the engine speed is from 720 r/min to 770 r/min. Figure 30 shows the overall angular acceleration under the idling condition, in which the red and green curves, respectively, present the overall angular acceleration of the primary flywheel and the input shaft of the gearbox. Similarly, the 2nd order angular acceleration by harmonic tracking is shown in Figure 31, where the red and green curves, respectively, present the 2nd order angular acceleration of the primary flywheel and the input shaft of the gearbox.

According to the test results, for the powertrain matching the DMF with the bifilar CPVA under the idling condition, the specific data are listed in Table 7, which suggests that the overall and 2nd angular acceleration of the engine are attenuated by 70.5% and 76%, respectively.

6.2. Real Vehicle Test under the Driving Condition. For the powertrain matching the DMF with the bifilar CPVA, under the driving condition, the range of the engine speed is 1000 r/min–3500 r/min, as shown in Figure 32, in which the red and green curves represent the engine speed and the rotary speed of the input shaft of the gearbox, respectively. Figure 33 shows the overall angular acceleration under the driving condition, and Figures 34 and 35 depict the 2nd order angular acceleration of the primary flywheel and the input shaft of the gearbox.

During the test, the engine speed increased from 1000 r/min to 3500 r/min, the overall angular acceleration is affected by the speed of the accelerator pedal, and thus, the 2nd order angular acceleration can more accurately reflect the damping effect. The specific data of the 2nd order angular acceleration are listed in Table 8. When the engine speed is 1000 r/min, 1500 r/min, 2000 r/min, 2500 r/min, 3000 r/min, and 3400 r/min, the 2nd angular acceleration of the engine is attenuated by 82.5%, 80.8%, 85.6%, 91.1%, 91.2%, and 92%, respectively.

For the powertrain with the DMF, under the driving condition, the range of engine speed is 1000 r/min–3700 r/min. As shown in Figure 36, the red and green curves represent the engine speed and the rotary speed of the input shaft of the gearbox, respectively. Figure 37 shows the overall angular acceleration under the driving condition. Moreover, the 2nd order angular acceleration by harmonic tracking is shown in Figures 38 and 39 .

The specific data of the 2nd order angular acceleration are shown in Table 9. When the engine speed is 1000 r/min, 1500 r/min, 2000 r/min, 2500 r/min, 3000 r/min, and 3400 r/min, respectively, the 2nd angular acceleration of the engine is attenuated by 62%, 60%, 71%, 71%, 68%, and 68%, respectively.

6.3. Discussion on Real Vehicle Test Result. The experimental data under idling and driving conditions are summarized in Tables 10 and 11, respectively, and the comparison of the 2nd order angular acceleration amplitudes of J_{10} in the input shaft of the gearbox in the test is plotted in Figure 40, which represent that the DMF with bifilar CPVA shows a better damping performance than DMF under idling and driving conditions. Moreover, regarding the DMF, the 2nd angular acceleration amplitude of the input shaft of the gearbox is rapidly reduced with the engine speed from 750 r/min to 2000 r/min but basically stable with the engine speed from 2000 r/min to 3400 r/min. On the other hand, considering the DMF with the bifilar CPVA, the 2nd order angular acceleration amplitude of the input shaft of the gearbox is uniformly attenuated with the engine speed from 750 r/min to 3400 r/min.

Referring to the simulation data in Table 5, the comparison of the 2nd order angular acceleration amplitudes of J_{10} in the input shaft of the gearbox in the simulation is plotted in Figure 41. The simulated excitation torque value is not the actual excitation value, the actual excitation frequencies are more complex, and the angular acceleration amplitudes cannot be used as a reference in the comparison of experimental results and simulation results; however, the two comparisons of the 2nd order angular acceleration amplitudes of J_{10} (Figures 40 and 41) demonstrate basically the same trend; that is, the 2nd angular acceleration amplitudes of the input shaft of the gearbox are rapidly attenuated as for the DMF and the DMF with bifilar CPVA with the engine speed lower than 2000 r/min. Nevertheless, when the engine speed is higher than 2000 r/min, the 2nd order angular accelerations of the input shaft of the gearbox with the DMF are basically stable; on the contrary, the 2nd order angular accelerations of the input shaft of the gearbox matching the DMF with bifilar CPVA are still attenuated. In addition, the DMF with bifilar CPVA shows a better damping performance than DMF in the whole test speed range. The regular pattern shows that the experimental results are basically consistent with the simulation results, which validate the validity of the proposed dynamic model of the DMF with the bifilar CPVA.

There are few published studies about DMF and CPVA as an ensemble, and in [12], only numerical simulation was done and no experimental verification was carried out. In addition, the real vehicle experiment of a clutch with CPVA was executed in [13]; however, the testing condition of this experiment was engine speed at 850 r/min and the test results showed that the 2nd order rotational speed amplitude was attenuated by 90% under the condition. Compared with the rotational speed, the angular acceleration can better characterize the torsional vibration of the powertrain. In this paper, the engine speed range of real vehicle experiment is wider, and the damping performance of DMF and DMF with bifilar CPVA is compared and analyzed by angular acceleration from the test results, which makes up for the lack of verification work of real vehicle experiment in previous research.

7. Conclusions

This study addresses the linear and the nonlinear dynamic model of the DMF with the bifilar CPVA. The linear dynamic model of the DMF with the bifilar CPVA reveals the vibration reduction principle and the importance of the structural parameters of R and l. Furthermore, the dynamic model of the powertrain based on the nonlinear dynamic model of the DMF with the bifilar CPVA is developed, and the dynamic responses are simulated through the speed range of 800–3000 r/min. Moreover, the influence of R and l on the damping performance is discussed on the basis of the dynamic model, and subsequently, the validity of the model is verified by the real vehicle tests under idling and driving conditions. The main conclusions of this research are summed up as follows:

(1) The bifilar CPVA can be regarded as a dynamic unit in which the natural frequency varies with the rotational speed. The linear dynamic model shows that the εth harmonic-order torsional vibration can be eliminated completely when the square root of the ratio of R and l is equal to ε; however, the simulation and test results indicate that the εth harmonic-order torsional vibration can only be attenuated by 80% to 90% and not be isolated from the transmission completely.

(2) Under the constraints of the installation size and the ratio of R to l, the angular acceleration amplitude of the input shaft of the gearbox is inversely proportional to $R + l$; that is, the damping effect of the DMF with the bifilar CPVA is directly proportional to $R + l$.

(3) In the whole engine speed region, the DMF with bifilar CPVA possesses the best damping performance among the three kinds of torsional dampers, which are the DMF, the DMF with simple CPVA, and the DMF with bifilar CPVA. If the square root of the ratio of R and l is equal to ε, for the DMF, the εth order angular acceleration amplitude of the input shaft of the gearbox can be rapidly attenuated by the DMF with the engine speed lower than 2000 r/min, but it is basically stable with the engine speed higher than 2000 r/min. For the DMF with the bifilar CPVA, the εth order angular acceleration amplitude of the input shaft of the gearbox can be continuously attenuated in the whole engine speed region.

(4) The simulation and test results suggest that the angular acceleration amplitudes of the primary flywheel are hardly affected by the DMF and the DMF with the bifilar CPVA.

(5) The nonlinear dynamic model of the DMF with the bifilar CPVA contains the dynamic parameters of the

DMF and the structural parameters of the bifilar CPVA. In this paper, the influence of R and l on the damping performance of the system is only discussed theoretically, and the comparison tests of different R and l have not been carried out due to the limited experimental conditions and the difficulty in making samples.

(6) The model and methods discussed here can offer guidelines for the design and optimization of DMF with bifilar CPVA and similar shock absorbers for rotating machinery systems.

(7) The simulation and test results show that bifilar CPVA can further improve the damping performance of DMF by attenuating the 2nd order rotational speed fluctuation. By analyzing the influence of the performance parameters of bifilar CPVA on the design model of DMF, the method of improving the performance parameters of DMF will be found to attenuate the rotational speed fluctuation from the engine in other orders and the damping performance of DMF with bifilar CPVA can be further enhanced, which will be the focus of the future research.

Data Availability

The data used to support the findings of this study are included within the article.

Conflicts of Interest

The authors declare that there are no conflicts of interest with respect to the research, authorship, and publication of this article.

Authors' Contributions

Lei Chen conceptualized the study, investigated the study, and wrote the original draft. Lei Chen and Jianming Yuan prepared the methodology. Jinmin Hu analyzed using the software. Hang Cai and Jianming Yuan validated the study. Jianming Yuan reviewed and edited the manuscript. Lei Chen and Jinmin Hu obtained funding acquisition. All authors have read and agreed to the published version of the manuscript.

Acknowledgments

References

[1] G. Wu and W. Luan, "Review of dynamic research for NVH problems related to automotive driveline," *Journal of Mechanical Engineering*, vol. 49, no. 24, pp. 108–119, 2013.

[2] N. Pavel, P. Ales, and Z. Martin, "Investigating the influence of computational model complexity on noise and vibration modeling of powertrain," *Journal of Vibroengineering*, vol. 18, no. 1, pp. 378–393, 2016.

[3] Y. D. Hao, Z. C. He, G. Y. Li, E. Li, and Y. Y. Huang, "Uncertainty analysis and optimization of automotive driveline torsional vibration with a driveline and rear axle coupled model," *Engineering Optimization*, vol. 50, no. 11, pp. 1871–1893, 2018.

[4] F. Jian, K. Diao, and X. Wang, "Experimental study and simulation analysis on torsional vibration characteristic of 3-cylinder engine driveline system," *Journal of Vibration, Measurement & Diagnosis*, vol. 40, no. 1, pp. 115–121, 2020.

[5] H. Ahmed, M. Eliot, and T. Stephanos, "A Study on torsional vibration attenuation in automotive drivetrains using absorbers with smooth and non-smooth nonlinearities," *Journal of Applied Mathematical Modeling*, vol. 46, pp. 674–690, 2017.

[6] W. B. Shang guan, X. L. Liu, Y. Yin, and S. Rakheja, "Modeling of automotive driveline system for reducing gear rattles," *Journal of Sound and Vibration*, vol. 416, pp. 136–153, 2018.

[7] L. Chen, W. Shi, Z. Chen, G. Liu, and H. Liu, "An analysis on torsional characteristics of Dual Mass Flywheel and vehicle test study," *Automotive Engineering*, vol. 41, no. 11, pp. 1294–1300, 2019.

[8] L. Song, Z. Zhi, L. Zeng, and H. Tian, "Design research on the safety device of automobile Dual Mass Flywheel based on auto-lock theory," *Journal of Mechanical Engineering*, vol. 51, no. 4, pp. 141–147, 2015.

[9] Y. Wang, X. Qin, S. Huang, and S. Deng, "Design and analysis of a multi-stage torsional stiffness dual mass flywheel based on vibration control," *Applied Acoustics*, vol. 104, pp. 172–181, 2016.

[10] M. Cirelli, J. Gregori, P. P. Valentini, and E. Pennestrí, "A Design chart approach for the tuning of parallel and trapezoidal bifilar centrifugal pendulum," *Mechanism and Machine Theory*, vol. 140, pp. 711–729, 2019.

[11] W. Li, L. Yan, and W. Shi, "Analysis of isolation of the torsional vibration of DMF -CS with centrifugal pendulum-type absorber," *Journal of China Mechanical Engineering*, vol. 20, no. 15, pp. 1787–1790, 2009.

[12] H. Wu and G. Wu, "Centrifugal pendulum vibration absorber and its application to torsional vibration damper with large angular displacement," *Automotive Engineering*, vol. 39, no. 12, pp. 1409–1416, 2017.

[13] M. Hässler, A. Kooy, R. Welter, and V. Lichtenwald, "Clutch disc with centrifugal pendulum absorber," *Auto Tech Review*, vol. 5, no. 4, pp. 26–31, 2016.

[14] S.-C. S. Seong and G. W. Kim, "Torsional vibration isolation performance evaluation of centrifugal pendulum absorbers for clutch dampers," *Transactions of the Korean Society for Noise and Vibration Engineering*, vol. 26, no. 4, pp. 436–442, 2016.

[15] L. Chen, W. Shi, and Z. Chen, "Modeling of idle speed transmission based on unit modeling method and performance comparison of various torsional dampers," *Journal of Central South University (Science and Technology)*, vol. 51, no. 3, pp. 842–852, 2020.

[16] M. Rao and C. Sujatha, "Design of centrifugal pendulum vibration absorber to reduce the axial vibration of rotating shafts for multiple orders," *SAE International Journal of Passenger Cars*, vol. 13, no. 2, pp. 1–23, 2020.

[17] A. S. Alsuwaiyan and S. W. Shaw, "Performance and dynamic stability of general-path centrifugal pendulum vibration absorbers," *Journal of Sound and Vibration*, vol. 252, no. 5, pp. 791–815, 2002.

[18] C. Shi and R. G. Parker, "Modal properties and stability of centrifugal pendulum vibration absorber systems with equally

spaced, identical absorbers," *Journal of Sound and Vibration*, vol. 331, no. 21, pp. 4807–4824, 2012.

[19] M. C. Cirelli, E. Valentini, and E. Pennestr, "The tuning conditions for circular, cycloidal and epicycloidal centrifugal pendula: a unified cartesian approach," *Mechanism and Machine Theory*, vol. 150, pp. 1–26, 2020.

[20] J. Mayet and H. Ulbrich, "Tautochronic centrifugal pendulum vibration absorbers," *Journal of Sound and Vibration*, vol. 333, no. 3, pp. 711–729, 2014.

[21] C. Shi and R. G. Parker, "Optimal tuning of centrifugal pendulum vibration absorbers," in *Proceedings of the ASME 2013 International Design Engineering Technical Conferences and Computers and Information in Engineering Conference*, vol. 8, Portland, OR, USA, August 2013.

[22] V. Pier Paolo, M. Cirelli, and Simone Di Donato, "The compliant centrifugal pendulum as the vibration absorber with second-order elasto-kinematic approximation," *Journal of Vibration and Control*, vol. 20, 2020.

[23] L. Chen, R. Zeng, and Z. Jiang, "Nonlinear dynamical model of an automotive dual mass flywheel," *Advances in Mechanical Engineering*, vol. 7, no. 6, pp. 1–11, 2015.

[24] J. E. Mottershead and R. Stanway, "Identification of Nth-Power velocity damping," *Journal of Sound and Vibration*, vol. 105, no. 2, pp. 309–319, 1986.

Research Article

Investigation of Low-Frequency Sound Radiation Characteristics and Active Control Mechanism of a Finite Cylindrical Shell

Shaohu Ding [ID], Chunyang Mu, Yang Gao, Hong Liu, and Maoqiang Li

College of Mechatronic Engineering, North MinZu University, Yinchuan, China

Correspondence should be addressed to Shaohu Ding; dingshaohu05@163.com

In this paper, the radiation characteristics and active structural acoustic control of a submerged cylindrical shell at low frequencies are investigated. First, the coupled vibro-acoustic equations for a submerged finite cylindrical shell are solved by a modal decomposition method, and the radiation impedance is obtained by the fast Fourier transform. The modal shapes of the first ten acoustic radiation modes and the structure-dependent radiation modes are presented. The relationships between the vibration modes and the radiation modes as well as the contributions of the radiation modes to the radiated sound power are given at low frequencies. Finally, active structural acoustic control of a submerged finite cylindrical shell is investigated by considering the fluid-structure coupled interactions. The physical mechanism of the active control is discussed based on the relationship between the vibration and radiation modes. The results showed that, at low frequencies, only the first several radiation modes contributed to the sound power radiated from a submerged finite cylindrical shell excited by a radial point force. By determining the radiation modes that dominate the contribution to the radiated sound, the physical mechanism of the active control is explained, providing a potential tool to allow active control of the vibro-acoustic responses of submerged structures more effectively.

1. Introduction

As a basic structural form, the cylindrical shell is commonly used in aerospace, marine, and other industrial fields. Such shell is excited to vibrate and radiate noise, and its vibro-acoustic characteristics have been widely concerned [1–5]. When a structure is immersed in a dense fluid (such as water), the vibration of the structure produces sound waves, causing the surrounding medium to vibrate, and in turn, the sound pressure acting on the structure as the excitation complicates the analysis of structural vibration. The sound behavior of a shell in water is very different from that in air, and as such, has received considerable attention [3–5]. To analyze the structural vibrations and sound radiation of fluid-loaded structures, many researchers investigated the effect of both external and internal fluid on shell vibrations taking into account the fluid-structure interaction. Junger [6] and Sandman [7] expanded the radial displacement of the cylindrical surface into Fourier series along the circumference. They expressed the radiated sound pressure in

terms of acoustic impedance through the boundary conditions of the fluid-solid interface. Amabili [8–10] studied the coupled vibration of shell-external fluid and shell-internal fluid and presented the solution for cylindrical shells filled and partially immersed in incompressible and compressible fluid. Kwak [11] investigated free flexural vibration of a finite cylindrical shell in contact with external fluid. The kinetic energy of the fluid is derived by solving the boundary-value problem. At the same time, many researchers have sought to develop efficient methods to reduce the noise of cylindrical structures. Generally, these methods can be divided into two subgroups. The first group contains passive methods, which reduce the noise of a structure using additional mass, dynamic vibration absorber, or viscoelastic damping material on the structure surface. The second subgroup contains active methods [12–17], which reduce the structurally radiated noise using actuators, sensors, and control algorithms. The passive method is not satisfactory in noise reduction in the low-frequency range. Therefore, the active control method, as an alternative to the passive

control method, has been used in noise control in the low-frequency range.

There have been a lot of literatures on the vibroacoustic characteristics of cylindrical shells. However, to use active structural sound control methods to effectively suppress the radiated noise of cylindrical shells, it is necessary to understand the modal characteristics of the vibration and radiation of the cylindrical shell in the low-frequency range. Sepanishen [2] investigated the radiation impedance of an infinite cylinder with a finite-length, nonuniform velocity distribution. Chen et al. [18] explored the modal radiation efficiency and radiation power of stiffened double-cylindrical shells considering the fluid field between the inner shell and outer shell. The results show that radiation efficiency and radiation power were affected mainly by the low-order modes at low frequencies. Lin et al. [19] discussed the modal characteristics of sound radiation of finite cylindrical shells using boundary element methods. The results show that, for each group of modes with the same circumferential modal index, the modal radiation efficiency decreases as the axial modal index increases. Peters et al. [20] presented a modal decomposition technique to analyze individual modal contributions to the sound power radiated from an externally excited structure submerged in a dense fluid. To control the structural vibrations and sound radiation of fluid-loaded structures, there have been few reports focused on vibration control through modal approaches and even fewer reports dealing with the modal control of vibrations and sound radiation [21, 22].

A thorough exploration of the vibrations and sound radiation would be conducive to understand the physical mechanism of the active noise reduction, provide guidance for optimal design, determine the arrangement of the actuators and the sensors, and select the control target. Structural vibration modes can be used to investigate the mechanism of structural acoustic radiation [23]. However, the sound radiation of each structural vibration mode is not independent, as the modes are coupled [24]. This creates difficulties when analyzing the structural acoustic radiation using structural vibration modes. In the early 1990s, Elliott and Johnson [23] presented the theory of acoustic radiation modes (a-modes) and decomposed the total sound power radiated from an elastic structure into a superposition of finite radiation modes. Each radiation mode was independent. These modes were only determined by the shape and size of the vibrating structure, and they were unrelated to the physical properties and boundary conditions of the structure. The advantages of acoustic radiation modes have attracted significant attention for the analysis and control of structural acoustic radiation in recent years [25–29]. In our previous research [30], we discussed the contribution of the low-order vibration modes and acoustic radiation modes to the radial squared velocity and the radiated sound power in different fluids and found that compared in water, more vibration modes and acoustic radiation modes are required to calculate the sound power in air. To accurately predict the vibro-acoustic behavior of a structure, the concept of structure-dependent radiation modes (s-modes) was presented by Photiadis [31] and developed by Ji and Bolton [32] to describe the sound power radiation from a simple vibrating beam and a thin baffled plate. Compared with a-modes, s-modes have more potential advantages because the sound power radiation is related to the boundary conditions and the material properties of the structure. However, previous studies on acoustic radiation modes and structure-dependent radiation modes are mostly for flat structures, and considerable research has been conducted on the vibration modes of cylindrical shells. There has been little research on acoustic radiation modes and structure-dependent radiation modes of the cylindrical shell. Further, several articles have examined the active structural acoustic control of submerged finite cylindrical shells [33–36]. However, few literatures explored the physical mechanism analysis of active control by using the relationship between the vibration modes and radiation modes.

In this work, by means of a modal expansion approach, the coupled vibro-acoustic equations for a finite cylindrical shell are solved first. The radiation impedance, which expresses the modal coupling caused by the fluids, is then obtained using the fast Fourier transform. Second, the modal shapes of the first few acoustic radiation modes and structure-dependent radiation modes are presented. The contributions of the low-order radiation modes to the sound power are discussed for a cylindrical shell immersed in a dense fluid using the solution of the vibration equation. The active structural acoustic control of a submerged finite cylindrical shell is investigated by considering the fluid-structure coupling interaction. An analytical expression for the optimal complex amplitude of the secondary force is derived based on the uncoupled characteristics of the sound power radiated from the finite cylindrical shell in the circumferential direction. The control effects with one and two control forces are also compared. Finally, the physical mechanism of the active structural acoustic control of the submerged finite cylindrical shell is analyzed based on the changes of the amplitude and sound power of the acoustic radiation modes and the structure-dependent radiation modes.

2. Theory

2.1. Theoretical Modeling Approach. A finite cylindrical shell with two semi-infinite cylindrical rigid baffles is considered, as illustrated in Figure 1; L is the length of the shell and h and a denote the wall thickness and radius of the shell, respectively. The shell is immersed in an unbounded fluid whose density is ρ_l, and the speed of sound in this fluid is c_l. The fluid is assumed to be stationary, nonviscous, and compressible.

In this study, the Flügge equations of motion are used to model the fluid-loaded cylindrical shell. The fluid-structure interaction problem is solved using an infinite shell model, which is shown to be a good approximation for finite shells [5]. The mathematical problem to be solved according to Flügge shell theory is
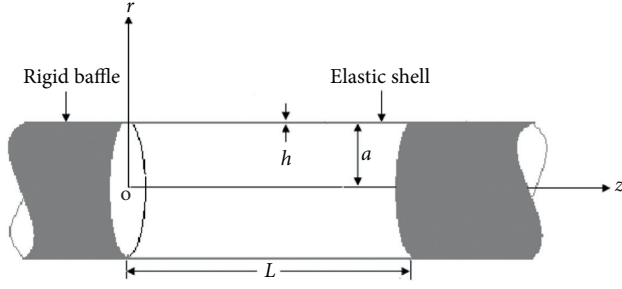
FIGURE 1: Baffled cylindrical shell and coordinate system.

$$\{\mathbf{L}_{3\times3}\}\begin{bmatrix} u(r,\phi,z) \\ v(r,\phi,z) \\ w(r,\phi,z) \end{bmatrix} = \frac{(1-\nu^2)a^2}{E^*h}\left(\begin{bmatrix} f_u \\ f_v \\ f_w - p_w \end{bmatrix}\right), \quad (1)$$

where $\mathbf{L}_{3\times3}$ refers to the coefficient matrix of the Flügge operator, the elements of which is given in Appendix A, and u, v, and w are the displacements of cylindrical shells in the x-, ϕ-, and z-directions, respectively. $E^* = E(1-i\eta)$ is the complex Young's modulus; η is the damping loss factor; f_u, f_v, and f_w are the excitation forces of the cylindrical shell in the x-, ϕ-, and z-directions, respectively; and, p_w represents the fluid load on the shell surface.

When simply supported boundary conditions are considered and the time-dependent factor of $e^{-i\omega t}$ is omitted, the displacement of the cylindrical shells in the x-, ϕ-, and z-directions can be expressed as

$$u(z,\phi) = \sum_{\alpha=0}^{1}\sum_{n=0}^{\infty}\sum_{m=1}^{\infty} C_{unm}^{\alpha} \cos(k_m z)\sin\left(n\phi + \frac{\alpha\pi}{2}\right)$$

$$= \sum_{n=0}^{\infty} u_n(z,\phi),$$

$$v(z,\phi) = \sum_{\alpha=0}^{1}\sum_{n=0}^{\infty}\sum_{m=1}^{\infty} C_{vnm}^{\alpha} \sin(k_m z)\cos\left(n\phi + \frac{\alpha\pi}{2}\right)$$

$$= \sum_{n=0}^{\infty} v_n(z,\phi), \quad (2)$$

$$w(z,\phi) = \sum_{\alpha=0}^{1}\sum_{n=0}^{\infty}\sum_{m=1}^{\infty} C_{wnm}^{\alpha} \sin(k_m z)\sin\left(n\phi + \frac{\alpha\pi}{2}\right)$$

$$= \sum_{n=0}^{\infty} w_n(z,\phi),$$

where subscripts n ($n = 0, 1, 2, \ldots$) and m ($m = 1, 2, 3, \ldots$) correspond to the circumferential mode index and axial mode index, respectively, $k_m = m\pi/L$ is the axial wavenumber, C_{jnm}^{α} is the modal displacement response amplitude of the shell in the x-, θ-, and z-directions, $\alpha = 0$ corresponds to antisymmetric modes, and $\alpha = 1$ corresponds to symmetric modes. In this study, the disturbance force and control force are assumed to be located at $\phi = 0$ or π.

Therefore, only the symmetric modes are excited by such a force configuration for vibration analysis and noise control, which indicates that the displacements for each circumferential mode can be written as

$$u_n(z,\phi) = \sum_{m=1}^{\infty} C_{unm}^{1} \cos(k_m z)\cos(n\phi),$$

$$v_n(z,\phi) = \sum_{m=1}^{\infty} C_{vnm}^{1} \sin(k_m z)\sin(n\phi), \quad (3)$$

$$w_n(z,\phi) = \sum_{m=1}^{\infty} C_{wnm}^{1} \sin(k_m z)\cos(n\phi).$$

Considering fluid-structure coupling, the motion equation of the cylindrical shell is as follows [1]:

$$M_{mn}\left[\omega_{mn}^2(1-i\eta) - \omega^2\right]C_{wnm}^{1} = F_{mn} - P_{mn}, \quad (4)$$

where M_{mn} denotes the generalized modal mass of the shell, ω_{mn} represents the in-vacuo natural angular frequencies, η is the structural damping coefficient, and F_{mn} is the generalized modal excitation force, which can be described as follows:

$$F_{mn} = \frac{\varepsilon_n}{\pi L}\int_0^{2\pi}\int_0^L f(z_0,\phi_0)\sin\left(\frac{m\pi z}{L}\right)\cos(n\phi)dz\,d\phi$$

$$= f_0\varphi_{mn}, \quad (5)$$

where ε_n is the Neumann factor ($\varepsilon_n = 1$ for $n = 0$ and $\varepsilon_n = 2$ for $n > 0$), $f(z_0,\phi_0) = (f_0/a)\delta(z_0)\delta(\phi_0)$ is the harmonic point force applied in the radial direction of the cylindrical shell, $\varphi_{mn} = (\varepsilon_n/2\pi La)\cos(n\phi_0)\sin(k_m z_0)$, and f_0 is the complex amplitude of the excitation force.

The modal sound pressure induced by the fluid is denoted as P_{mn}, the expression of which is derived in detail in the Appendix B, and can be expressed as follows:

$$P_{mn} = -i\omega a \sum_{q=1}^{\infty} C_{wnm}^{1} Z_{qmn}, \quad (6)$$

where Z_{qmn} is the radiation impedance, which expresses the modal coupling between the different axial modal indices (m and q) due to the fluids. It can be obtained by the fast Fourier transform, which can significantly reduce the analysis time compared with traditional direct numerical integration methods [37]:

$$Z_{qmn} = \frac{2}{L}\int_0^L \mathcal{F}^{-1}\left[\tilde{z}_n(k_z)\mathcal{F}\left[f_q(z)\right]\right]\sin k_m z\,dz, \quad (7)$$

where

$$\tilde{z}_n(k_z) = \frac{i\omega\rho_l H_n\left[\left(k^2 - k_z^2\right)^{1/2}a\right]}{\left(k^2 - k_z^2\right)^{1/2}H_n'\left[\left(k^2 - k_z^2\right)^{1/2}a\right]},$$

$$f_q(z) = \begin{cases} \sin k_q z, & 0 \le z \le L \\ 0, & z < 0, z > L \end{cases}, \quad (8)$$

$$\mathcal{F}\left[f_q(z_q)\right] = \frac{k_q\left[1 - (-1)^q e^{-ik_z L}\right]}{k_q^2 - k_z^2},$$

where $\mathcal{F}$ and $\mathcal{F}^{-1}$ represent the Fourier transform and inverse Fourier transform, respectively, $k = \omega/c_l$ is the fluid wavenumber, $k_q = q\pi/L$, k_z is the structural axial wavenumber, H_n is the nth-order Hankel function of the second kind for a radially outgoing wave, and H_n' is the derivative of the Hankel function with respect to its argument.

Substituting equations (5) and (6) into equation (4), the radial displacement amplitude of the shell C_{wnm}^1 can be obtained. Then, the radiated sound power of the fluid-loaded cylinder will be acquired.

2.2. Acoustic Radiation Modes of Finite Cylindrical Shells.
Using the transfer acoustic impedance matrix $\mathbf{Z}$, the modal contributions to the radiated sound power can be acquired. It is well-known acoustic radiation modes that correspond to the eigenvectors of the resistive part of the sound impedance matrix. The acoustic radiation modes are a set of orthonormal surface velocity patterns. At low frequencies, only the first few sound radiation modes are radiated efficiently. Therefore, the total radiated sound power can be obtained by truncating the series sound radiation modes without loss of calculation accuracy.

The surface of the cylindrical shell is evenly split into N_e elementary radiators, where the area of each elementary radiator is denoted as s. The radiated sound power can be obtained through the near-field method, as follows [18]:

$$W = \frac{s}{2}\mathrm{Re}\left(\mathbf{V}^{\mathrm{H}}\mathbf{ZV}\right) = \mathbf{V}^{\mathrm{H}}\mathbf{RV}, \tag{9}$$

where $\mathbf{V}$ is the complex velocities' vector of these elementary radiators, the superscript "H" denotes the conjugate transpose, and $\mathbf{R} = (s/2)\mathrm{Re}(\mathbf{Z})$ is a real, symmetric, positive definite matrix, which is proportional to the transfer acoustic impedance matrix for the elementary radiators. These matrix elements can be expressed as follows [38]:

$$R_{ij} = \frac{s}{2}\mathrm{Re}\left\{\frac{i\omega\rho_l s}{2\pi^2}\sum_{n=0}^{\infty}\varepsilon_n\cos\left[\left(\theta_i - \theta_j\right)\right]\int_0^{k_0}\frac{\cos k_z\left(z - z'\right)}{\sqrt{k^2 - k_z^2}\,a}\frac{H_n\left[\left(k^2 - k_z^2\right)^{1/2}a\right]}{H_n'\left[\left(k^2 - k_z^2\right)^{1/2}a\right]}dk_z\right\}, \tag{10}$$

where $\mathbf{R}$ can be expressed through an eigenvector decomposition as follows:

$$\mathbf{R} = \mathbf{Q}^{\mathrm{T}}\mathbf{\Lambda}\mathbf{Q}, \tag{11}$$

where $\mathbf{Q}$ is an orthogonal matrix of eigenvectors and Λ is a diagonal matrix of eigenvalues. Substituting equation (11) into equation (9) and defining $y = \mathbf{Q}V$, equation (9) can be written as follows:

$$W = y^H\Lambda y = \sum_{k=1}^{K}\lambda_k\left|y_k\right|^2, \tag{12}$$

where $y_k = q_k^{\mathrm{T}}\mathbf{V}$ denotes the modal amplitude of the kth radiation mode, q_k is the kth radiation modal shape vector, and λ_k is called the radiation efficiency coefficient of the kth acoustic radiation mode. As shown by equation (8), the

radiation modes radiate independently, and the sound power becomes a summation of independent quantities y_k factored by the eigenvalue λ_k.

2.3. Structure-Dependent Radiation Modes.
If the vibration response of the structure is represented by the superposition of the modal vibration response, the surface velocity of the structure can be expressed by the vibration modes as follows:

$$\mathbf{V} = \mathbf{\Phi}\widehat{V}_N, \tag{13}$$

where $\widehat{V}_N$ is the corresponding modal coefficient vector, which is an $N \times 1$ column vector, N is the number of vibration modes, and $N = m \times n$:

$$\widehat{V}_N = \begin{bmatrix} \widehat{V}_{m1} & \widehat{V}_{m2} & \dots & \widehat{V}_{mn} \end{bmatrix}^{\mathrm{T}}. \tag{14}$$

Φ is an $N_e \times N$ structural mode shape matrix defined as follows:

$$\Phi = \begin{bmatrix} \sin\dfrac{\pi z_1}{L}\cos\varphi_1 & \sin\dfrac{\pi z_1}{L}\cos 2\varphi_1 & \dots & \sin\dfrac{2\pi z_1}{L}\cos\varphi_1 & \sin\dfrac{2\pi z_1}{L}\cos 2\varphi_1 & \dots & \sin\dfrac{m\pi z_1}{L}\cos n\varphi_1 \\[1em] \sin\dfrac{\pi z_1}{L}\cos\varphi_2 & \sin\dfrac{\pi z_1}{L}\cos 2\varphi_2 & \dots & \sin\dfrac{2\pi z_1}{L}\cos\varphi_2 & \sin\dfrac{2\pi z_1}{L}\cos 2\varphi_2 & \dots & \sin\dfrac{m\pi z_1}{L}\cos n\varphi_2 \\[1em] \dots & \dots & \dots & \dots & \dots & \dots & \dots \\[1em] \sin\dfrac{\pi z_2}{L}\cos\varphi_1 & \sin\dfrac{\pi z_2}{L}\cos 2\varphi_1 & \dots & \sin\dfrac{2\pi z_2}{L}\cos\varphi_1 & \sin\dfrac{2\pi z_2}{L}\cos 2\varphi_1 & \dots & \sin\dfrac{m\pi z_2}{L}\cos n\varphi_2 \\[1em] \sin\dfrac{\pi z_2}{L}\cos\varphi_2 & \sin\dfrac{\pi z_2}{L}\cos 2\varphi_2 & \dots & \sin\dfrac{2\pi z_2}{L}\cos\varphi_2 & \sin\dfrac{2\pi z_2}{L}\cos 2\varphi_2 & \dots & \sin\dfrac{m\pi z_2}{L}\cos n\varphi_2 \\[1em] \dots & \dots & \dots & \dots & \dots & \dots & \dots \\[1em] \sin\dfrac{\pi z_{Nz}}{L}\cos\varphi_{N\varphi} & \sin\dfrac{\pi z_{Nz}}{L}\cos 2\varphi_{N\varphi} & \dots & \sin\dfrac{2\pi z_{Nz}}{L}\cos\varphi_{N\varphi} & \sin\dfrac{2\pi z_{Nz}}{L}\cos 2\varphi_{N\varphi} & \dots & \sin\dfrac{m\pi z_{Nz}}{L}\cos n\varphi_{N\varphi} \end{bmatrix}. \tag{15}$$

Substituting equation (13) into equation (9), the radiated sound power can be further expressed as

$$W = \mathbf{V}^{H}\mathbf{R}\mathbf{V} = \widehat{V}_N{}^{H}\mathbf{G}\widehat{V}_N \tag{16}$$

where $\mathbf{G} = \Phi^{H}\mathbf{R}\Phi$, which is also a real symmetric positive definite matrix. Each element is considered to be the contribution of the ith mode to the structural acoustic radiation due to the vibration of the jth mode. The case where $i = j$ represents the contribution of the mode vibrations of the structure itself to the radiated sound power, and the contribution of such self-radiation to the total sound power is always dominant near the natural frequency. Its off-diagonal elements represent the contribution of the modes to the radiated sound power caused by other modes, and the values are often much smaller than the diagonal elements of the matrix.

The dimension of $\mathbf{G}$ is not only related to the number of partition elements on the structure surface but also to the number of vibration modes. It can be decomposed into the following eigenvalues:

$$\mathbf{G} = \mathrm{P}^{H}\Sigma\mathrm{P}, \tag{17}$$

where $\mathbf{P}$ is an orthogonal matrix, the eigenvectors corresponding to each row of the matrix, Σ is a diagonal matrix composed of the N eigenvalues, which are different from those defined in equation (12), and σ_r is called the radiation efficiency coefficient of the rth structure-dependent radiation mode. The matrix $\mathbf{G}$ is a real symmetric positive definite matrix, and thus, the eigenvalues have the following characteristics $\sigma_1 > \sigma_2 > \sigma_3, \cdots, > \sigma_r > 0$.

Substituting equation (17) into equation (16), the radiated sound power can be further expressed as

$$W = \widehat{V}_N^{H}\mathrm{P}^{H}\Sigma\mathrm{P}\widehat{V}_N. \tag{18}$$

Defining

$$\mathbf{g} = \mathrm{P}\widehat{V}_N. \tag{19}$$

The radiated sound power can be further expressed as

$$W = \mathbf{g}^{H}\Sigma\mathbf{g} = \sum_{r=1}^{N}\sigma_r|g_r|^2, \tag{20}$$

where N represents the number of vibration modes and g_r is the vector of linear transformations of the modal velocity amplitude of the structure surface through the transformation matrix, which is defined as the structural radiation mode vector.

2.4. Active Control of Sound Radiation from the Submerged Cylindrical Shell. Assuming that the primary force (i.e., disturbance input) is a harmonic radial point force with a known amplitude, the secondary forces (control inputs) are also one or more harmonic point forces. The objective function of the active control is the sound power radiated from the cylindrical shells subjected to primary and secondary forces. The expression of the complex amplitude of the secondary control forces is derived when minimizing the objective function.

Due to the fluid-structure interaction, the modal velocity and radiated sound power cannot be directly represented in a matrix form such that the complex amplitude of the secondary control forces can be solved easily. Because the radiated sound power of the different circumferential vibration modes is decoupled from each other [25], the radiated sound power can be determined individually for each circumferential vibration mode:

$$W = \sum_{n=0}^{\infty} W_n. \tag{21}$$

The sound power of the nth-order circumferential vibration mode can be expressed in the matrix form:

$$W_n = \widehat{V}_n{}^H \mathbf{M}_n \widehat{V}_n, \tag{22}$$

where M_n represents the $M \times P$ radiation resistance matrix corresponding to the nth-order circumferential mode.

For a selected circumferential mode, equation (4) can be written as follows:

$$\begin{pmatrix} Z_{1n}^M + Z_{11n} & Z_{12n} & \cdots & Z_{1pn} \\ Z_{21n} & Z_{2n}^M + Z_{22n} & \cdots & Z_{2pn} \\ \cdots & \cdots & \cdots & \cdots \\ Z_{1mn} & Z_{2mn} & \cdots & Z_{mn}^M + Z_{qmn} \end{pmatrix} \begin{pmatrix} \widehat{V}_{1n} \\ \widehat{V}_{2n} \\ \cdots \\ \widehat{V}_{mn} \end{pmatrix}$$
$$= \begin{pmatrix} f_{1n} \\ f_{2n} \\ \cdots \\ f_{mn} \end{pmatrix}, \tag{23}$$

where Z_{mn}^M denotes the modal mechanical impedance of the shell. $\widehat{V}_{mn} = -i\omega C_{wnm}^1$ is the modal vibration velocities of cylindrical shells in the z-directions.

Therefore, the modal vibration velocities corresponding to the nth-order circumferential mode can be expressed as

$$\mathbf{V}_n = [\mathbf{Z}_n]^{-1} \cdot [\mathbf{F}_n], \tag{24}$$

where F_n is an $M \times 1$ column vector that represents the modal excitation force corresponding to the nth-order circumferential mode, which includes two parts: a primary modal excitation force $\mathbf{F}_n^P$ that consists of a $Q \times 1$ column vector and a secondary modal excitation force $\mathbf{F}_n^S$ that consists of a $K \times 1$ column vector:

$$\mathbf{F}_n^P = \boldsymbol{\psi}_n^P \mathbf{f}_p = \begin{pmatrix} \varphi_{11}^P & \varphi_{12}^P & \cdots & \varphi_{1Q}^P \\ \varphi_{21}^P & \varphi_{22}^P & \cdots & \varphi_{2Q}^P \\ \cdots & \cdots & \cdots & \cdots \\ \varphi_{m1}^P & \varphi_{m2}^P & \cdots & \varphi_{mQ}^P \end{pmatrix} \begin{pmatrix} f_{p1} \\ f_{p2} \\ \cdots \\ f_{pQ} \end{pmatrix},$$

$$\mathbf{F}_n^S = \boldsymbol{\psi}_n^S \mathbf{f}_s = \begin{pmatrix} \varphi_{11}^S & \varphi_{12}^S & \cdots & \varphi_{1K}^S \\ \varphi_{21}^S & \varphi_{22}^S & \cdots & \varphi_{1K}^S \\ \cdots & \cdots & \cdots & \cdots \\ \varphi_{m1}^S & \varphi_{m2}^S & \cdots & \varphi_{mK}^S \end{pmatrix} \begin{pmatrix} f_{s1} \\ f_{s2} \\ \cdots \\ f_{sK} \end{pmatrix}, \tag{25}$$

where $\mathbf{f}_p$ represents the complex amplitude vector of the primary modal excitation force, $\mathbf{f}_s$ represents the complex amplitude vector of the secondary modal excitation force, and ψ_n^P and ψ_n^S represent primary and secondary modal force coordinate vectors corresponding to the nth-order circumferential mode, and their elements can be obtained using equation (5).

Consequently, equation (24) becomes

$$\widehat{V}_n = \widehat{V}_n^P + \widehat{V}_n^S = \mathbf{T}_p \mathbf{f}_p + \mathbf{T}_s \mathbf{f}_s, \tag{26}$$

where $\mathbf{T}_p = [\mathbf{Z}_n]^{-1} \psi_n^P$ and $\mathbf{T}_s = [\mathbf{Z}_n]^{-1} \psi_n^S$ represent the transfer functions between the structural response and the primary and secondary excitation forces, respectively.

Substituting equation (26) into equation (22), we obtain

$$W = \sum_{n=0}^{\infty} \widehat{V}_n{}^H \mathbf{M}_n \widehat{V}_n = \sum_{n=0}^{\infty} \left[\left(\mathbf{T}_p \mathbf{f}_p + \mathbf{T}_s \mathbf{f}_s \right)^H \mathbf{M}_n \left(\mathbf{T}_p \mathbf{f}_p + \mathbf{T}_s \mathbf{f}_s \right) \right]$$
$$= \mathbf{f}_p{}^H \sum_{n=0}^{\infty} \left(\mathbf{T}_p{}^H \mathbf{M}_n \mathbf{T}_p \right) \mathbf{f}_p + \mathbf{f}_p{}^H \sum_{n=0}^{\infty} \left(\mathbf{T}_p{}^H \mathbf{M}_n \mathbf{T}_s \right) \mathbf{f}_s$$
$$+ \mathbf{f}_s{}^H \sum_{n=0}^{\infty} \left(\mathbf{T}_s{}^H \mathbf{M}_n \mathbf{T}_p \right) \mathbf{f}_p + \mathbf{f}_s{}^H \sum_{n=0}^{\infty} \left(\mathbf{T}_s{}^H \mathbf{M}_n \mathbf{T}_s \right) \mathbf{f}_s. \tag{27}$$

The radiation sound power can be expressed as a quadratic function of the complex amplitude of the control input, i.e., the Hermitian quadratic form. Consequently, the optimal strength of the secondary source for active control can be obtained for the active control as follows:

$$\mathbf{f}_s = -\left[\sum_{n=0}^{\infty} \left(\mathbf{T}_s{}^H \mathbf{M}_n \mathbf{T}_s \right) \right]^{-1} \sum_{n=0}^{\infty} \left(\mathbf{T}_s{}^H \mathbf{M}_n \mathbf{T}_p \right) \mathbf{f}_p. \tag{28}$$

The calculated optimal secondary force can be inserted into equation (27), and the radiated sound power with active control can be obtained.

3. Results and Discussion

A finite cylindrical shell submerged in fluid is schematically shown in Figure 1. The structure is made of steel (density $\rho_s = 7850 \, \text{kg/m}^3$, Young's modulus $E = 2.1 \times 10^{10} \, \text{N/m}^2$, and Poisson's ratio $\sigma = 0.3$). The density and speed of sound of the fluid are $\rho_l = 1000 \, \text{kg/m}^2$ and $c_l = 1500 \, \text{m/s}$, respectively, for water. The structural damping is introduced by means of a complex elastic modulus, i.e., $E(1 - i\eta)$, where $\eta = 0.01$ is the damping loss factor of the shell. It is assumed that the radial excitation force is centered at a point $z_0 = 0.44$ and $\phi_0 = 0$. Its magnitude is 1 N and along the radial direction of the shell.

In order to evaluate the accuracy of the proposed model, the natural frequencies of a cylindrical shell in air and in water obtained here are compared with those from the literature and are listed in Table 1. Good agreement between values obtained from the present model with results from the literature can be observed.

3.1. Radiation Modal Characteristics. For a finite cylindrical shell with $L = 1.2 \, \text{m}$, $a = 0.4 \, \text{m}$, and $h = 0.003 \, \text{m}$, the surface is divided into 20×36 equal area units for the numerical calculations. Each radiation mode q_k has a different shape. Figure 2 shows the modal shapes of the first ten acoustic radiation modes for $kL = 1$.

As shown in Figure 2, the acoustic radiation modes of the submerged finite cylindrical shells are composed of

TABLE 1: Comparison of values of the natural frequency (Hz) for a shell $L = 1.284$ m, $a = 0.18$ m, and $h = 0.003$ m.

m	n	Air			Water		
		Ref. [39]	Ref. [40] *	Present	Ref. [39]	Ref. [40] *	Present
1	5	542.3	—	542.8	351.6	—	343
1	4	340.5	336.6	340.5	205.6	200.9	202
1	2	195.3	194.0	197.1	98.2	97.5	99
1	3	199.0	198.0	198.8	110.9	108.7	109
2	2	635.8	—	654.7	328.9	—	339
2	3	386.5	387.0	388.5	218.2	217.0	217
2	4	403.5	403.0	403.4	245.8	241.3	242
2	5	570.0	—	570.2	380.8	—	362
3	4	568.1	—	567.7	350.2	—	344

* Experimental results.
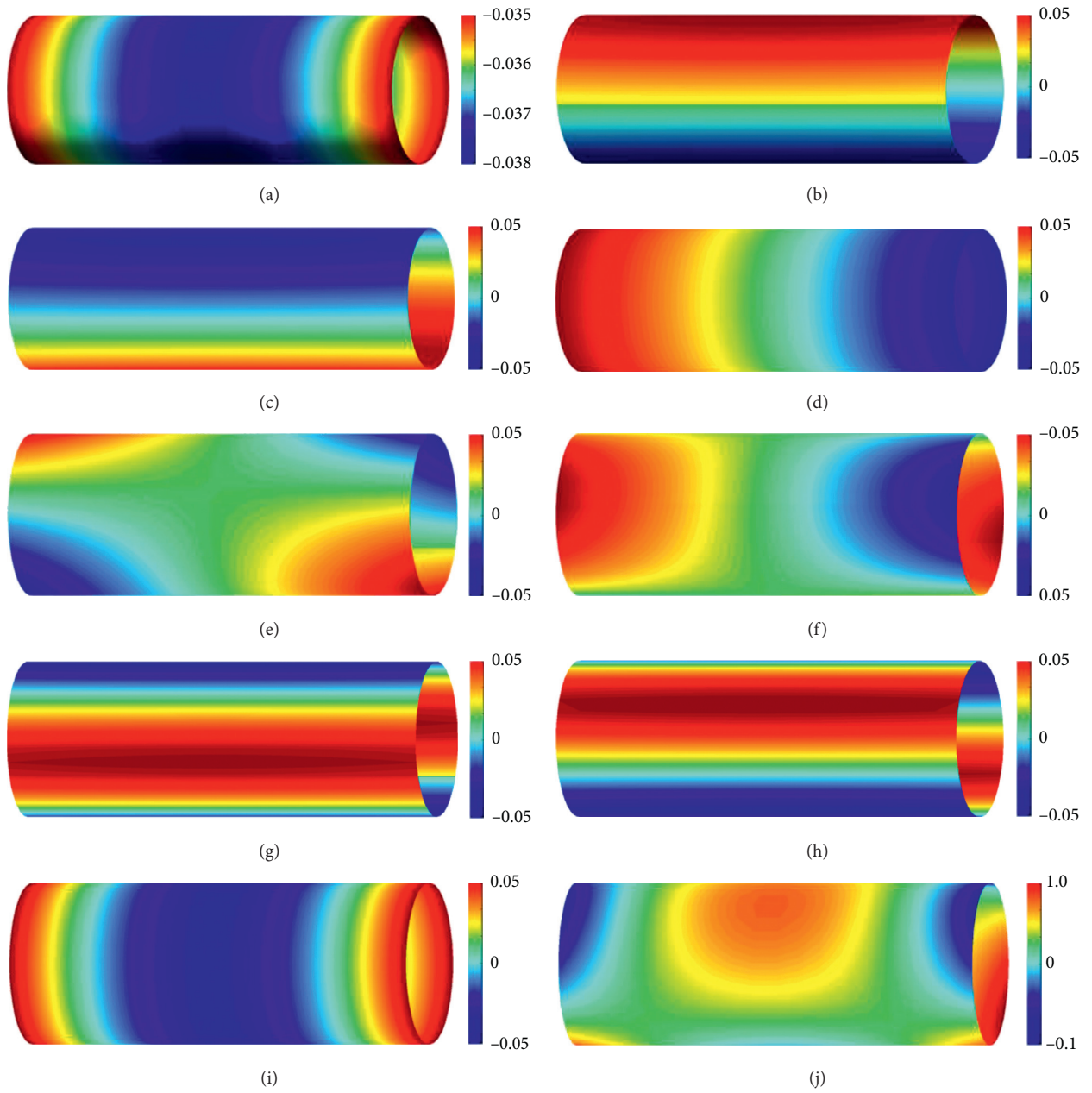
FIGURE 2: Modal shapes of the first ten a-modes ($kL = 1$) (a–j) for the modes from first to tenth.

symmetric and antisymmetric vibration modes. The velocity distribution corresponding to the first radiation mode is uniform in the middle of the shell, and the radiation type is similar to a monopole source. The velocity patterns corresponding to the second and third radiation modes are distributed uniformly along the axial direction and are symmetric and antisymmetric in the circumferential direction. Thus, these can be called circumferential dipole modes. The fourth radiation mode is an axial dipole mode, and the radiation modes from fifth to eighth are analogous with quadrupole modes. The fifth and six modes are compound axial and circumferential quadrupole modes, and the seventh and eighth radiation modes are circumferential quadrupole modes.

From equation (16), it is seen that if the surface velocity vector is expressed in terms of the vibration modes of the structure, the structure-dependent radiation mode shapes can reflect the relationship between radiation modes and vibration modes. The first ten axial and circumferential structural vibration modes occur within the frequency range of interest. In Figure 3, discrete integer values up to 100 on the horizontal axis represent cylindrical shell vibration modes (m, n) corresponding to $(1,0)$, $(1,1)$, $(1,2)$ ... $(1,9)$, $(2,0),(2,1)$, $(2,2)$, ..., $(10,9)$. The first six s-modes' shapes are rendered against the structural vibration modes in Figure 3.

Compared with the s-mode shapes of beams and plates [32], the s-mode shapes of a finite cylindrical shell with simply supported boundary conditions are more complicated, as shown in Figure 3. All the s-mode shapes possess many modal nodes, and each node corresponds to a structure vibration mode, i.e., if the sound power generated by a single s-mode is calculated, the vibration modes at the nodes do not contribute to the sound power generated by this s-mode, regardless of the velocity magnitude of these vibration modes, and only the vibration modes with nonzero values will contribute. At low frequencies, each s-mode is associated with a few vibration modes. It can be seen from Figure 3(a) that the first s-mode shapes possess peaks at modes 1, 21, 41, 61, and 81, corresponding to the structural vibration modes $(1, 0)$, $(3, 0)$, $(5, 0)$, $(7, 0)$, and $(9, 0)$ of the cylindrical shell. Thus, the sound power radiated from these vibration modes could be replaced by the sound power generated from the first s-mode. With the increase in the number of the axial vibration mode, the amplitude of the structure-dependent radiation modes decreases gradually, which indicates the contribution of the vibration modes to the amplitude of the structure-dependent radiation mode decrease. At the same time, the 4th s-mode corresponds to the same structural modes as well as the first s-mode; however, these two s-modes correspond to different dominant structural vibration modes. The dominant mode of the first s-mode corresponds to vibration mode $(1, 0)$, while the dominant mode of the 4th s-mode corresponds to vibration mode $(3, 0)$. It also can be seen from Figure 2 that the 1st and 4th a-modes in the circumferential direction are not pitch line and have similar circumferential vibration patterns, similar to the vibration modes with $n = 0$. In addition, the structural modes for $(1, 0)$, $(3, 0)$, $(5, 0)$, $(7, 0)$, and $(9, 0)$ tend to form dipole radiation. The 2nd s-modes mainly have

peaks at the 2, 22, 42, 62, and 82 vibration modes, which correspond to the vibration modes $(1,1)$, $(3,1)$, $(5,1)$, $(7,1)$, and $(9,1)$ of the cylindrical shell, respectively. The 3rd s-mode corresponds to the vibration modes $(2,0)$, $(4,0)$, $(6,0)$, $(8,0)$, and $(10,0)$. The 5th s-mode corresponds to the vibration modes $(2,1)$, $(4,1)$, $(6,1)$, $(8,1)$, and $(10,1)$. The 6th s-mode corresponds to the vibration modes $(1,2)$, $(3,2)$, $(5,2)$, $(7,2)$, and $(9,2)$ of the cylindrical shell. Comparing Figures 3(a) and 3(b), it can be seen that the order of the s-modes changes except the 1st and 4th s-modes. In Figure 3(b), the 2nd s-modes have peaks at the vibration modes $(2,0)$, $(4,0)$, $(6,0)$, $(8,0)$, and $(10,0)$. The 3rd s-mode corresponds to the vibration modes $(1,1)$, $(3,1)$, $(5,1)$, $(7,1)$, and $(9,1)$. The 5th s-mode corresponds to the vibration modes $(1,2)$, $(3,2)$, $(5,2)$, $(7,2)$, and $(9,2)$. The 6th s-mode corresponds to the vibration modes $(2,1)$, $(4,1)$, $(6,1)$, $(8,1)$, and $(10,1)$ of the cylindrical shell. Therefore, it indicates that the shapes of the s-modes can help to determine the coupling relationship between the structure-dependent radiation modes and the vibration modes at low frequencies.

Figure 4 compares the contributions of the radiation modes to the radiated sound power at low frequencies. According to the literature [32], the 1st radiation modes (either s-mode or a-mode) contribute to over 95% of the total power for the beam and plate structure in the low-frequency range. For the cylindrical shell examined in this work, the contribution of the 1st radiation mode to the radiated sound power of the cylindrical shell is the only dominant radiation mode below 80 Hz, and it is no longer the dominant radiation mode above 80 Hz. The 1st radiation mode corresponds to the vibration modes with the circumferential modal index ($n = 0$), which has relatively higher natural frequency than those of the $n > 0$ circumferential modes. Different from reference [15], it is impossible to achieve radiated sound power attenuation in the low-frequency range by only controlling the first radiation mode. The sound power from the first four a-modes only coincided at some natural frequencies, and there are large differences at other frequency values. The sound power from first eight a-modes has a greater contribution to the radiated sound power, and at some natural frequencies such as 393, 735, and 948 Hz, the difference is significant. As the number of radiation modes increases, the contribution to the sound power increases. The sound power from first twelve a-modes could approximately represent the total radiated sound power, while for s-modes, only the first ten s-modes are needed. For active control, fewer modes can be controlled to achieve a better control effect, and at the same time, fewer sensors are needed to detect these modes, thus simplifying the control system construction.

3.2. Active Control. Based on the theory described above, the sound power radiating from a submerged cylindrical shell before and after applying control by secondary force input is investigated through a numerical simulation in this section. The geometry and material parameters of the cylindrical shell are given in Section 3.1. The primary excitation forces and secondary control forces are both harmonic point forces

(a)

(b)
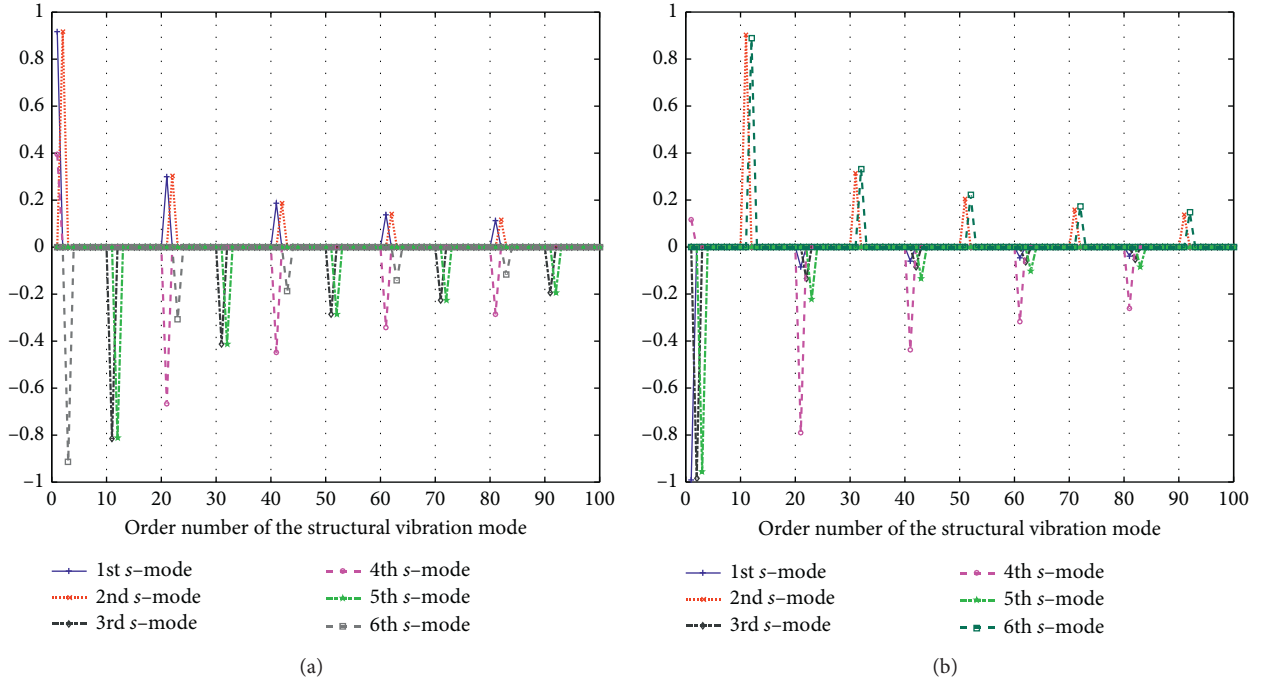
FIGURE 3: Modal shapes of the first six s-modes. (a) $kL = 1$; (b) $kL = 5$.

(a)

(b)
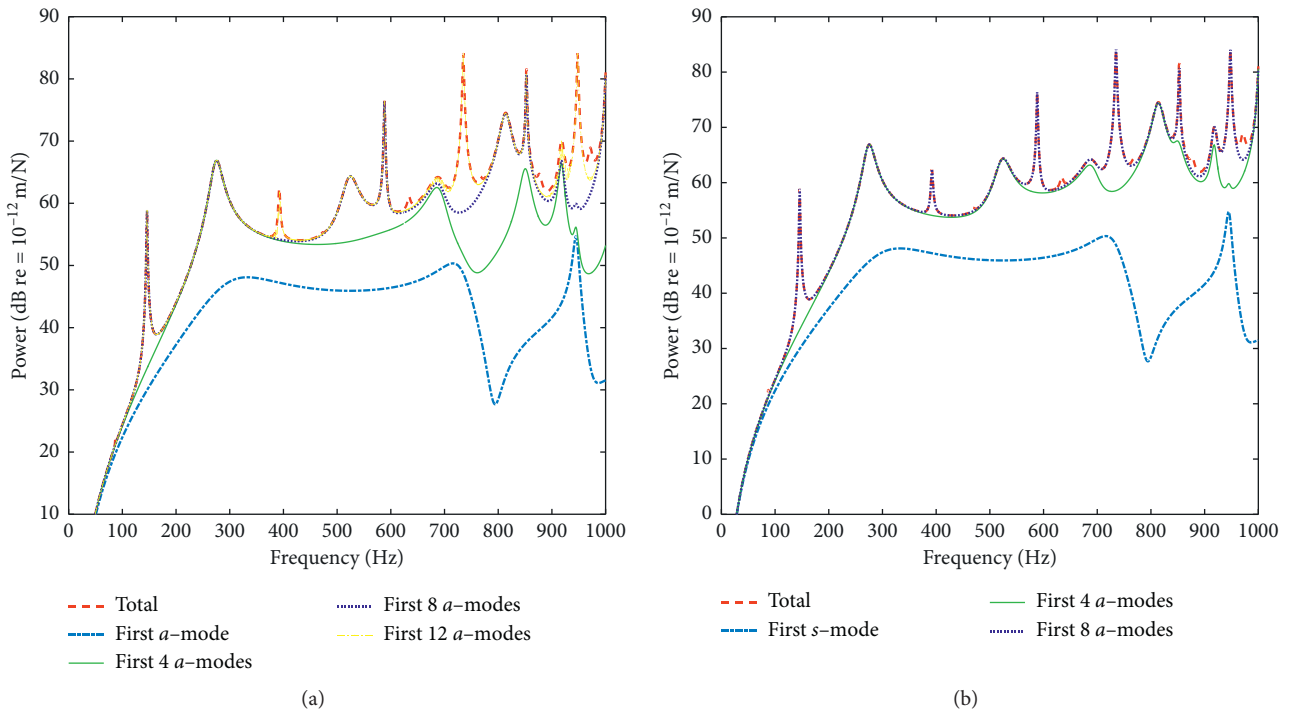
FIGURE 4: Radiated sound power from the first several a-modes and s-modes. (a) a-modes; (b) s-modes.

that are perpendicular to the surface of the shell. The position of the single primary excitation force is centered at a point $z_0 = 0.44$ and $\phi_0 = 0$, and its amplitude is 1 N. When two primary forces are used to excite the shell, the positions of the primary excitation forces are centered at a point $z_{01} = 0.44$ and $\phi_{01} = 0$ and $z_{02} = 0.3$ and $\phi_{02} = 0$, respectively,

and the amplitudes are all 1 N. The minimization of the total sound power radiating from the cylindrical shell under primary excitation forces and secondary control forces is set as the target function. The amplitude and phase of the optimal control force are calculated using equation (28). The radiated sound power of the submerged finite cylindrical
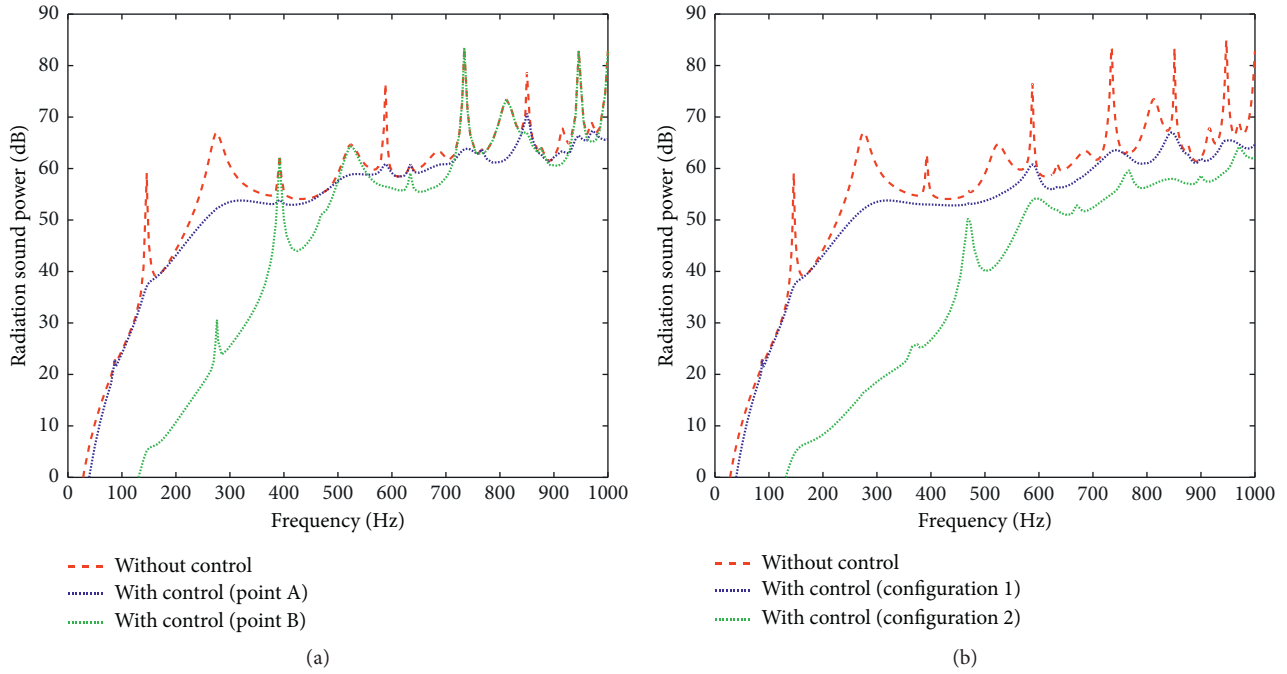
FIGURE 5: Effects of different positions and configurations of control force. (a) Single secondary control force. (b) Two secondary control forces.
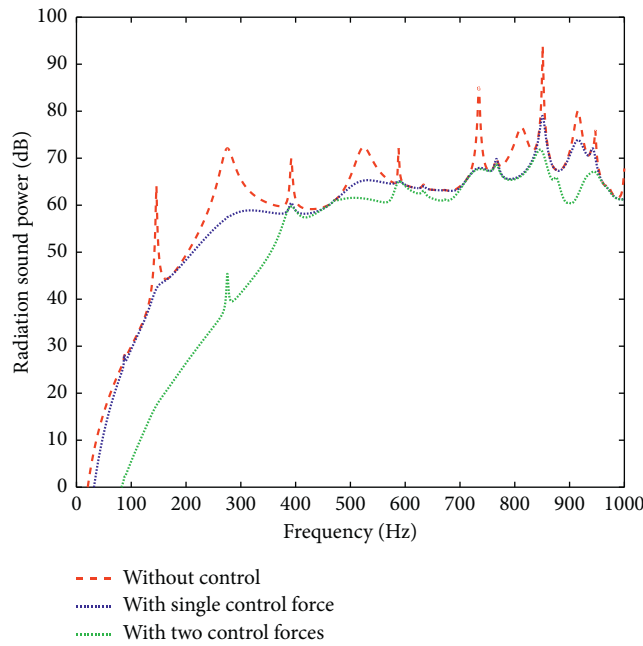
FIGURE 6: Comparison of control effects under multiple primary excitation forces.

shell before and after active control can be solved. Here, one and two secondary control forces are used for active control. First, when one force is used as a control force, the control effects of the secondary forces at different positions are compared. The effects of the two secondary control forces are also investigated. Figure 5 shows effects of different positions and configurations of control force under the

single primary excitation force. Figure 5(a) shows the sound power radiating from the cylindrical shell before and after active control by different positions of the control forces located at point A (0.76, 180°) and B (0.6, 0°). Figure 5(b) shows the radiated sound power before and after active control by different configurations of the two control forces. One configuration consisted of two control forces located at
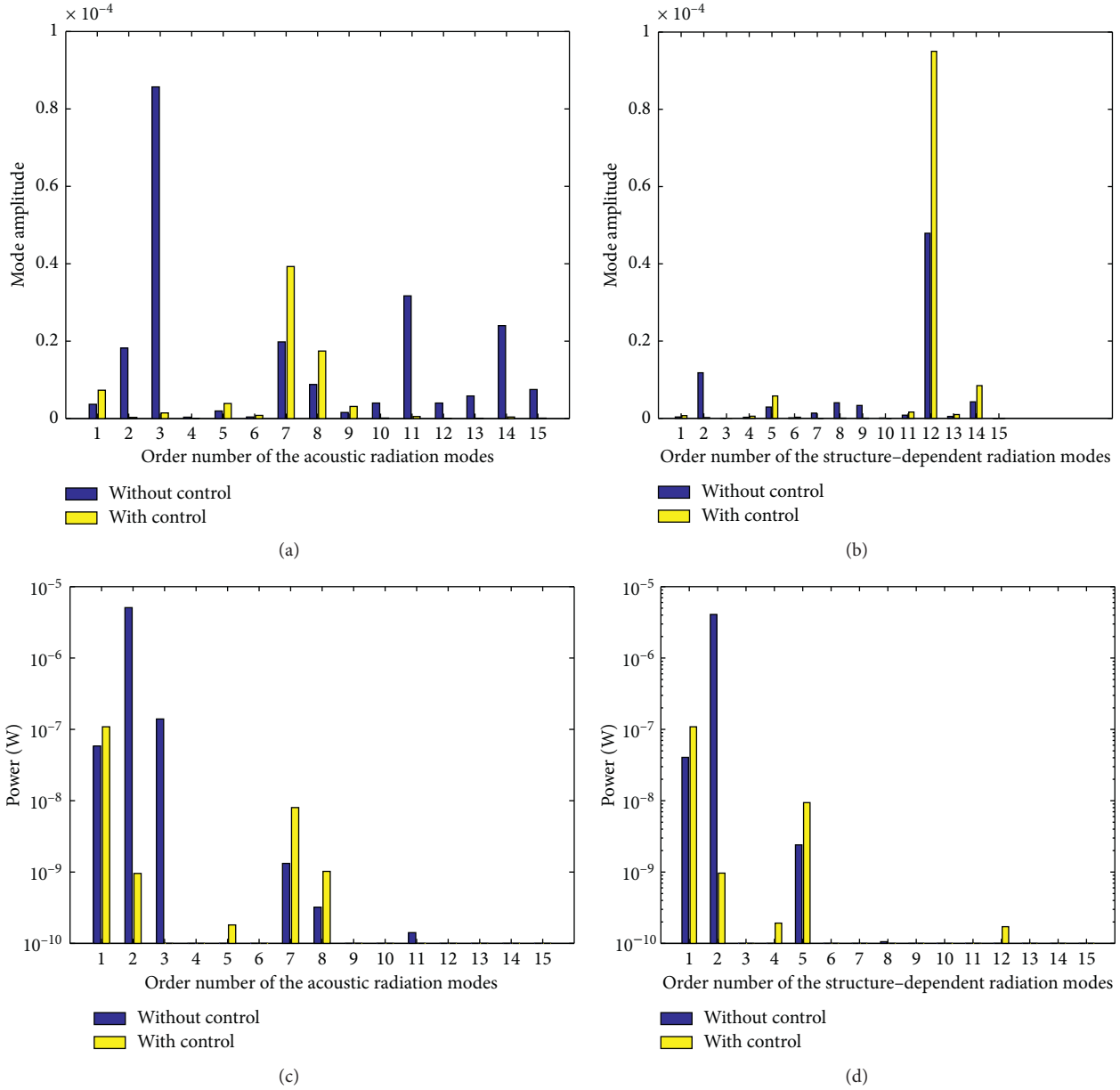
FIGURE 7: Amplitude and sound power of the *a*-modes and *s*-modes at resonance frequency (276 Hz). (a) Amplitude of the *a*-modes. (b) Amplitude of the *s*-modes. (c) Sound power of the *a*-modes. (d) Sound power of the *s*-modes.

point A (0.76, 180°) and C (0.44, 180°), and the other consisted of two control forces located at point A (0.76, 180°) and D (0.6, 0°). Figure 6 compared the control effects of two control forces under multiple primary excitation forces, and the single control force is located at point A (0.76, 180°), and the two control forces are located at point A (0.76, 180°) and C (0.9, 0°).

When a single primary force is used to excite the shell and a single secondary control force located at point A is used for active control, the peaks of the radiated sound power at most resonance frequencies have significant attenuation, as shown in Figure 5(a). With the single secondary control force located at point B, the larger attenuation appears in the low-frequency range. In the range

from 380 to 1000 Hz, the control effect is unsatisfactory at resonance frequencies and not as good as that with the secondary force located at point A. The main reason for this is that the secondary force located at point A is at the antinodal line relative to primary excitation forces, but the secondary force located at point B is at the nodal line of the even-order axial vibration modes. Therefore, the optimal control effect may be achieved by searching for the optimal position of the secondary control force. Comparing the results shown in Figures 5(a) and 5(b), it is evident that the radiated sound power in the frequency range of interest is reduced significantly by the two control forces, and the control effect is superior to single control force. In addition, the position of the two secondary control forces also has a
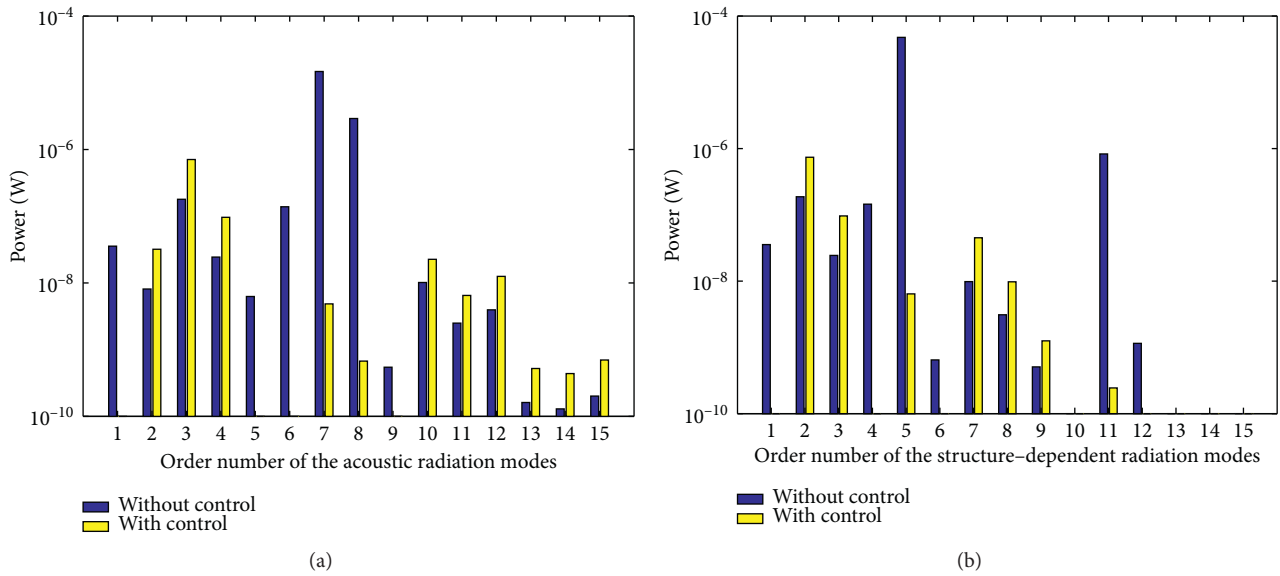
FIGURE 8: Sound power of the *a*-modes and *s*-modes at resonance frequency (588 Hz). (a) Sound power of the *a*-modes. (b) Sound power of the *s*-modes.

significant influence on the control effect. It can be seen from Figure 6 that there also have good control effects at most resonant frequencies for single control force when two primary forces are used to excite the shell. The results suggest that the control effect can be improved by increasing the number of control forces for the entire frequency band. The results show that the sound power radiated from the submerged vibrating cylindrical shell could be attenuated by suppressing the vibrating parts of the shell through the vibrators placed on the shell used to generate the secondary control force. For the shell subjected to a complex excitation, the structural acoustic radiation may be controlled by placing multiple exciters and optimizing the position, input amplitude, and phase of the vibration exciters.

3.3. Physical Mechanism of Active Control. To understand the influence of the modal amplitude on the sound power radiated from the cylindrical shell before and after active control, the control mechanisms are analyzed from the perspective of the radiation modes. In this section, the primary excitation force is the same as that in the previous section, and a single radial force is used as a secondary control force located at position A on the cylindrical shell. Modal amplitude changes at the resonance frequencies of 276 Hz (1,1) and 588 Hz (3,2) and the nonresonance frequency of 500 Hz are considered as examples. The amplitude and sound power of the *a*-modes and *s*-modes at these frequencies are shown in Figures 7–9. The blue bars of the column plot represent the modal amplitude and sound power before control, and the yellow bars represent those after control.

As shown in Figures 7(a) and 7(b), there is only one dominant peak of the first 15 *a*-modes and *s*-modes at the resonance frequency of 276 Hz before control, the 2nd *a*-mode and the 12th *s*-mode. After applying the control, the amplitude of the 2nd *a*-mode decreases sharply, while the

amplitude of the 12th *s*-mode increases. This indicates that the 12th *s*-mode is not the dominant mode. According to equations (12) and (20), the contribution of the *a*-mode or *s*-mode on the sound radiation power is determined by the multiplication of the radiation coefficient and amplitude of the radiation mode. Consequently, we must calculate the radiated sound power for each *a*-mode and *s*-mode. Figures 7(c) and 7(d) show the radiated sound power of the first 15 *a*-modes and *s*-modes before and after applying control. For the *a*-modes, the maximum peaks of the sound power as well as amplitude of the radiation mode occur for the second-order mode. Different from the amplitude of the *s*-modes, the maximum peak of the sound power of the *s*-modes occurs for the second-order mode and decreases significantly after control is applied, which shows the 2nd *s*-mode is the dominant mode at 276 Hz. In the subsequent analysis, the radiated sound power for each *a*-mode and *s*-mode before and after control is used to display the control mechanism.

Figures 8(a) and 8(b) show the amplitude and power of the *a*-modes and *s*-modes at the resonance frequency of 588 Hz. In Figure 8(a), the 7th and 8th *a*-modes have higher amplitudes, and these two modes are pairs of acoustic radiation modes with the same modal shape but a 90° phase shift, as shown in Figure 2. After applying control, the sound power in the 7th and 8th *a*-modes decreases. As shown in Figure 8(b), the 5th *s*-mode is the dominant structure-dependent radiation mode, and the amplitude that attenuates significantly after control is applied.

Furthermore, Figures 9(a) and 9(b) show that the sound power radiated from some *s*-modes or *a*-modes decrease after applying control at nonresonance frequency. When some radiation modal sound power increase, the sum of the sound power from all the radiation modes remains almost unchanged before and after control. This occurs mainly because there is no dominant structural vibration mode at the nonresonance frequency and no dominant radiation
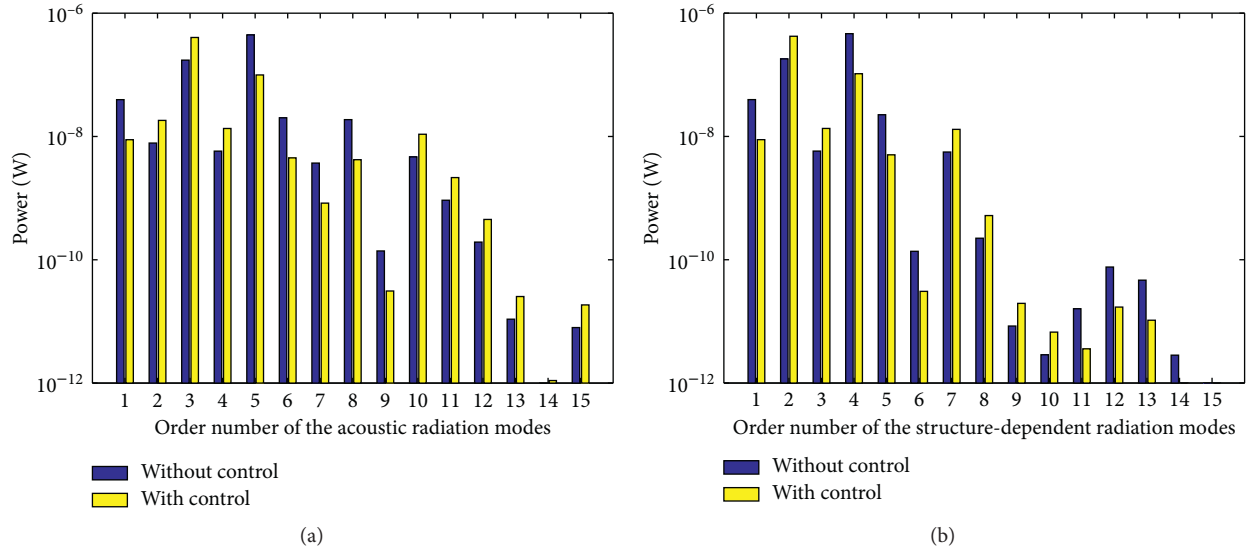
FIGURE 9: Sound power of the *a*-modes and *s*-modes at nonresonance frequency (500 Hz). (a) Sound power of the *a*-modes. (b) Sound power of the *s*-modes.

mode. In particular, Figure 9(a) shows that the 3rd and 5th *a*-modes contribute more to the radiated sound power than the other modes. After applying control, the radiated sound power for the 3rd *a*-mode increases, while that of the 5th *a*-mode decreases. The *s*-modes are slightly different from the *a*-modes. As shown in Figure 9(b), the peaks of the radiated sound power correspond to the 2nd and 4th *s*-modes. The sound power radiation of the 2nd *s*-mode increases, while that of the 5th *a*-mode decreases after control is applied.

Therefore, when the minimum of the total sound power radiating from a cylindrical shell is considered as the control target, the mechanism of active control is used to reduce the sound power of the dominant *a*-modes or *s*-modes corresponding to structural vibration modes, while ensuring that the magnitude of the nondominant radiation modes is not significantly increased, allowing the sound radiation of the vibrating structure to be controlled.

4. Conclusion

The radiation characteristics and active structural acoustic control of a submerged cylindrical shell at low frequencies are investigated by means of the radiation modes. The contribution of the low-order radiation modes to the radiated sound power is discussed. The results show that the sound power radiated from a group of specific vibration modes can be replaced by that generated through one *a*-mode or *s*-mode. The performance of the sound power radiated from individual radiation modes decreases with the increase in the mode number. Only the first few radiation modes contribute to the

sound power radiated from a submerged finite cylindrical shell at low frequencies. However, the contribution of the first radiation mode of the cylindrical shell to the radiated sound power at the low frequency is not always dominant mode, especially at higher resonant frequencies.

The active structural acoustic control of a submerged finite cylindrical shell is investigated by considering the fluid-structure coupled interaction. The analytical expression of the optimal complex amplitude of the secondary force is derived based on the uncoupled characteristics of the radiated sound power in the circumferential direction, and the control effects with one and two control forces are also compared. Moreover, the physical mechanism of the active structural acoustic control of the submerged finite cylindrical shell is analyzed based on the radiation modes. The results show that a greater reduction is achieved using multiple secondary forces by controlling the vibration of the shell, which effectively produces the sound radiation. The physical mechanism of the active control is to reduce the amplitude of the radiation modes corresponding to the structural vibration modes, thereby effectively controlling the sound radiated due to structural vibrations.

Appendix

A. Flügge Operator

The elements of the Flügge operator $\mathbf{L}_{3\times3}$ in equation (1) are given as

$$L_{11} = a^2\frac{\partial^2}{\partial z^2} + \left(\frac{1-\sigma}{2}\right)(1+\beta)\frac{\partial^2}{\partial\phi^2} - \frac{\rho_s a^2\left(1-\sigma^2\right)}{E^*}\frac{\partial^2}{\partial t^2},$$

$$L_{12} = L_{21} = a\frac{1+\sigma}{2}\frac{\partial^2}{\partial z\partial\phi},$$

$$L_{13} = L_{31} = \sigma a\frac{\partial}{\partial z} + \beta a\frac{(1-\sigma)}{2}\frac{\partial^3}{\partial z\partial\phi^2} - ka^3\frac{\partial^3}{\partial z^3},$$

$$L_{22} = a^2\frac{1-\sigma}{2}(3\beta+1)\frac{\partial^2}{\partial z^2} + \frac{\partial^2}{\partial\phi^2} - \frac{\rho a^2\left(1-\sigma^2\right)}{E^*}\frac{\partial^2}{\partial t^2},$$

$$L_{23} = L_{32} = \frac{E^*h}{a^2\left(1-\sigma^2\right)}\left(\frac{\partial}{\partial\phi} - \beta a^2\frac{(3-\sigma)}{2}\frac{\partial^3}{\partial\phi\partial z^2}\right),$$

$$L_{33} = 1 + \beta + 2\beta\frac{\partial^2}{\partial\phi^2} + \beta\nabla^4 - \frac{\rho a^2\left(1-\sigma^2\right)}{\widetilde{E}}\frac{\partial^2}{\partial t^2},$$

$$\text{(A.1)}$$

where $\nabla^4 = a^4\left(\partial^4/\partial z^4\right) + 2a^2\left(\partial^4/\partial z^2\partial\phi^2\right) + \left(\partial^4/\partial\phi^4\right)$, $\beta = h^2/12a^2$, and ρ_s denotes the density of the cylindercal shell.

B. The Expression for Modal Sound Pressure

It is assumed that a finite-length cylindrical shell with simple supports at both ends is immersed in an irrotational, nonviscous, and compressible fluid. The vibration of the shell causes the vibration of the surface medium, and the sound field is generated. For the steady-state problem, the pressure field satisfies the acoustic wave equation in cylindrical coordinates:

$$\nabla^2 p_a + k^2 p_a = 0, \tag{B.1}$$

where ∇^2 is the Laplace operator in cylindrical coordinates.

According to the continuity condition, the radial velocity of the fluid is equal to the radial vibration velocity of the structure on the contact surface between the fluid and the structure, and no cavitation is assumed at the fluid-shell interface at $r = a$:

$$\frac{\partial p_a}{\partial r}\Big|_{r=a} = \rho_l\omega^2 C_{wnm}^\alpha. \tag{B.2}$$

The Sommerfeld radiation condition is satisfied at an infinite distance:

$$\lim_{r\to\infty} r\left(\frac{\partial p_a}{\partial r} + ikp_a\right) = 0. \tag{B.3}$$

The Green's function satisfies the Neumann boundary condition for a finite-length cylindrical shell with an infinite barrier. Thus, the radiated sound pressure of the cylindrical shell is expressed as

$$p_a(\mathbf{r}) = -i\rho_l\omega\iint G\left(\frac{\mathbf{r}}{\mathbf{r}_0}\right)\dot{w}(\mathbf{r}_0)dS, \tag{B.4}$$

where $\mathbf{r}$ denotes the points on the outside of the cylindrical shell and $\mathbf{r}_0$ denotes the points on the cylindrical shell.

In cylindrical coordinates, Green's function satisfying the above equation can be expressed as

$$G\left(\frac{\mathbf{r}}{\mathbf{r}_0}\right) = -\frac{1}{4\pi^2}\sum_{n=0}^\infty\varepsilon_n\cos\left[n(\phi-\phi_0)\right]\cdot\int_{-\infty}^\infty\frac{H_n^{(1)}\left(\sqrt{k^2-k_z^2}\,r\right)}{\sqrt{k^2-k_z^2}\,aH_n^{(1)}\left(\sqrt{k^2-k_z^2}\,a\right)}e^{jk_z(z-z_0)}dk_z. \tag{B.5}$$

By substituting $w(z,\phi)$ in equations (2) and (B.5) into equation (B.4), the radiated sound pressure of a cylindrical shell of finite length simply supported at both ends can be obtained:

$$p_a(\mathbf{r}) = \frac{\omega^2\rho_l}{2\pi}\sum_{\alpha=0}^1\sum_{n=0}^\infty\sum_{m=1}^\infty C_{wnm}^\alpha\sin\left(n\phi+\frac{\alpha\pi}{2}\right)\int_{-\infty}^\infty\widetilde{Z}(k_z)\psi_m(k_z)e^{ik_zz}dk_z, \tag{B.6}$$

where

$$\psi_m(k_z) = \int_0^L\sin\left(\frac{m\pi z}{L}\right)e^{-ik_zz}dz. \tag{B.7}$$

At the surface of the cylindrical shell, the surface sound pressure of the shell can be expanded according to the mode function of the cylindrical shell:

$$p_a = \sum_{\alpha=0}^1\sum_{m=1}^\infty\sum_{n=1}^\infty P_{mn}^\alpha\sin\left(n\phi_0+\frac{\alpha\pi}{2}\right)\sin(k_mz_0). \tag{B.8}$$

According to the radiated sound pressure of the cylindrical shell, the surface modal sound pressure can be expressed by using the orthogonality of trigonometric functions as

$$P_{mn}^\alpha = -i\omega a\sum_{q=1}^\infty C_{wmn}^\alpha Z_{qmn}, \tag{B.9}$$

where Z_{qmn} is the radiation impedance, which expresses the modal coupling between the different axial modal indices (m and q) due to the fluids.

Data Availability

The data used to support the findings of this study are included within this article.

Conflicts of Interest

The authors declare that they have no conflicts of interest.

Acknowledgments

References

[1] B. Laulagnet and J. L. Guyader, "Sound radiation by finite cylindrical ring stiffened shells," *Journal of Sound and Vibration*, vol. 138, no. 2, pp. 173–191, 1990.

[2] P. R. Sepanishen, "Radiated power and radiation loading of cylindrical surfaces with non-uniform velocity distributions," *Journal of the Acoustical Society of America*, vol. 63, no. 2, pp. 328–338, 1978.

[3] B. Laulagnet and J. L. Guyader, "Modal analysis of a shell's acoustic radiation in light and heavy fluids," *Journal of Sound and Vibration*, vol. 131, no. 3, pp. 397–415, 1989.

[4] F. Bérot and B. Peseux, "Vibro-acoustic behavior of submerged cylindrical shells: analytical formulation and numerical model," *Journal of Fluids and Structures*, vol. 12, no. 8, pp. 959–1003, 1998.

[5] M. Caresta and N. J. Kessissoglou, "Structural and acoustic responses of a fluid-loaded cylindrical hull with structural discontinuities," *Applied Acoustics*, vol. 70, no. 7, pp. 954–963, 2009.

[6] M. C. Junger, "Radiation loading of cylindrical and spherical surfaces," *The Journal of the Acoustical Society of America*, vol. 24, no. 3, pp. 288–289, 1952.

[7] B. E. Sandman, "Fluid-loading influence coefficients for a finite cylindrical shell," *The Journal of the Acoustical Society of America*, vol. 60, no. 6, pp. 1256–1264, 1976.

[8] M. Amabili, "Flexural vibration of cylindrical shells partially coupled with external and internal fluids," *Journal of Vibration and Acoustics*, vol. 119, no. 3, pp. 476–484, 1997.

[9] M. Amabili, "Vibrations of circular tubes and shells filled and partially immersed in dense fluids," *Journal of Sound and Vibration*, vol. 221, no. 4, pp. 567–585, 1999.

[10] M. Amabili, *Nonlinear Vibrations and Stability of Shells and Plates*, Cambridge University Press, New York, NY, USA, 2008.

[11] M. K. Kwak, "Free vibration analysis of a finite circular cylindrical shell in contact with unbounded external fluid," *Journal of Fluids and Structures*, vol. 26, no. 3, pp. 377–392, 2010.

[12] K. Naghshineh, W. Chen, and G. H. Koopmann, "Use of acoustic basis functions for active control of sound power radiated from a cylindrical shell," *The Journal of the Acoustical Society of America*, vol. 103, no. 4, pp. 1897–1903, 1998.

[13] J. P. Maillard and C. R. Fuller, "Active control of sound radiation from cylinders with piezoelectric actuators and structural acoustic sensing," *Journal of Sound and Vibration*, vol. 222, no. 3, pp. 363–387, 1999.

[14] X. Pan, Y. Tso, and R. Juniper, "Active control of low-frequency hull–radiated noise," *Journal of Sound and Vibration*, vol. 313, no. 2, pp. 29–45, 2008.

[15] A. Loghmani, M. Danesh, M. K. Kwak, and M. Keshmiri, "Active control of radiated sound power of a smart cylindrical shell based on radiation modes," *Applied Acoustics*, vol. 114, no. 1, pp. 218–229, 2016.

[16] M. Caresta and N. J. Kessissoglou, "Active control of sound radiated by a submarine hull in axisymmetric vibration using inertial actuators," *Journal of Vibration and Acoustics*, vol. 81, pp. 1–8, 2012.

[17] Y. Cao, H. Sun, F. Y. An, and X. Li, "Active control of low-frequency sound radiation by cylindrical shell with piezoelectric stack force actuators," *Journal of Sound and Vibration*, vol. 331, no. 11, pp. 2471–2484, 2012.

[18] M. X. Chen, D. P. Luo, G. Cao, F. Zhou, and H. L. Guo, "Sound radiation analysis of low order modes from finite stiffened double cylindrical shells," *Journal of Harbin Engineering University*, vol. 25, no. 4, pp. 446–450, 2004.

[19] T. R. Lin, M. Chris, and O. S. Peter, "Characteristics of modal sound radiation of finite cylindrical shells," *Journal of Vibration and Acoustics*, vol. 133, no. 5, pp. 1–6, 2011.

[20] H. Peters, N. J. Kessissoglou, and S. Marburg, "Modal decomposition of exterior acoustic-structure interaction," *Journal of the Acoustical Society of America*, vol. 133, no. 5, pp. 2668–2677, 2013.

[21] O. M. Fein, L. Gaul, and U. Stobener, "Vibration reduction of a fluid-loaded plate by modal control," *Journal of Intelligent Material Systems and Structures*, vol. 16, no. 6, pp. 541–552, 2005.

[22] S. Li, "Active modal control simulation of vibro-acoustic response of a fluid-loaded plate," *Journal of Sound and Vibration*, vol. 330, no. 23, pp. 5545–5557, 2011.

[23] S. J. Elliott and M. E. Johnson, "Radiation modes and the active control of sound power," *Journal of the Acoustical Society of America*, vol. 94, no. 4, pp. 2194–2204, 1993.

[24] K. A. Cunefare, "Effect of modal interaction on sound radiation from vibrating structures," *AIAA Journal*, vol. 30, no. 12, pp. 2819–2828, 1992.

[25] K. A. Cunefare and M. N. Currey, "On the exterior acoustic radiation modes of structures," *Journal of the Acoustical Society of America*, vol. 96, no. 4, pp. 2302–2312, 1994.

[26] K. A. Cunefare, M. N. Currey, M. E. Jonhson, and S. J. Elliott, "The radiation efficiency grouping of free-space acoustic radiation modes," *Journal of the Acoustical Society of America*, vol. 109, no. 1, pp. 203–215, 2001.

[27] K. Naghshineh and G. H. Koopmann, "Active control of sound power using acoustic basis functions as surface velocity filters," *Journal of the Acoustical Society of America*, vol. 93, no. 5, pp. 2740–2752, 1993.

[28] W. R. Johnson, P. Aslani, and D. R. Hendricks, "Acoustic radiation mode shapes for control of plates and shells," *Journal of the Acoustical Society of America*, vol. 133, no. 5, pp. 3385-3386, 2013.

[29] D. R. Wilkes, H. Peters, P. Croaker, S. Marburg, A. J. Duncan, and N. Kessissoglou, "Non-negative intensity for coupled fluid–structure interaction problems using the fast multipole

method," *Journal of the Acoustical Society of America*, vol. 141, no. 6, pp. 4278–4288, 2017.

[30] S. H. Ding, K. A. Chen, and X. Y. Ma, "Analysis of low frequency radiation characteristics of a finite cylindrical shell based on vibration and radiation modes," in *Proceedings of the 21st International Congress on Sound and Vibration*, pp. 13–17, Beijing, China, July, 2014.

[31] D. M. Photiadis, "The relationship of singular value decomposition to wave-vector filtering in sound radiation problems," *Journal of the Acoustical Society of America*, vol. 88, no. 2, pp. 1152–1159, 1990.

[32] L. Ji and J. S. Bolton, "Sound power radiation from a vibrating structure in terms of structure-dependent radiation modes," *Journal of Sound and Vibration*, vol. 335, pp. 245–260, 2015.

[33] X. Pan, Y. Tso, and R. Juniper, "Active control of radiated pressure of a submarine hull," *Journal of Sound and Vibration*, vol. 311, no. 1-2, pp. 224–242, 2008.

[34] M. Caresta and N. J. Kessissoglou, "Active control of sound radiated by a submarine in bending vibration," *Journal of Sound and Vibration*, vol. 330, no. 4, pp. 615–624, 2011.

[35] X. L. Ma, G. Y. Jin, and Z. G. Liu, "Active structural acoustic control of an elastic cylindrical shell coupled to a two-stage vibration isolation system," *International Journal of Mechanical Sciences*, vol. 79, pp. 182–194, 2014.

[36] S. Merz, N. J. Kessissoglou, R. Kinns, and S. Marburg, "Passive and active control of the radiated sound power from a submarine excited by propeller forces *Journal of Ship Research*, vol. 57, no. 1, pp. 59–71, 2013.

[37] S. X. Liu and M. S. Zou, "Evaluation of radiation loading on finite cylindrical shells using the fast Fourier transform: a comparison with direct numerical integration," *Journal of the Acoustical Society of America*, vol. 143, no. 3, pp. 160–166, 2018.

[38] Y. Sun, T. J. Yang, and Y. H. Chen, "Sound radiation modes of cylindrical surfaces and their application to vibro-acoustics analysis of cylindrical shells," *Journal of Sound and Vibration*, vol. 424, pp. 64–77, 2018.

[39] P. Liu, "The impact of diving depth on vibration and acoustic radiation of cylinderical shell and research of similarity," Master's Thesis, Dalian University of Technology, Dalian, China, 2013.

[40] A. Ergin, W. G. Price, R. Randall, and P. Temarel, "Dynamic characteristics of a submerged, flexible cylinder vibrating in finite water depths," *Journal of Ship Research*, vol. 36, no. 2, pp. 154–167, 1992.

Research Article
A Dynamic Motion Tracking Control Approach for a Quadrotor Aerial Mechanical System

Hugo Yañez-Badillo [iD],[1] Francisco Beltran-Carbajal [iD],[2] Ruben Tapia-Olvera [iD],[3]
Antonio Valderrabano-Gonzalez [iD],[4] Antonio Favela-Contreras [iD],[5]
and Julio C. Rosas-Caro [iD][4]

[1]*Tecnológico de Estudios Superiores de Tianguistenco, División de Mecatrónica, Tianguistenco C.P. 52650, Estado de México,*
 Mexico City, Mexico
[2]*Universidad Autónoma Metropolitana, Unidad Azcapotzalco, Departamento de Energía, Azcapotzalco C.P. 02200,*
 Mexico City, Mexico
[3]*Universidad Nacional Autónoma de México, Departamento de Energía Eléctrica, C.P. 04510, Mexico City, Mexico*
[4]*Universidad Panamericana, Facultad de Ingeniería, Álvaro del Portillo 49, Zapopan, Jalisco 45010, Mexico*
[5]*Tecnologico de Monterrey, Escuela de Ingenieria y Ciencias, Monterrey, Nuevo León, Mexico*

Correspondence should be addressed to Francisco Beltran-Carbajal; fbeltran@azc.uam.mx

Received 3 October 2020; Revised 20 November 2020; Accepted 27 November 2020; Published 30 December 2020

Academic Editor: Pierangelo Masarati

This paper deals with the reference trajectory tracking problem and simultaneous active disturbance suppression on a class of controlled aerial mechanical systems by processing measurable output signals. A novel dynamic control method for desired motion reference trajectory tracking for quadrotor helicopters is introduced. Measurements of position output signals for efficient and robust tracking of motion profiles specified for the unmanned aerial vehicle are only required. Thus, differentiation of signals and real-time estimation of disturbances affecting the multi-input multioutput, underactuated nonlinear dynamic system are unnecessary. The presented active control approach can be directly extended for a class of vibrating mechanical systems. Analytical, experimental, and numerical results are presented to prove the satisfactory performance of the proposed trajectory tracking control approach for considerably perturbed operating scenarios.

1. Introduction

Interest in the study of unmanned aerial vehicles (UAVs) has increased in the last years since these aerial machines are able to accomplish several sorts of tasks. Diverse configurations of these vehicles can be found in multiple applications such as surveillance, monitoring, inspection, mapping, and payload transportation, among others [1, 2]. Efficient control of a four-rotor helicopter, commonly named quadrotor, has been addressed in various technological and scientific research works [3]. This vehicle is an underactuated nonlinear dynamic system because it counts with six degrees of freedom and only four independent control inputs. In contrast with other UAVs, such as the fixed-wing type that need large and wide space extensions for take-off and landing, a quadrotor has the ability of vertical take-off and landing (VTOL) which allows its safe operation indoors [4].

During flights, as a consequence of variable wind speeds, fluctuations in the surrounding humidity, and air resistance, quadrotors are subjected to endogenous and exogenous uncertainties due to a highly changing medium. A complex nonlinear dynamic behaviour between relevant variables and uncertainty is observed. Therefore, in order to efficiently perform trajectory tracking, slow and fast motion, hovering, stable flight, and VTOL, robust motion control schemes should be designed.

Numerous linear and nonlinear controllers have been proposed in the literature for quadrotor helicopters. In [5], PID and LQ control strategies have been implemented for stabilization of a quadrotor in presence of small perturbations. PID

control algorithms have been also introduced in [6], where results show a good flight performance for trajectory tracking at slow velocity in controlled environments. To regulate the rotational dynamics of a quadrotor in [7], a backstepping-based PID nonlinear control has been introduced, where the tracking error integral is used to minimize the steady-state error. The work in [8] deals with the regulation of the quadrotor position by using a robust PID controller, while robust attitude control is achieved by means of integral backstepping and terminal sliding modes.

Indeed, synthesis of several high-efficiency nonlinear control schemes may require accurate mathematical models or have a complex structure, which complicate their implementation in realistic systems due to some variables and parameters are unavailable or hard to obtain [9]. Thus, the Active Disturbance Rejection Control (ADRC) methodology constitutes an excellent alternative to achieve robustness against a wide class of disturbances [10]. Effective online disturbance estimation represents a fundamental component in ADRC [11, 12]. In this regard, in [13], disturbances are estimated by a Linear Extended State Observer (LESO) and then compensated by a PD controller. Authors in [14] propose an active disturbance rejection sliding mode controller, compensating estimates of uncertainties and external disturbances. Meanwhile, authors in [15] put all the available process information as an input in the control scheme for improving the disturbance estimation. In [16], satisfactory results to stabilize a quadrotor are achieved with a modified nonlinear version of ADRC.

In this paper, a new robust motion tracking control approach for a multiinput multioutput, underactuated nonlinear four-rotor helicopter is introduced. In contrast with other recent contributions, in the present dynamic tracking control proposal, additional designs of asymptotic extended state observers for real-time estimation of both disturbances and unavailable states signals are unnecessary. External disturbances and model uncertainties are actively suppressed through polynomial signal compensators, injected directly by suitable action of constrained, and reduced dynamic control inputs. Dynamic compensators are exploited to add outstanding active disturbance suppression capabilities. Integral structural reconstruction of unavailable time derivatives in the proposed control scheme is properly extended as well [17]. Effectiveness of integral reconstruction of velocity signals on efficiently controlled nonlinear vibrating systems has been proved in [18, 19]. Robustness of integral error action on electric motor control has been discussed in [20, 21]. In the present study, important insights for extension of the dynamic tracking control approach for a class of mechanical systems are also provided.

The remainder of this paper is organized as follows. In Section 2, an experimental case study on central ideas of the reference trajectory tracking control approach is described. The MIMO underactuated nonlinear dynamic model of the aerial vehicle is presented in Section 3. Then, active disturbance suppression is addressed by means of the proposed robust motion tracking control scheme in Section 4. In Section 5, three case studies are presented to demonstrate the efficiency and robustness of the introduced dynamic control scheme in presence of considerable disturbances. Lastly, conclusions and future work are highlighted in Section 6.

2. An Output Feedback Dynamic Control Approach

To depict the basic ideas of the proposed dynamic tracking control approach, consider the n Degree-of-Freedom (DOF) mass-spring-damper mechanical system shown in Figure 1. Here, x_i, $i = 1, 2, \ldots, n$, stands for position of the mass m_i, $y = x_1$ represents the output variable to be controlled, and u is a single force control input. Mass, damping, and stiffness parameters associated with the i-th DOF are denoted by m_i, k_i, and c_i, respectively.

The mathematical model of this multi-degree-of-freedom vibrating mechanical system is described by

$$\mathbf{M}\ddot{\mathbf{x}} + \mathbf{C}\dot{\mathbf{x}} + \mathbf{K}\mathbf{x} = \mathbf{u}, \tag{1}$$

where $\mathbf{M}$, $\mathbf{C}$, and $\mathbf{K}$ are, respectively, the mass, damping, and stiffness matrices given by

$$
\mathbf{M} = \begin{bmatrix} m_1 & 0 & 0 & \ldots & 0 & 0 \\ 0 & m_2 & 0 & \ldots & 0 & 0 \\ \vdots & & \ddots & & & \\ 0 & 0 & 0 & \ldots & m_{n-1} & 0 \\ 0 & 0 & 0 & \ldots & 0 & m_n \end{bmatrix},
$$

$$
\mathbf{C} = \begin{bmatrix} c_1 & 0 & 0 & \ldots & 0 & 0 \\ 0 & c_2 & 0 & \ldots & 0 & 0 \\ \vdots & & \ddots & & & \\ 0 & 0 & 0 & \ldots & c_{n-1} & 0 \\ 0 & 0 & 0 & \ldots & 0 & c_n \end{bmatrix},
$$

$$
\mathbf{K} = \begin{bmatrix} k_1 + k_2 & -k_2 & 0 & \ldots & 0 & 0 & 0 \\ -k_2 & k_2 + k_3 & -k_3 & \ldots & 0 & 0 & 0 \\ \vdots & & & & & & \\ 0 & 0 & 0 & \ldots & -k_{n-1} & k_{n-1} + k_n & -k_n \\ 0 & 0 & 0 & \ldots & 0 & -k_n & k_n + k_{n+1} \end{bmatrix},
$$

$$\tag{2}$$

with position vector $\mathbf{x} = [x_1 x_2 \ldots x_n]^T$ and control force vector $\mathbf{u} = [u \ 0 \ \ldots \ 0]^T$. Notice that equation (1) has been widely employed to model diverse engineering systems such as dynamic vibration absorbers [22, 23] and flexible structures [24].

Then, from equation (1), the following feedforward and feedback controller for asymptotic tracking of the desired reference position trajectory $y^*(t)$ can be synthesized:

$$u = m_1 \left[\ddot{y}_1^* - \beta_1 (\dot{y} - \dot{y}^*) - \beta_0 (y - y^*) - \xi(t) \right], \tag{3}$$

where β_0 and β_1 are control gains and $\xi(t)$ is disturbance affecting the dynamics of the actively controlled output variable y. Notice that $\xi(t)$ includes disturbances due to unmodeled dynamics and, possibly, parametric uncertainty and resonant excitation forces. Nevertheless, the trajectory tracking controller (3) requires measurements of position, velocity, and information of disturbances $\xi(t)$. Thus, the Generalized Proportional-Integral (GPI) control approach is used for the synthesis of a robust output feedback control scheme. This control technique
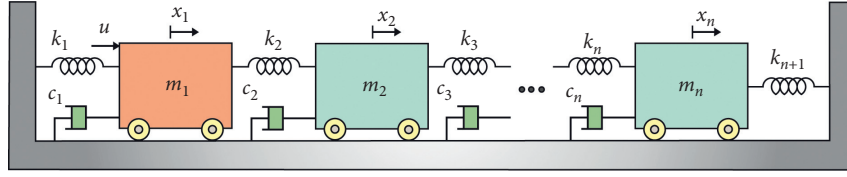
FIGURE 1: Schematic diagram of a n DOF flexible mechanical system.

is based on the integral reconstruction of the state variables through iterated integrations of the output and input variables [17]. Moreover, dynamic tracking error compensation is used to reject disturbances using only measurements of the output position variable y.

For control design purposes, it is assumed that the disturbance signal $\xi(t)$ can be approximated into a small window of time by the r-th order Taylor polynomial expansion, around a given time instant $t_0 > 0$,

$$\xi(t) \approx \sum_{i=0}^{r} p_i (t - t_0)^i, \tag{4}$$

where coefficients p_i are completely unknown. In addition, we have assumed that $\xi(t)$ is uniformly absolutely bounded, i.e.,

$$\|\xi\|_\infty = \sup_{t \in [0,\infty)} |\xi(t)| = \delta < \infty, \tag{5}$$

where δ is a possibly unknown positive constant.

Dynamics of the output position variable of the mechanical system is then described into an infinitesimal time window as

$$\ddot{y} = \frac{1}{m_1} u + \sum_{i=0}^{r} p_i (t - t_0)^i. \tag{6}$$

By integrating equation (6), one can obtain the following integral reconstructor for the velocity signal:

$$\widehat{\dot{y}} = \frac{1}{m_1} \int_{t_0}^{t} u(\tau) d\tau. \tag{7}$$

Note that initial conditions of the uncertain mechanical system and coefficients p_i were intentionally neglected in the integral reconstruction of the velocity signal. Thus, the structural estimate $\widehat{\dot{y}}$ differs from the actual velocity signal by an algebraic polynomial up to $r + 1$-th degree as follows:

$$\widehat{\dot{y}} = \dot{y} + \sum_{i=0}^{r+1} \lambda_i (t - t_0)^i, \tag{8}$$

where constants λ_i depend on unknown initial conditions and coefficients of the disturbance model (4).

Then, a dynamic controller, using integral velocity reconstruction (7), for both active disturbance suppression and robust reference trajectory tracking is proposed as follows:

$$u = m_1 \left[\ddot{y}^* - \beta_{r+3} \left(\widehat{\dot{y}} - \dot{y}^* \right) - \beta_{r+2} (y - y^*) - \chi_{r+1} \right], \tag{9}$$

with

$$\dot{\chi}_0 = \beta_0 (y - y^*),$$
$$\dot{\chi}_1 = \chi_0 + \beta_1 (y - y^*),$$
$$\vdots \tag{10}$$
$$\dot{\chi}_r = \chi_{r-1} + \beta_r (y - y^*),$$
$$\dot{\chi}_{r+1} = \chi_r + \beta_{r+1} (y - y^*).$$

Substitution of controller (9) into equation (6) leads to the closed-loop tracking error dynamics, $e = y - y^*$:

$$e^{(r+4)} + \sum_{k=0}^{r+3} \beta_k e^{(k)} = 0. \tag{11}$$

Hence, by selecting the design parameters β_k, the characteristic polynomial associated with the tracking error dynamics (11) is a Hurwitz polynomial results in a globally exponentially asymptotically stable equilibrium point. Therefore,

$$\lim_{t \to \infty} e = 0 \implies \lim_{t \to \infty} y = y(t)^*. \tag{12}$$

2.1. Experimental Results. Analytical results were confirmed by real-time experiments performed on a three degree-of-freedom mass-spring-damper system characterized by the set of system parameters described in Table 1. The experimental setup used to test the proposed control approach is a rectilinear mechanical plant (Model 210a) provided by Educational Control Products. The design parameters for the output feedback tracking controller were selected to have the closed-loop characteristic polynomial:

$$P_c(s) = \left(s^2 + 2\zeta\omega_n s + \omega_n^2 \right)^4, \tag{13}$$

with $r = 4$, $\omega_n = 70$ rad/s, and $\zeta = 7$.

Figure 2 confirms the acceptable performance of the tracking control scheme. In this case study, the vibration test system was also perturbed by unmodeled dynamics associated with flexible beam structures connected to each mass, as shown in Figure 3. The satisfactory tracking of the reference position trajectory y^* is verified. This profile was planned to smoothly transfer the mass m_1 from the rest position to the equilibrium position of 0.01 m in a time interval of 3 s. Therefore, in Section 3, the proposed control approach is extended to the desired motion tracking problem on perturbed quadrotor helicopters.

3. Dynamic Model of a Quadrotor Helicopter

The quadrotor is a controlled aerial mechanical system with six degrees of freedom and only four control inputs. Moreover, its dynamic behaviour is governed by a set of strongly coupled

TABLE 1: Parameters of a 3 DOF mass-spring-damper system.

|		
$m_1 = 2.82$ kg	$c_1 = 3.64$ Ns/m	$k_1 = 191.315$ N/m
$m_2 = 2.59$ kg	$c_2 = 1.75$ Ns/m	$k_2 = 391.16$ N/m
$m_3 = 2.59$ kg	$c_3 = 1.75$ Ns/m	$k_3 = 344.83$ N/m

(a)

(b)
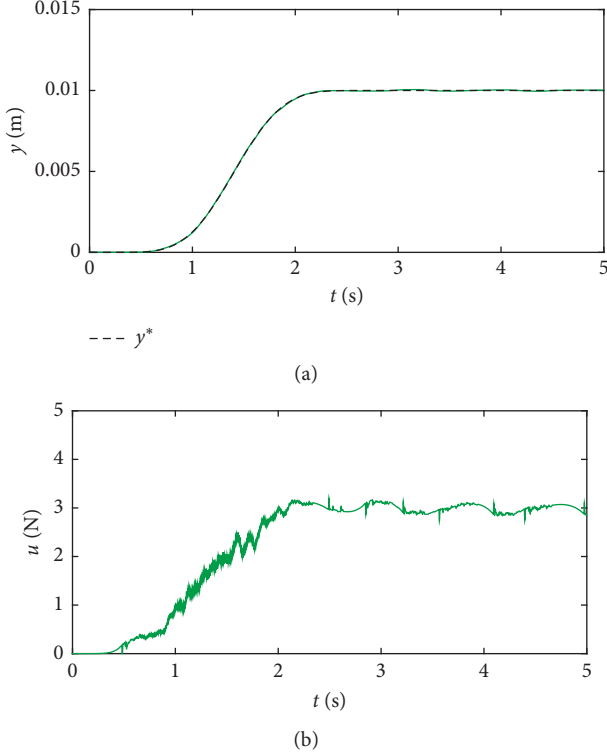
FIGURE 2: Experimental results for trajectory tracking planned for the controlled mass.
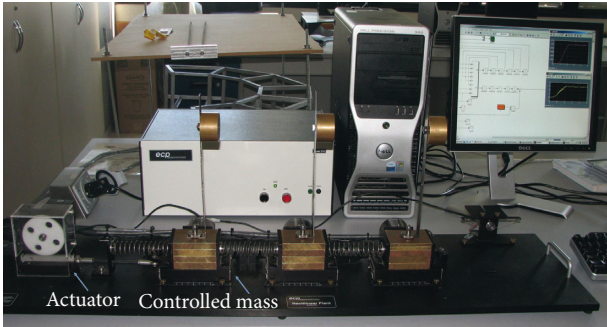
FIGURE 3: Configuration of the experimental setup used to test the performance of the proposed control approach.

nonlinear differential equations. A quadrotor is commonly designed to have a rigid body mechanical structure in order to obtain a simplified mathematical model, where two reference frames are used to describe its dynamic behaviour [3, 25]. The former, a global inertial coordinate system with X, Y, and Z axes, is attached to the Earth, and the second one with X', Y', and Z' axes fixed the quadrotor centre of mass as portrayed in Figure 4. Control force and torques, represented as u, τ_ψ, τ_θ, and τ_ϕ, are generated by four rotors located symmetrically in a

suitably balanced mechanical structure. Thus, force and torque controllers should be synthesized to perform online and offline trajectory tracking for translation and rotation motion in the three-dimensional space.

Controlled system motion is achieved by increasing or decreasing properly the speed of each rotor. The pair of rotors 1 and 3 spin counterclockwise and the other in clockwise. Thus, pitching moment is produced by rotors 1 and 3, as shown in Figure 4(a). Similarly, rolling moment shown in Figure 4(b) is caused by the difference between forces produced by rotors 2 and 4. Yawing moment is originated when angular velocities of lateral rotors are modified, as displayed in Figure 4(c). On the contrary, the control force u, which allows lifting the quadrotor body, stands for the sum of all the vertical forces produced by each rotor.

Relation between produced forces by each rotor and control inputs is given by [3]

$$u = \sum_{i=1}^{4} F_i,$$

$$\tau_\psi = \sum_{i=1}^{4} \tau_{M_i}, \tau_\theta = (F_3 - F_1)l, \tag{14}$$

$$\tau_\phi = (F_2 - F_4)l,$$

where l is the distance from the motors to the centre of mass and τ_{M_i} stands for the torque induced by each electric motor M_i. F_i and τ_{M_i} are related to the geometry of the rotors blades by means of the coefficients of thrust and drag. Hence, motion in different directions on the plane can be attained by regulating angular velocities of rotors in order to change the magnitude of the forces F_i. Therefore, by suitably combining the rolling, pitching, and yawing moments, a quadrotor can track different reference trajectories.

The nonlinear dynamic model of the quadrotor is obtained by the Euler–Lagrange formalism [3, 25]. The vector of generalized coordinates is given by

$$q = [x \ y \ z \ \phi \ \theta \ \psi] \in \mathbb{R}^6, \tag{15}$$

where ϕ, θ, and ψ are the Euler angles describing the orientation of the system and x, y, and z are the position coordinates of the centre of mass measured with respect to the inertial reference frame. By considering the kinetic and potential energies, the Lagrangian is then given by

$$L = \frac{1}{2} \dot{\lambda} \mathbf{M} \dot{\lambda}^\top + \frac{1}{2} \dot{\eta}^\top \mathfrak{I} \dot{\eta} - \lambda \mathbf{M} \mathbf{g}, \tag{16}$$

where $\mathbf{M}$ is the diagonal mass matrix, $\mathfrak{I}$ is the equivalent inertia tensor, $\mathbf{g} = [0 \ 0 \ g]^\top$ is the gravity vector, g is the acceleration constant of gravity, $\lambda = [x \ y \ z]$ stands for the position vector, and $\eta = [\phi \ \theta \ \psi]$ is the orientation vector, both expressed in the global reference frame. The nonlinear translational dynamics of the quadrotor is given by

$$m\ddot{x} = -u \sin \theta + \xi_x,$$
$$m\ddot{y} = u \cos \theta \sin \phi + \xi_y, \tag{17}$$
$$m\ddot{z} = u \cos \theta \cos \phi - mg + \xi_z,$$
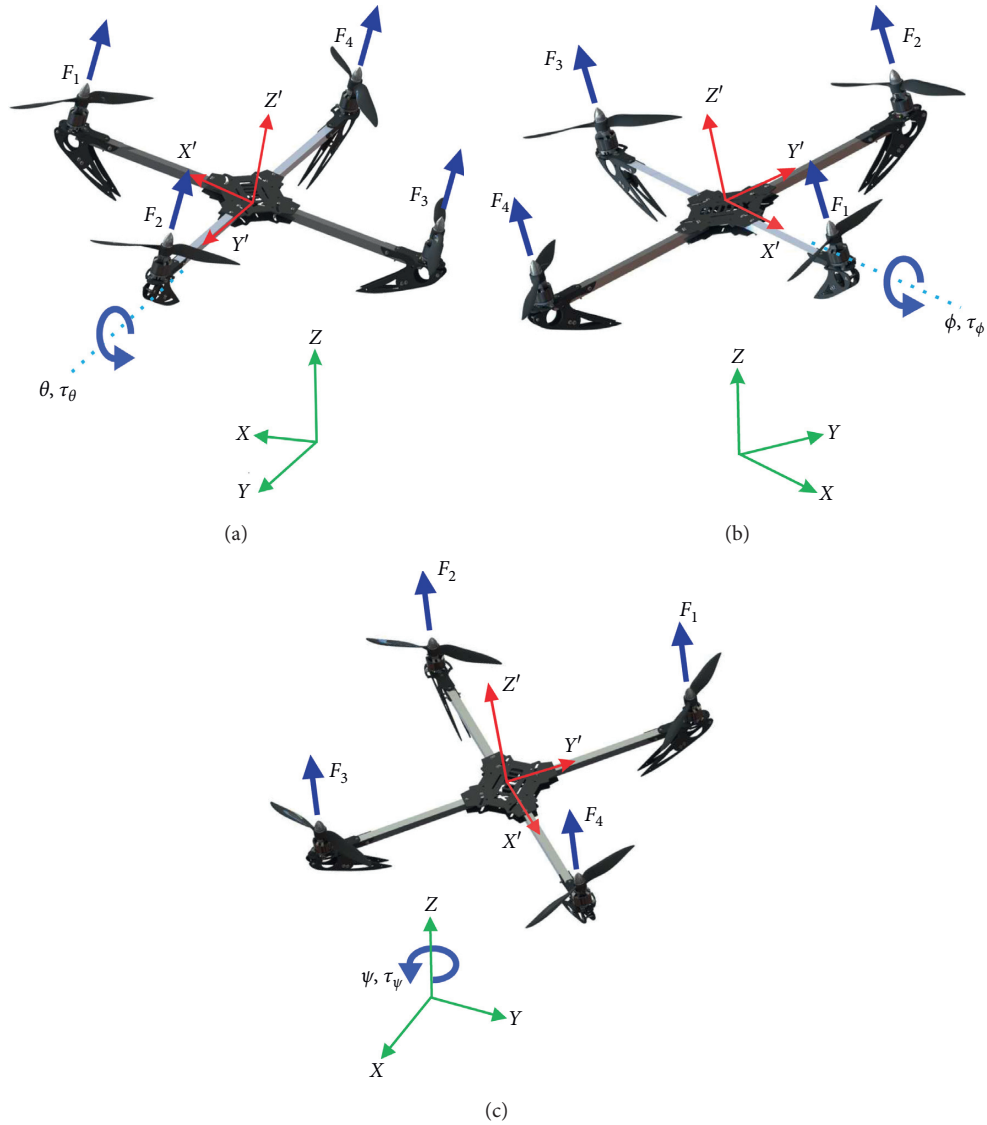
FIGURE 4: Motion in each direction of the space by the control inputs. (a) Pitching moment. (b) Rolling moment. (c) Yawing moment.

where ξ_x, ξ_y, and ξ_z denote unknown time-varying force disturbances affecting the operation of the aerial system. Simultaneously, rotational dynamics has numerous nonlinear couplings between system variables and parameters. Disturbed angular dynamics is described in a compact form as follows:

$$\mathfrak{I}\ddot{\boldsymbol{\eta}} = \boldsymbol{\tau}_{\boldsymbol{\eta}} - \mathbf{C}(\dot{\boldsymbol{\eta}}, t\eta\,)\dot{\boldsymbol{\eta}} + \boldsymbol{\xi}_{\boldsymbol{\eta}}, \tag{18}$$

where

$$\mathfrak{I} = \begin{bmatrix} -I_x s_\theta & 0 & I_x \\ \left(I_y - I_z\right)c_\theta c_\phi s_\phi & I_y c_\phi^2 + I_z s_\phi^2 & 0 \\ I_z c_\theta^2 c_\phi^2 + I_y c_\theta^2 s_\phi^2 + I_x s_\theta^2 & \left(I_y - I_z\right)c_\theta c_\phi s_\phi & -I_x s_\theta \end{bmatrix},$$

$$\mathbf{C}(\dot{\boldsymbol{\eta}}, \boldsymbol{\eta}) = \begin{bmatrix} c_{11} & c_{12} & c_{13} \\ c_{21} & c_{22} & c_{23} \\ c_{31} & c_{32} & c_{33} \end{bmatrix}, \tag{19}$$

with

$$c_{11} = \left(I_z - I_y\right)\dot{\psi}s_\phi c_\phi c_\theta^2,$$

$$c_{12} = -I_x\dot{\psi}c_\theta + I_y\left(\dot{\theta}s_\phi c_\phi + \dot{\psi}c_\theta s_\phi^2 - \dot{\psi}c_\theta c_\phi^2\right) - I_z\left(\dot{\psi}c_\theta s_\phi^2 - \dot{\psi}c_\theta c_\phi^2 + \dot{\theta}s_\phi c_\phi\right),$$

$$c_{13} = 0,$$

$$c_{21} = -I_x\dot{\psi}s_\theta c_\theta + I_y\dot{\psi}s_\theta c_\theta s_\phi^2 + I_z\dot{\psi}s_\theta c_\theta c_\phi^2,$$

$$c_{22} = \left(I_z - I_y\right)\dot{\phi}s_\phi c_\phi,$$

$$c_{23} = I_x\dot{\psi}c_\theta + I_y\left(-\dot{\theta}s_\phi c_\phi + \dot{\psi}c_\theta c_\phi^2 - \dot{\psi}c_\theta s_\phi^2\right) + I_z\left(\dot{\psi}c_\theta s_\phi^2 - \dot{\psi}c_\theta c_\phi^2 + \dot{\theta}s_\phi c_\phi\right),$$ (20)

$$c_{31} = \dot{\theta}I_x s_\theta c_\theta + I_y\left(-\dot{\theta}s_\theta c_\theta s_\phi^2 + \dot{\phi}s_\phi c_\phi c_\theta^2\right) - I_z\left(\dot{\theta}s_\theta c_\theta c_\phi^2 + \dot{\phi}s_\phi c_\phi c_\theta^2\right),$$

$$c_{32} = I_x\dot{\psi}s_\theta c_\theta - I_y\left(\dot{\theta}s_\theta s_\phi c_\phi + \dot{\phi}c_\theta s_\phi^2 - \dot{\phi}c_\theta c_\phi^2 + \dot{\psi}s_\theta c_\theta s_\phi^2\right) + I_z\left(\dot{\phi}c_\theta s_\phi^2 - \dot{\phi}c_\theta c_\phi^2 - \dot{\psi}s_\theta c_\theta c_\phi^2 + \dot{\theta}s_\theta s_\phi c_\phi\right),$$

$$c_{33} = -I_x\dot{\theta}c_\theta + \left(I_y - I_z\right)\left(\dot{\psi}c_\theta^2 s_\phi c_\phi\right).$$

Here, for purposes of simplicity of the model representation, s_i and c_i stand for the sine and cosine functions for $i = \theta, \phi$. The control torque vector is denoted by $\tau_\eta = \begin{bmatrix} \tau_\phi & \tau_\theta & \tau_\psi \end{bmatrix}^\top$. Similarly, $\xi_\eta = \begin{bmatrix} \xi_\phi & \xi_\theta & \xi_\psi \end{bmatrix}^\top$ represents a torque disturbance vector due to wind corrupting the rotational dynamics. Parametric uncertainty and unmodeled dynamics could be also lumped in disturbances ξ_γ, for $\gamma = x, y, z, \phi, \theta, \psi$.

4. Robust Motion Tracking Control for Quadrotor Helicopters

ADRC focuses on the input and output evolution instead of the use of some detailed nonlinear mathematical model of the disturbed dynamic system [11, 12]. An extended state observer is designed to estimate disturbances. After, real-time estimated disturbances are included in the control syntheses to guarantee active disturbance rejection. In the present contribution, from a different control design perspective, disturbance observers and time derivatives of output signals are unnecessary. Time-varying disturbances are actively and directly suppressed by dynamic error compensation properly embedded into control signals.

The proposed main control scheme is schematically depicted in Figure 5. Two virtual controllers are synthesized for adjusting the nonactuated dynamics and ensure the efficient and robust tracking of position reference trajectories in X and Y directions. Meanwhile, fully actuated dynamics are regulated directly by suitable action of four robust controllers. The control scheme is based on tracking errors given by the difference between real measured variables and desired reference trajectories, with $\gamma = x, y, z, \phi, \theta, \psi$,

$$e_\gamma = \gamma - \gamma^*,$$ (21)

where the superscript $*$ is used to denote reference trajectory for some system variable. Here, a virtual control block computes the reference trajectories θ^* and ϕ^*, according to the desired motion for X and Y directions as follows:

$$\theta^* = \sin^{-1}\left(-\frac{1}{u}mv_x\right),$$

$$\phi^* = \sin^{-1}\left(\frac{1}{u\cos\theta}mv_y\right).$$ (22)

For robust control design purposes, from equations (17) and (18), disturbed tracking error dynamics is simplified as

$$\ddot{e}_\gamma = v_\gamma + \xi_\gamma(t).$$ (23)

Similarly, $\xi_\gamma(t)$ are considered as bounded time-varying disturbance signals and locally approximated into a small interval of time by the r-th order Taylor polynomial expansions:

$$\xi_\gamma(t) \approx \sum_{i=0}^{r} p_{i,\gamma}\left(t - t_0\right)^i,$$ (24)

where coefficients $p_{i,\gamma}$ are assumed to be completely unknown.

From equation (23), integral reconstructors for velocity signals of tracking errors can be then computed by

$$\widehat{\dot{e}}_\gamma = \int_{t_0}^{t} v_\gamma dt.$$ (25)

The polynomial relationship between structural estimates $\widehat{\dot{e}}_\gamma$ and actual velocity tracking error signals is given by

$$\widehat{\dot{e}}_\gamma = \dot{e}_\gamma + \sum_{i=0}^{r+1} \lambda_{i,\gamma}\left(t - t_0\right)^i,$$ (26)

where parameters $\lambda_{i,\gamma}$ are also assumed to be unknown.
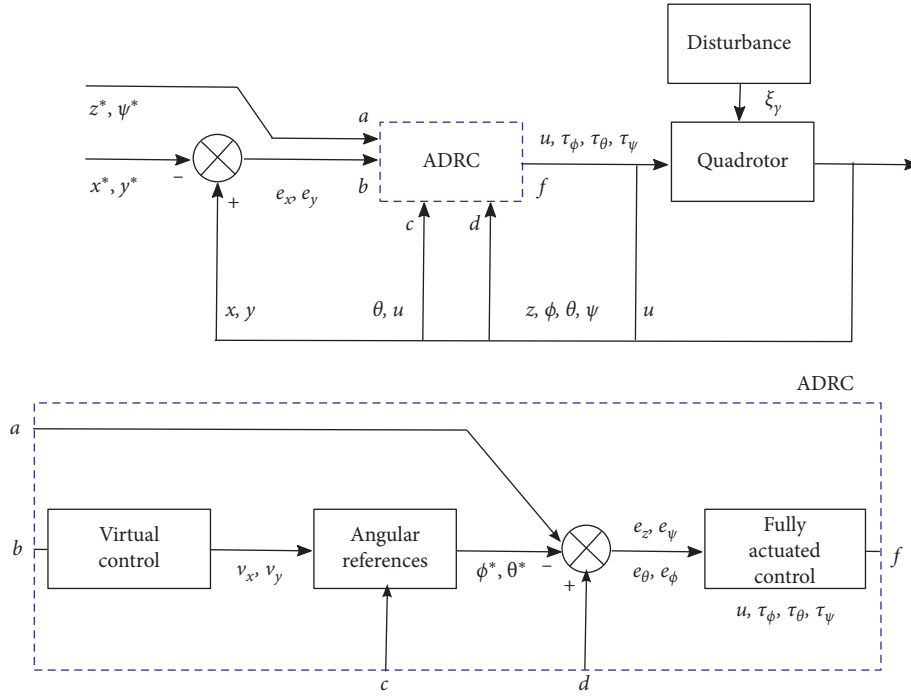
FIGURE 5: Main robust motion control scheme for a disturbed aerial quadrotor vehicle.

Auxiliary controllers for desired motion trajectory tracking tasks on the aerial vehicle are then proposed as

$$v_\gamma = -\beta_{r+3,\gamma}\widehat{\dot{e}}_\gamma - \beta_{r+2,\gamma}e_\gamma - \chi_{r+1,\gamma}, \quad (27)$$

with

$$\begin{aligned}
\dot{\chi}_{0,\gamma} &= \beta_{0,\gamma}e_\gamma, \\
\dot{\chi}_{1,\gamma} &= \chi_{0,\gamma} + \beta_{1,\gamma}e_\gamma, \\
&\vdots \\
\dot{\chi}_{r,\gamma} &= \chi_{r-1,\gamma} + \beta_{r,\gamma}e_\gamma, \\
\dot{\chi}_{r+1,\gamma} &= \chi_{r,\gamma} + \beta_{r+1,\gamma}e_\gamma.
\end{aligned} \quad (28)$$

Then, from equations (23) and (27), closed-loop tracking error dynamics is governed by

$$e_\gamma^{(r+4)} + \sum_{k=0}^{r+3} \beta_{k,\gamma}e_\gamma^{(k)} = 0. \quad (29)$$

Therefore, control gains $\beta_{k,\gamma}$ should be selected so that characteristic polynomials associated with the closed-loop error dynamics (29),

$$P_{\mathrm{CL},\gamma}(s) = s^{r+4} + \sum_{k=0}^{r+3} \beta_{k,\gamma}s^k, \quad (30)$$

are Hurwitz polynomials and faster than disturbance signals. In this way, reference trajectory tracking can be achieved:

$$\lim_{t \to \infty} e_\gamma = 0 \implies \lim_{t \to \infty} \gamma = \gamma^*, \quad (31)$$

with $\gamma = x, y, z, \phi, \theta, \psi$.

Notice from (18) that

$$\ddot{\boldsymbol{\eta}} = \mathfrak{I}^{-1}\left[\boldsymbol{\tau_\eta} - \mathbf{C}(\dot{\boldsymbol{\eta}}, \boldsymbol{\eta})\dot{\boldsymbol{\eta}}\right] + \mathfrak{I}^{-1}\boldsymbol{\xi_\eta}. \quad (32)$$

The control torque vector can be then proposed as follows:

$$\boldsymbol{\tau_\eta} = \mathfrak{I}\mathbf{v_\eta} + \mathbf{C}(\dot{\boldsymbol{\eta}}, \boldsymbol{\eta})\dot{\boldsymbol{\eta}} + \mathfrak{I}\ddot{\boldsymbol{\eta}}^*, \quad (33)$$

with $\mathbf{v}_\eta = [v_\phi v_\theta v_\psi]^\mathsf{T}$. Thus, substitution of (33) into (18) yields

$$\begin{aligned}
\ddot{\boldsymbol{\eta}} &= \ddot{\boldsymbol{\eta}}^* + \mathbf{v_\eta} + \mathfrak{I}^{-1}\boldsymbol{\xi_\eta}, \\
\ddot{\mathbf{e}}_\eta &= \mathbf{v_\eta} + \mathfrak{I}^{-1}\boldsymbol{\xi_\eta},
\end{aligned} \quad (34)$$

and by expressing the angular acceleration disturbance vector as $\mathfrak{I}^{-1}\boldsymbol{\xi_\eta} = \mathbf{d_\eta}$, it results

$$\ddot{\mathbf{e}}_\eta = \mathbf{v_\eta} + \mathbf{d_\eta}, \quad (35)$$

which presents the structure in (23). Therefore, the control inputs for desired motion trajectory tracking and active disturbance suppression are proposed as

$$\begin{aligned}
u &= \frac{1}{\cos\phi\cos\theta}(mv_z + mg), \\
\tau_\phi &= k_\phi v_\phi, \\
\tau_\theta &= k_\theta v_\theta, \\
\tau_\psi &= k_\psi v_\psi,
\end{aligned} \quad (36)$$

with

$$k_\phi = I_x,$$

$$k_\theta = I_y \cos^2 \phi + I_z \sin^2 \phi, \tag{37}$$

$$k_\psi = I_z \cos^2 \theta \cos^2 \phi + I_y \cos^2 \theta \sin^2 \phi + I_x \sin^2 \theta.$$

TABLE 2: Parameters of the quadrotor system.

Parameter	Value	Units
m	1.016	kg
l	0.225	m
I_x	0.012450	kg·m^2
I_y	0.013303	Kg·m^2
I_z	0.024752	kg·m^2

5. Case Studies on Dynamic Performance Assessment

In this section, numerical experiments to confirm the effectiveness of the proposed dynamic tracking control scheme are described. Experiments were implemented on a lightly damped quadrotor with parameters described in Table 2. Translational reference trajectories in meters are given by

$$x^*(t) = 2\sin\left(\frac{t}{2}\right)\cos\left(\frac{t}{4}\right),$$

$$y^*(t) = 2\sin\left(\frac{t}{2}\right)\sin\left(\frac{t}{4}\right), \tag{38}$$

$$z^*(t) = \frac{t}{4}.$$

Control design parameters were selected for matching closed-loop Hurwitz (stable) polynomials:

$$P_{\text{CL},\gamma}(s) = \left(s^2 + 2\zeta_\gamma \omega_{n,\gamma} s + \omega_{n,\gamma}^2\right)^2 \left(s + p_{c,\gamma}\right), \tag{39}$$

with $\omega_{n,\gamma}$, ζ_γ, $p_{c,\gamma} > 0$ and $\gamma = x, y, z, \phi, \theta, \psi$. Controller adjustment parameters to perform a satisfactory robust tracking of planned trajectories were then selected as $\omega_{n,x} = \omega_{n,y} = 3$ rad/s, $\zeta_x = \zeta_y = 1$, and $p_{c,x} = p_{c,y} = 3$ rad/s; $\omega_{n,z} = 3$ rad/s, $\zeta_z = 2$, and $p_{c,z} = 2$ rad/s; $\omega_{n,\phi} = \omega_{n,\theta} = 10$ rad/s, $\zeta_\phi = \zeta_\theta = 3$, and $p_{c,\theta} = 10$ rad/s; and $\omega_{n,\psi} = 10$ rad/s, $\zeta_\psi = 1$, and $p_{c,\psi} = 10$ rad/s. Additionally, for purposes of robustness assessment, control input gains were selected as $k_\phi = I_x$, $k_\theta = I_y$, and $k_\psi = I_z$.

During simulation experiments, the quadrotor was exposed to follow planned trajectories in presence of completely unknown considerable external disturbances. For purposes of control robustness assessment, the wind disturbance models affecting the aerial vehicle dynamics described in [8, 26] were selected. Interested readers in more details about these disturbance models applied on controlled aerial vehicles can refer to the contributions [8, 26] and references therein. Three case studies for robustness and effectiveness assessment were thus developed.

In the first case study, the quadrotor is exposed to disturbances induced by wind gusts, similar as authors in [8]. Here, the effects of wind gusts on the quadrotor translational accelerations are considered:

$$f_{d_i}(t) = \begin{cases} 0, & 0 \leq t \leq 15, \\ 0.8\sin\left[\dfrac{\pi(t-30)}{31}\right] + 0.4\sin\left[\dfrac{\pi(t-30)}{7}\right] & \\ \qquad\qquad\qquad\qquad\qquad\qquad\qquad 15 < t \leq 45, & \\ + 0.08\sin\left[\dfrac{\pi(t-30)}{2}\right] + 0.056\sin\left[\dfrac{\pi(t-30)}{11}\right], & \\ 0, & 45 < t \leq 65, \\ 0.8\sin\left[\dfrac{\pi(t-30)}{31}\right] + 0.4\sin\left[\dfrac{\pi(t-30)}{7}\right] & \\ \qquad\qquad\qquad\qquad\qquad\qquad\qquad 65 < t \leq 85, & \\ +0.08\sin\left[\dfrac{\pi(t-30)}{2}\right] + 0.056\sin\left[\dfrac{\pi(t-30)}{11}\right], & \\ 0, & t > 85. \end{cases} \tag{40}$$

Therefore, the external disturbance forces introduced in (17) are defined such that

$$\xi_i = m f_{d_i}(t), \tag{41}$$

for $i = x, y, z$. Meantime, disturbance torques in (18) are the following:

$$\xi_\eta = \mathfrak{I}[\sin(t) + 0.2\sin(100\pi t)]. \tag{42}$$

On the contrary, in the second study, the quadrotor is subjected to the effects of crosswind disturbances. The crosswind representation is similar to that in [26], where authors introduce a wind speed model which directly perturbs the helicopter translational motion, and is given by

$$\xi_x = -w_1\sin\theta,$$
$$\xi_y = w_1\cos\theta\sin\phi, \tag{43}$$
$$\xi_z = w_1\cos\theta\cos\phi,$$

where w_1 is the representation of the wind disturbance. Here, induced normal forces for each rotor are included. Additionally, the forces are related with the wind speed model as $w_1 = V_w(t)$, and $V_w(t) = V_{wg}(t) + V_{wt}(t)$, with

$$V_{wg}(t) = \begin{cases} 0, & t < T_{sg}, \\ A_g - A_g\cos\left(2\pi\dfrac{t - T_{sg}}{T_{eg} - T_{sg}}\right), & T_{sg} \leq t \leq T_{eg}, \\ 0, & T_{eg} < t, \end{cases} \tag{44}$$

where $V_w(t)$ is the wind speed expression composed by a gust component V_{wg} and a turbulence term V_{wt}, A_g is the amplitude of the wind gust, T_{sg} is its starting time, and T_{eg} is its stopping time. In this paper, values for $A_g = 1$ m/s, $T_{sg} = 30$ s, and $T_{eg} = 65$ s are adopted. Also, for representing the turbulence component V_{wt}, a band-limited white noise has been implemented. Enforced crosswind affecting rotational displacements is given by $\xi_\eta = [w_2 \; w_3 \; w_4]^\top$, with $w_2 = 0.75w_1$, $w_3 = 0.25w_1$, and $w_4 = 0.15w_1$ (cf. [26]).

In Figure 6, the above main disturbance features are depicted. Notice the differences in the representation for each case.

Exhaustive numerical experiments were performed for both case studies. Figure 7 depicts the vertical trajectory tracking in presence of wind gust and crosswinds, respectively. An adequate position tracking is achieved due to the robustness of the proposed controllers for facing unknown external disturbances. Also, it is appreciated that there is only a slight deviation in the tracking of the planned trajectories represented by discontinuous lines.

Notice from Figure 8 the proper tracking of the planned reference trajectories for X and Y directions, as a consequence of a suitable tuning of the virtual controllers. Moreover, as confirmed in Figure 9, the planned X-Y path is followed adequately by the quadrotor even in presence of the disturbances. Additionally, due to the features of the controller design, the error dynamic presents an asymptotically stable behaviour.

The path reference and the path following in X-Y-Z directions are portrayed in Figures 10(a) and 10(b), respectively. For purposes of simplicity in the representation, the results are presented only for case 1. Nevertheless, the proposed control scheme allows to achieve satisfactory results in both cases studies even though disturbances present diverse behaviour, crosswind, and wind gust, respectively.

Figures 11 and 12 show the control inputs responses calculated online to regulate efficiently the quadrotor flight according to planned trajectories and paths, as well as to reject uncertain variable disturbances in spite of not having information about their dynamic behaviour. Additionally, the proposed control scheme allows ensuring a proper tracking even though the information about the derivatives of the interest variables is not available.

Notice that actuators are not saturated by the computed control inputs, since these are acceptably small and smooth, which could represent considerable energy savings during the execution of flight tasks as well. Disturbance effects are also observed in each designed control input signal.

Figure 13 shows the time histories of the quadrotor pitch and roll tracking. The references θ^* and ϕ^* were computed online accordingly to equation (22) in order to regulate the displacements in X and Y directions adequately. In both cases the tracking of the computed references is achieved due to the robust structure of the proposed control scheme, where the virtual control stage depends on the regulation and tracking of this variables for ensuring the planned path following.

Lastly, the desired yaw angle reference ψ^* is given as follows:

$$\psi^* = \begin{cases} \psi_i, & 0 \leq t < T_1, \\ \psi_i + (\psi_f - \psi_i)\mathcal{B}_z(t, T_1, T_2), & T_1 \leq t \leq T_2, \\ \psi_f, & t > T_2, \end{cases} \tag{45}$$

where $\psi_i = 0$ rad, $\psi_f = 0.5$ rad, $T_1 = 0$ s, $T_2 = 5$ s, and $\mathcal{B}_z(t, T_1, T_2)$ is a Bézier interpolation polynomial given by

$$\mathcal{B}_z(t, T_1, T_2) = \frac{t - T_1}{T_2 - T_1}\left[r_1 - r_2\left(\frac{t - T_1}{T_2 - T_1}\right) + r_3\left(\frac{t - T_1}{T_2 - T_1}\right)^2 - \cdots + r_6\left(\frac{t - T_1}{T_2 - T_1}\right)^5\right], \tag{46}$$

with constants $r_1 = 252$, $r_2 = 1050$, $r_3 = 1800$, $r_4 = 1575$, $r_5 = 700$, and $r_6 = 126$.

Therefore, results show the proposed control approach simultaneously can properly reject disturbances and

(a)

(b)
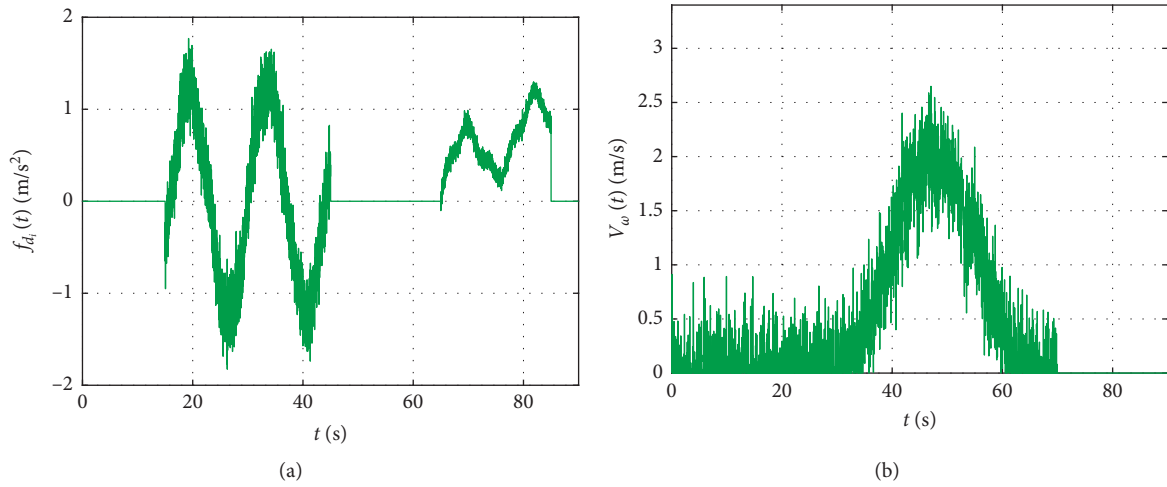
FIGURE 6: Wind disturbance representations. (a) Disturbance for $i = x$; y; z, case 1. (b) Wind speed model, case 2.


(a)

(b)
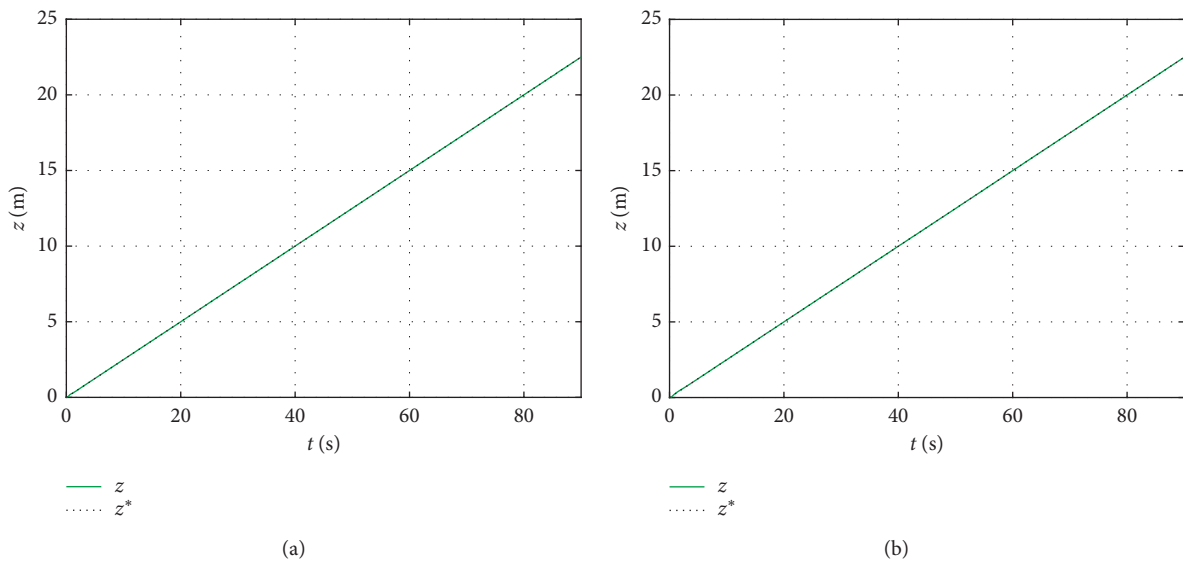
FIGURE 7: Tracking of planned reference trajectories for Z direction. (a) Trajectory tracking in (Z) case 1. (b) Trajectory tracking in (Z) case 2.


(a)

(b)
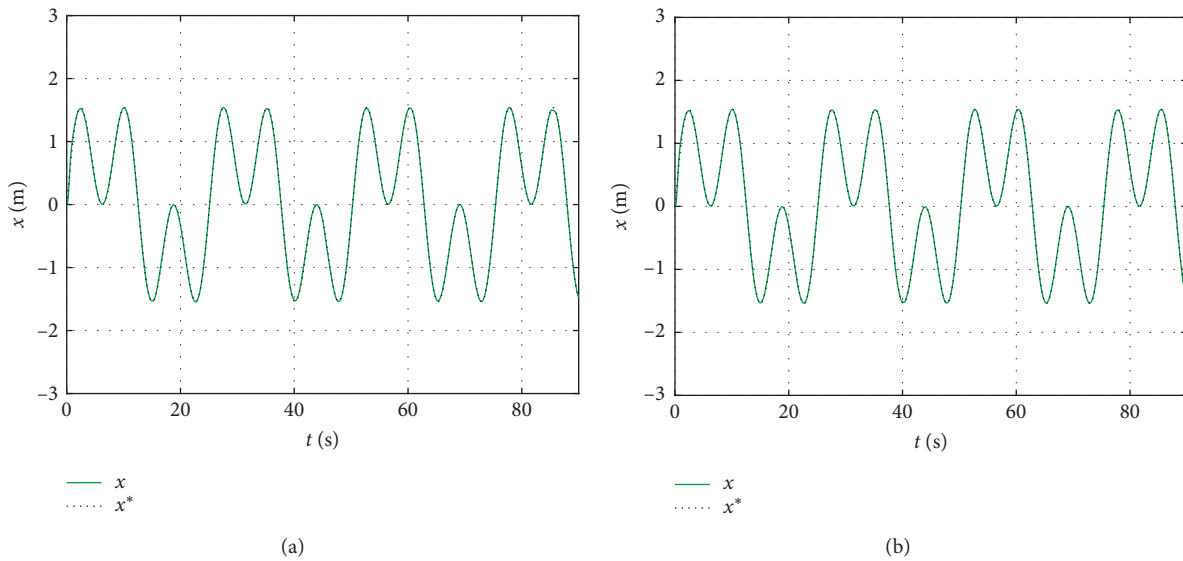
FIGURE 8: Continued.

(c)

(d)
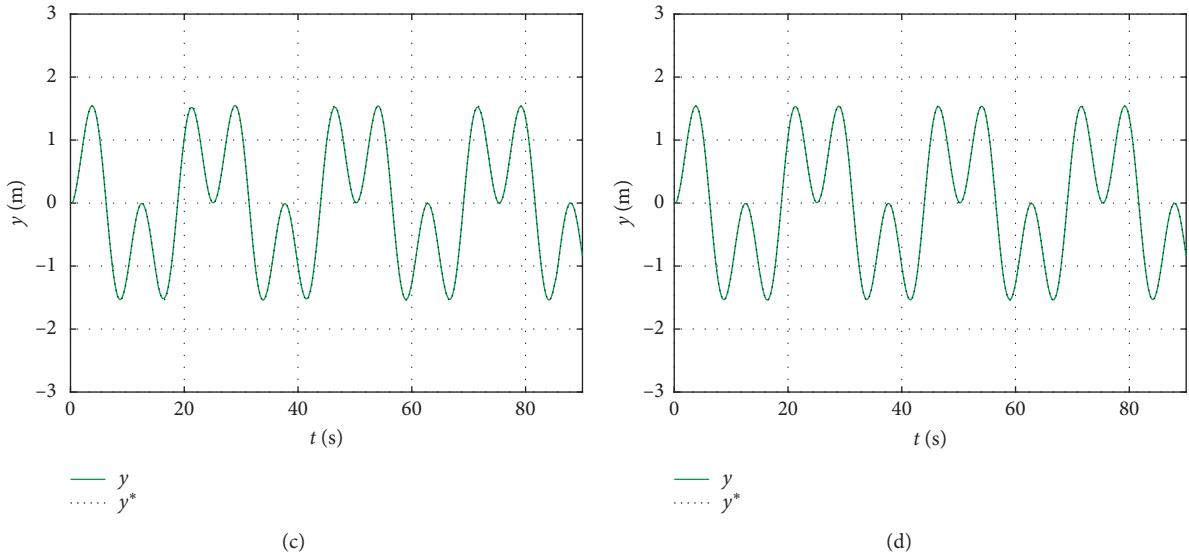
FIGURE 8: Tracking of planned reference trajectories for X and Y directions. (a) Trajectory tracking in X case 1. (b) Trajectory tracking in X case 2. (c) Trajectory tracking in Y, case 1. (d) Trajectory tracking in Y, case 2.

(a)

(b)
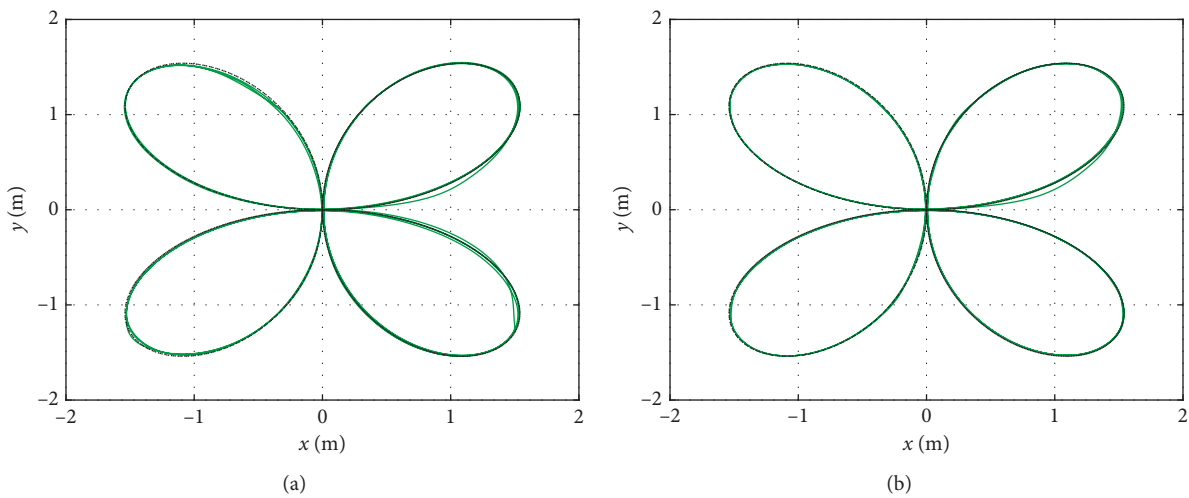
FIGURE 9: X-Y path followed by the quadrotor vehicle. (a) Path following case 1. (b) Path following case 2.

(a)

(b)
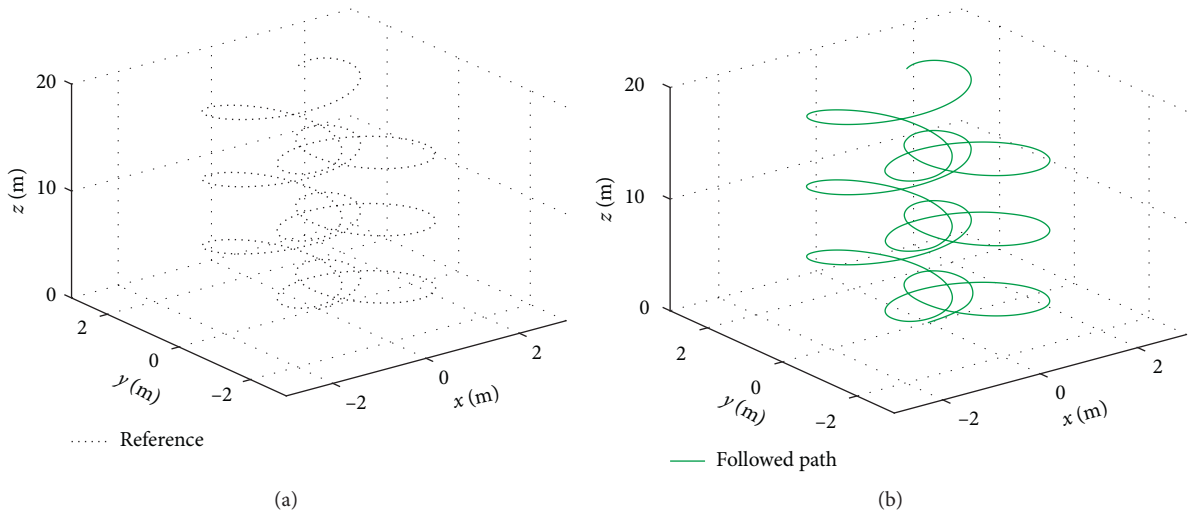
FIGURE 10: Following of the reference path specified for the controlled quadrotor motion, case 1.

(a)

(b)

(c)

(d)
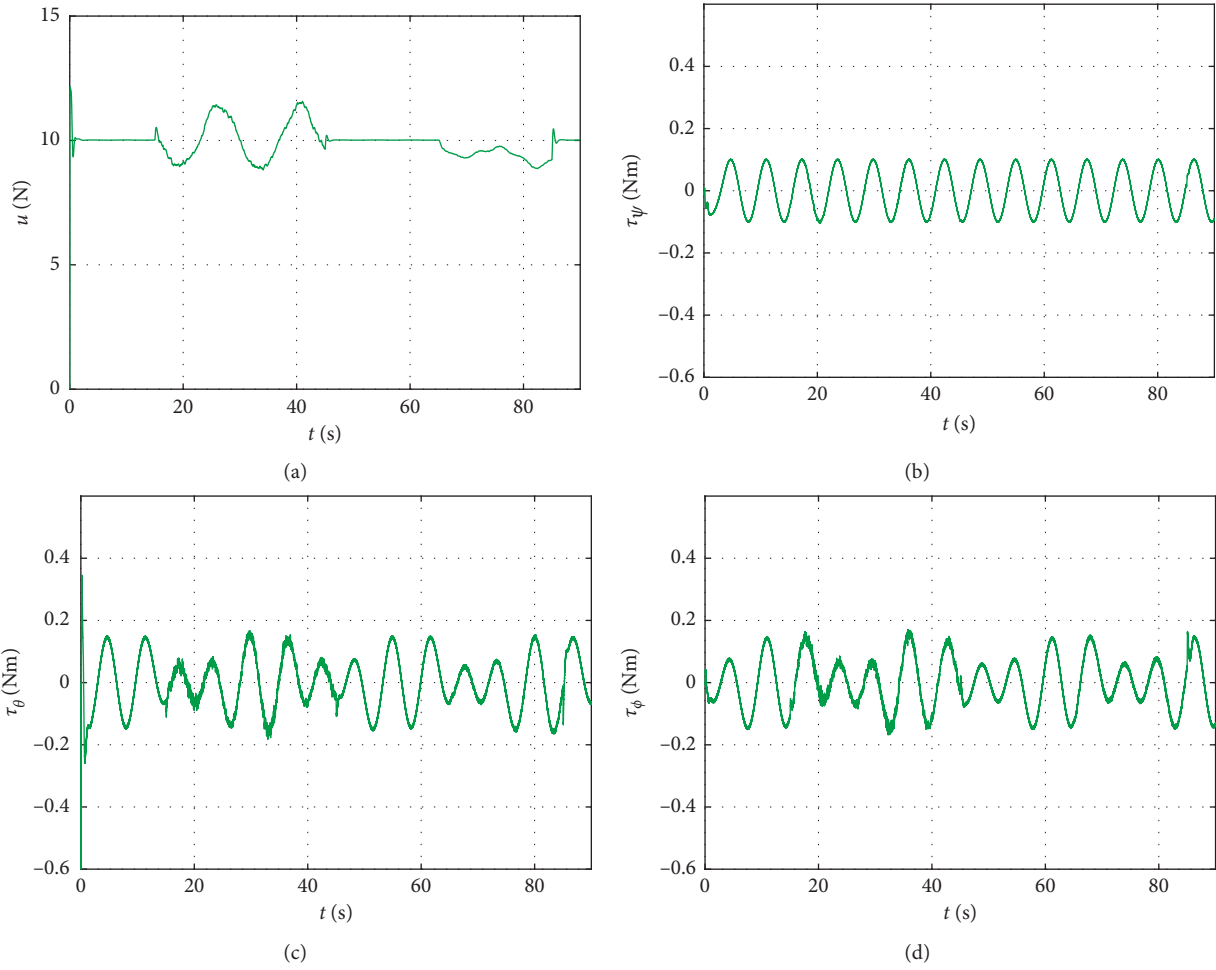
FIGURE 11: Computed robust control input signals for compensation of disturbances, case 1. (a) u. (b) τ_{ψ}. (c) τ_{θ}. (d) τ_{φ}.

(a)

(b)
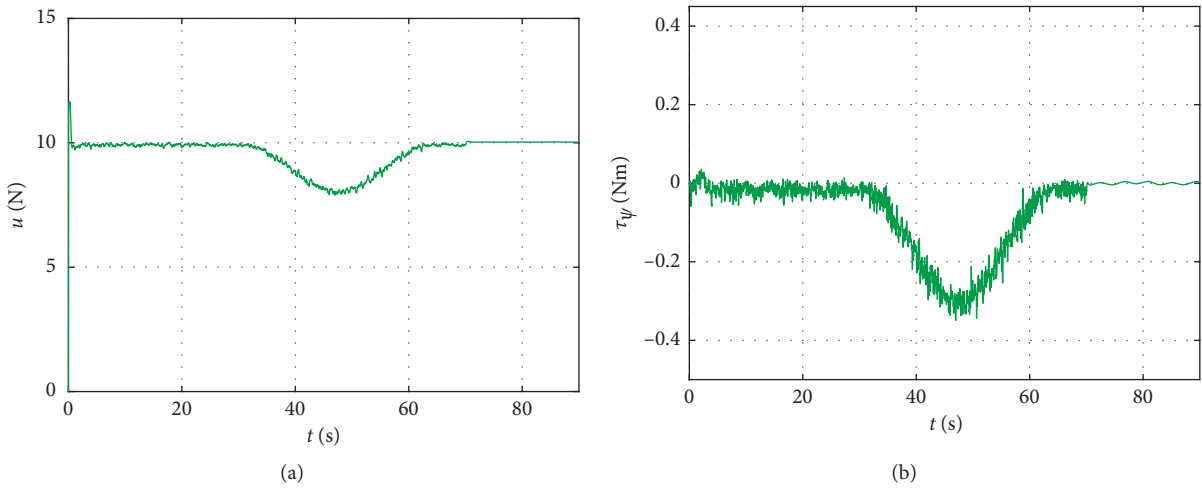
FIGURE 12: Continued.

(c)

(d)
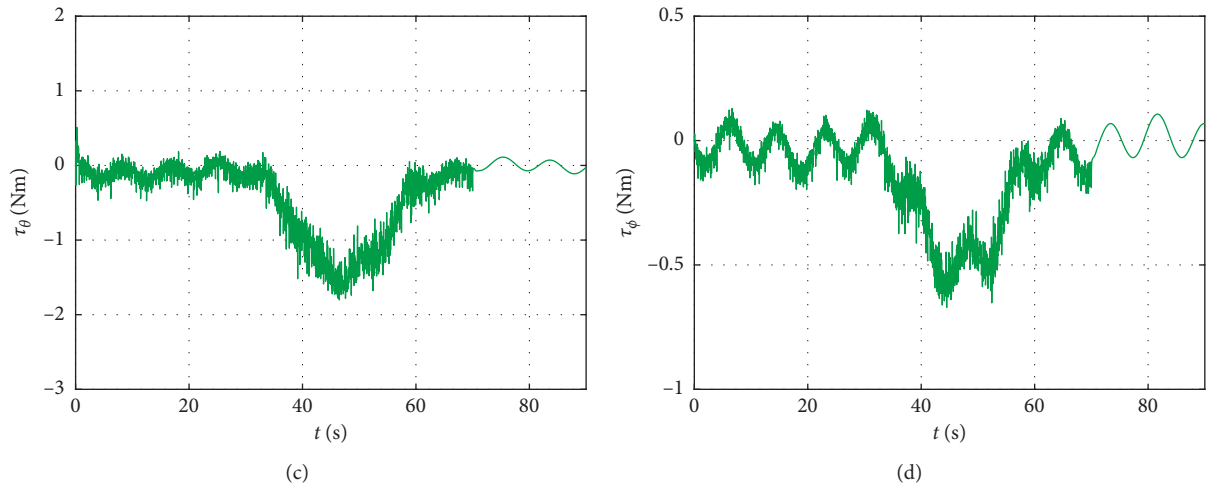
FIGURE 12: Computed robust control input signals for compensation of disturbances, case 2. (a) u. (b) τ_ψ. (c) τ_θ. (d) τ_φ.


(a)

(b)

(c)

(d)
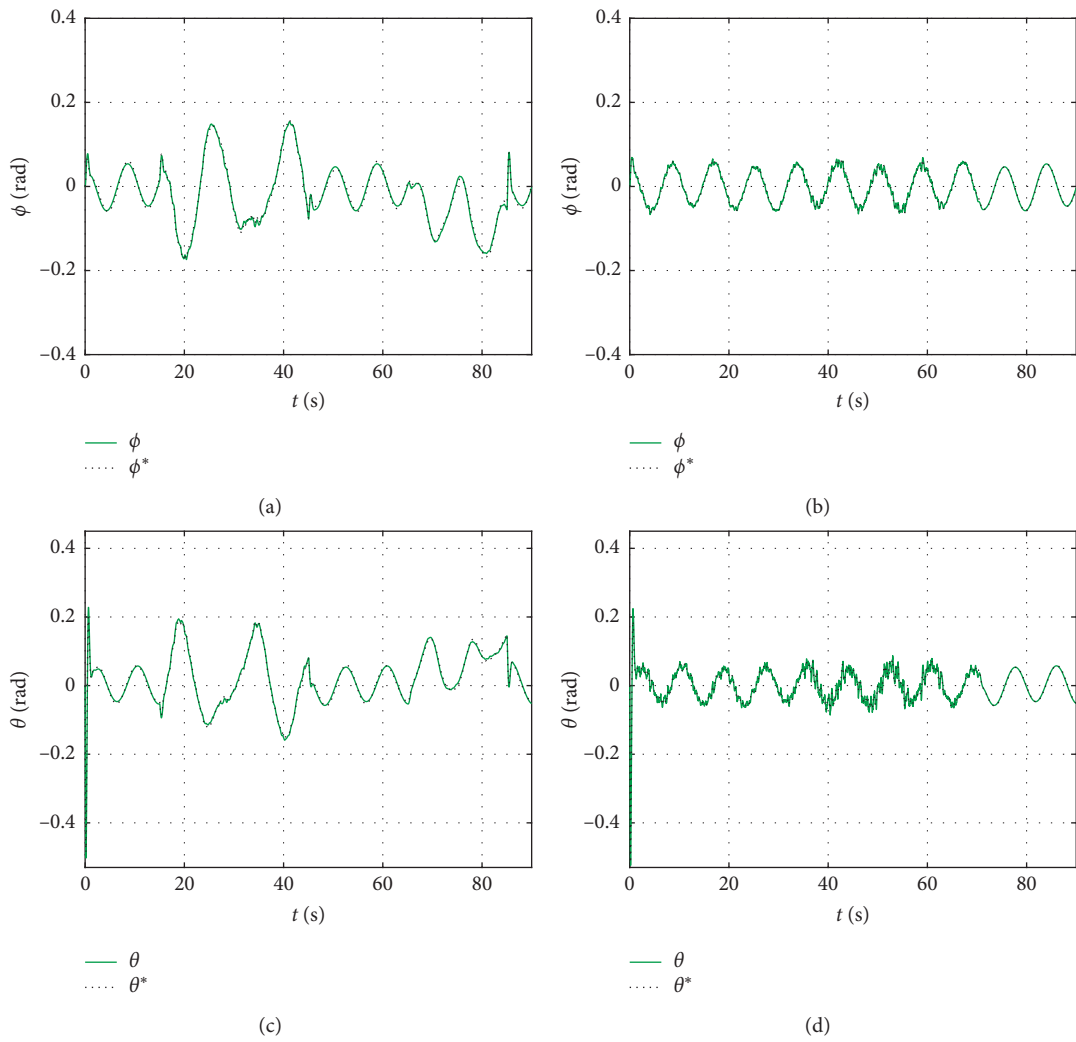
FIGURE 13: Continued.

(e)

(f)
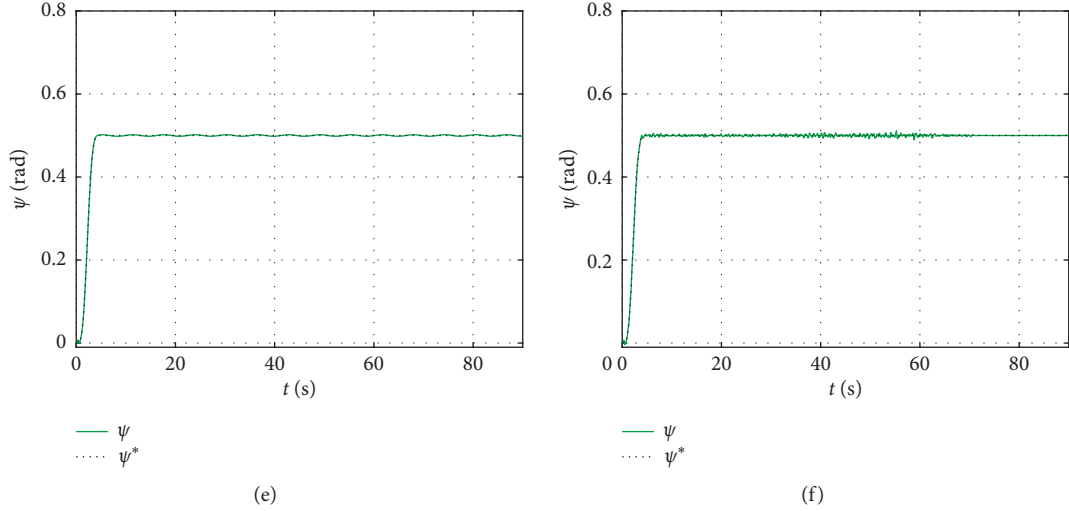
Figure 13: Tracking of planned reference trajectories for angular motion. (a) Trajectory tracking for φ, case 1. (b) Trajectory tracking for φ, case 2. (c) Trajectory tracking for θ, case 1. (d) Trajectory tracking for θ, case 2. (e) Trajectory tracking for ψ, case 1. (f) Trajectory tracking for ψ, case 2.
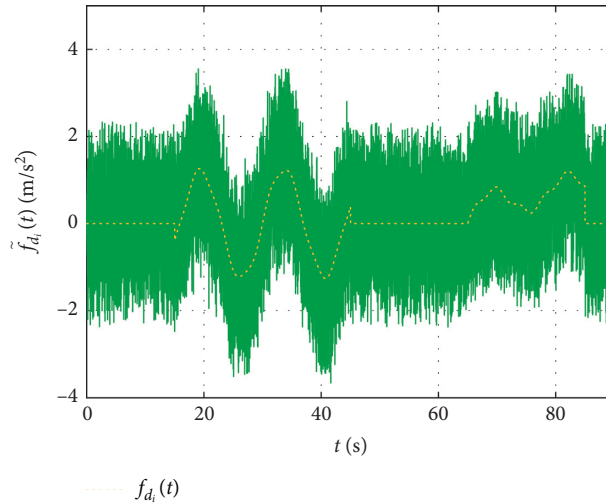

Figure 14: Acceleration disturbances induced by high-frequency motions.

perform an efficient tracking. Besides, notice from (33) that it is unnecessary to include the model information about the matrix Coriolis $\mathbf{C}(\dot{\eta}, \eta)$ as well as the angular nominal control trajectories $\ddot{\eta}^*$ in the controller design (36), which is desirable to keep the structure of the proposed controllers simple as possible.

Finally, a third case study is introduced to show the effectiveness and robustness of the proposed motion tracking control scheme against additional high-frequency time-varying disturbances depicted in Figure 14. Wide spectrum disturbances affecting the controlled aerial vehicle dynamics are described as

$$\xi_i = m\tilde{f}_{d_i}(t), \tag{47}$$

with

$$\tilde{f}_{d_i}(t) = f_{d_i}(t) + \mathcal{U}(0,1) + \mathcal{H}(n,t,\mathcal{A}). \tag{48}$$

Here, white noise generated by an uniform distribution $\mathcal{U}(0,1)$ in the interval $[0,1]$ was added. High-frequency harmonic components were also considered as

$$\mathcal{H}(n,t,\mathcal{A}) = \left[\mathcal{A} \sum_{j=1}^{n} \sin(100\,jt) \right] + \text{sign}(\mathcal{N}(\mu,\sigma)) - 0.5, \tag{49}$$

with $\mathcal{A} = 0.5$ and $n = 3$. Furthermore, high-frequency unpredictable oscillations generated by a normal distribution $\mathcal{N}(\mu,\sigma)$, with mean value $\mu = 0$ and standard deviation $\sigma = 1$, were included.

Figure 15 portrays the robust control performance for following the 3D planned path. A satisfactory reference trajectory tracking can be observed in Figure 16, even though the quadrotor is subjected to high-frequency disturbance motions.

(a)

(b)
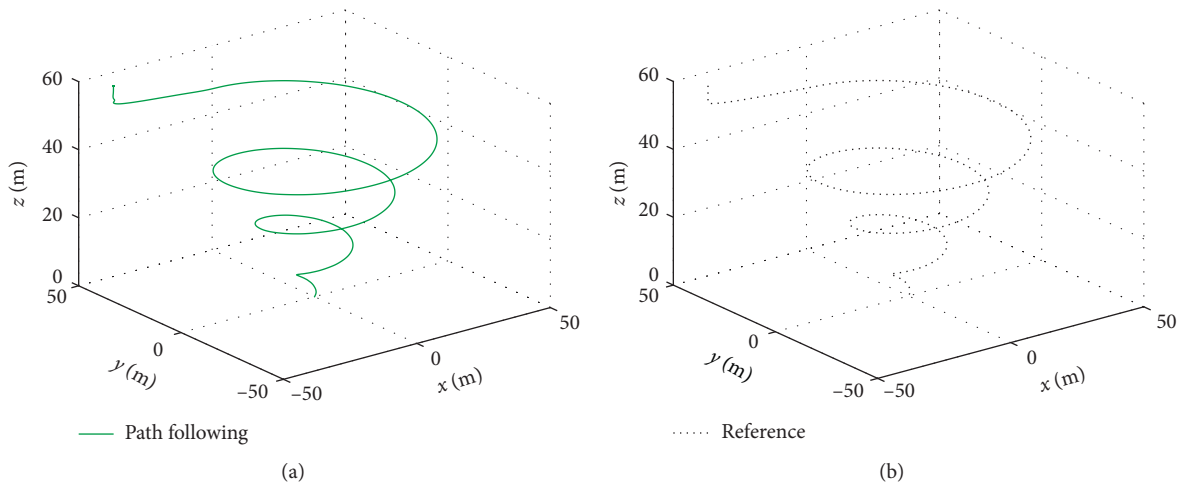
FIGURE 15: Satisfactory tracking of the reference path specified for the controlled quadrotor motion, case 3.


(a)

(b)

(c)

(d)
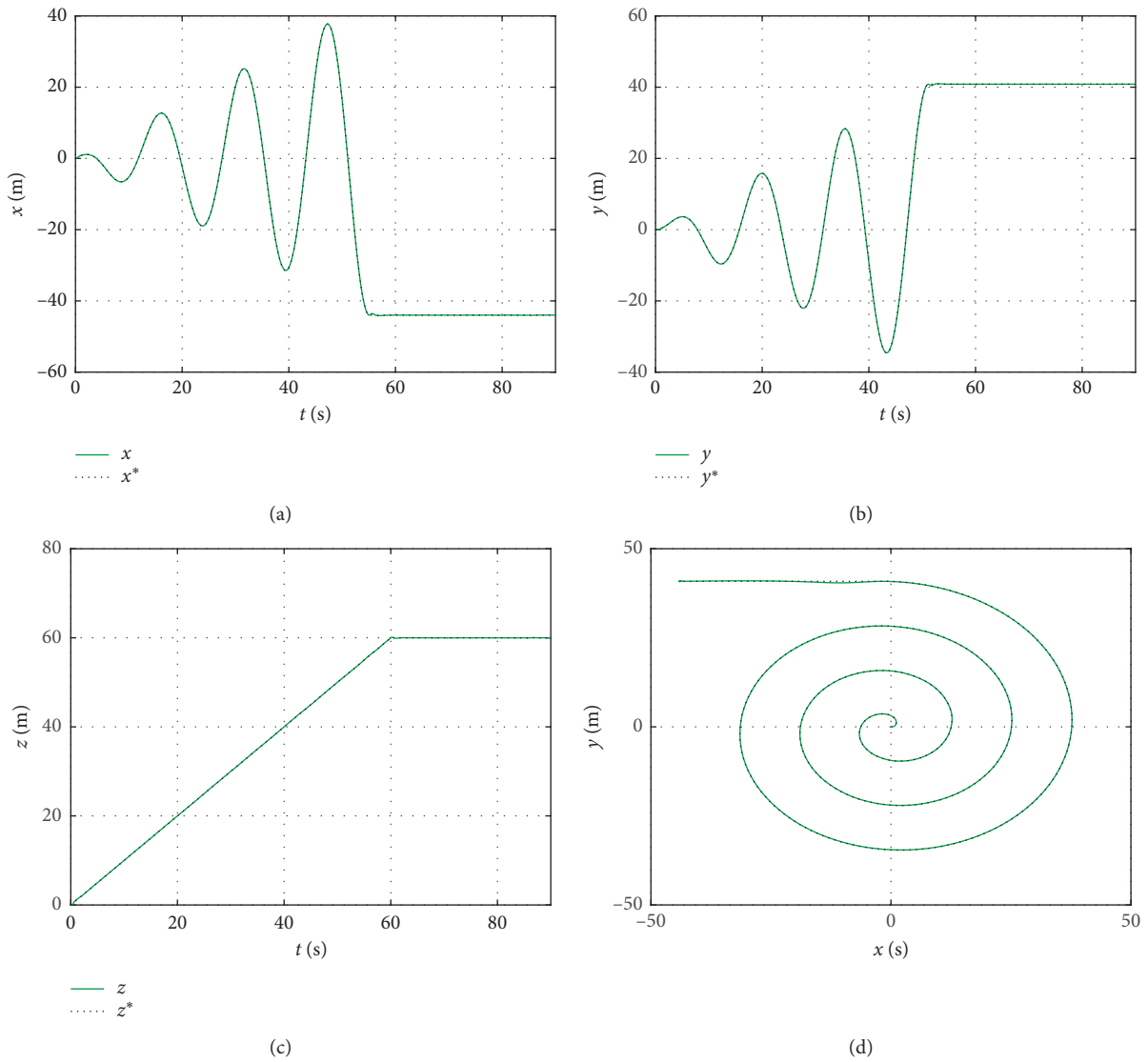
FIGURE 16: Tracking of the planned motion reference trajectories. (a) Trajectory tracking in X, case 3 (b) Trajectory tracking in Y, case 3 (c) Trajectory tracking in Z, case 3 (d) Path following, case 3.

(a)

(b)

(c)

(d)
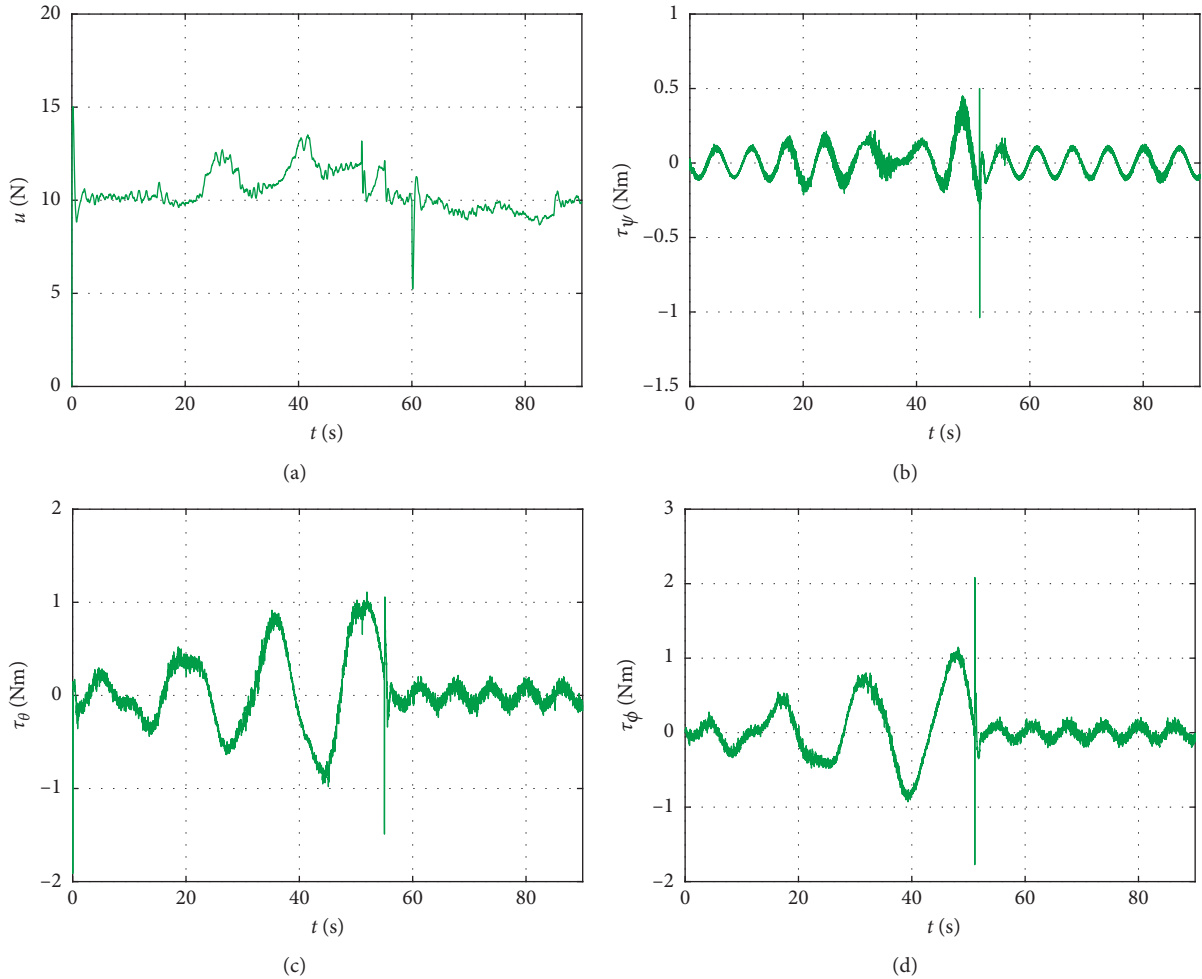
FIGURE 17: Robust control input signals computed in presence of high-frequency motion disturbances. (a) u. (b) τ_ψ. (c) τ_θ. (d) τ_φ.

Computed robust control inputs are shown in Figure 17. The high-frequency motion disturbance compensation is evident. Effectiveness and robustness of the dynamic controllers are hence confirmed. In this experiment, the reference for yaw motion was set as: $\psi^* = 0$ rad. From yielded results, it can be verified that the proposed dynamic motion tracking control is able to safely drive the quadrotor in the three-dimensional space in presence of undesirable high-frequency motions. It can be also corroborated that the quadrotor control achieves an acceptable trajectory tracking under reasonable time-varying operational uncertainties.

6. Conclusions

A novel and effective method based on active suppression of external and internal uncertainties for controlling the stable flight of a quadrotor helicopter in highly disturbed operating environments was introduced. A solution alternative for robust and efficient motion trajectory tracking tasks for an underactuated nonlinear aerial quadrotor vehicle under relevant uncertainties, from an active disturbance rejection perspective, has been proposed. Trajectory tracking is satisfactorily achieved by the controlled quadrotor. Main differences of the proposed

desired motion tracking control approach with other important contributions have been highlighted. Robust asymptotic state observers for real-time estimation of disturbances and time derivatives are unnecessary. Dependence on detailed mathematical models of the complex nonlinear unmanned aerial system dynamics is considerably reduced. Two virtual controllers were designed to face the underactuated motion problem, and consequently, perform a suitable tracking of the planned references. Proposed dynamic compensators are able to actively reject disturbances in real time. Output signal measurements are only required for a proper tracking of the planned trajectories. Three strict case studies confirmed the robustness and efficiency of the proposed motion control scheme under hostile operating conditions. It was also proved that the presented active control approach can be directly extended for a class of vibrating mechanical systems. Therefore, analytical, experimental, and numerical results proved that the introduced motion trajectory tracking control method stands for a very good alternative to actively suppress disturbances. Future research works deal with the extension of the presented control design perspective to other nonlinear configurations of dynamically underactuated helicopters with multiple rotors operating

under uncertainty. In this context, effects of significant uncertainties and analysis of the transient behaviour of several controlled multirotor aerial vehicles will be considered in future works as well.

Data Availability

The data used to support the findings of the study are available from the corresponding author upon request.

Conflicts of Interest

The authors declare that they have no conflicts of interest.

References

[1] B. Siciliano and O. Khatib, *Springer Handbook of Robotics*, Springer International Publishing, Berlin, Germany, 2nd edition, 2016.

[2] X. Shao, N. Liu, Z. Wang, W. Zhang, and W. Yang, "Neuroadaptive integral robust control of visual quadrotor for tracking a moving object," *Mechanical Systems and Signal Processing*, vol. 136, Article ID 106513, 2020.

[3] P. Castillo, R. Lozano, and A. Dzul, *Modelling and Control of Mini-Flying Machines*, Springer Publishing Company, Inc., New York, NY, USA, 1st edition, 2010.

[4] P. Corke, *Robotics, Vision and Control: Fundamental Algorithms in MATLAB*, Springer Publishing Company, New York, NY, USA, 2nd edition, 2017.

[5] S. Bouabdallah, A. Noth, and R. Siegwart, "PID vs LQ control techniques applied to an indoor micro quadrotor," in *Proceedings of the 2004 IEEE/RSJ International Conference on Intelligent Robots and Systems (IROS)*, vol. 3, pp. 2451–2456, Sendai, Japan, October 2004.

[6] G. Hoffmann, H. Huang, S. Waslander, and C. Tomlin, "Quadrotor helicopter flight dynamics and control: theory and experiment," in *Proceedings of the AIAA Guidance, Navigation and Control Conference and Exhibit, American Institute of Aeronautics and Astronautics*, pp. 1670–1689, Hilton Head, SC, USA, August 2007.

[7] A. A. Mian and W. Daobo, "Modeling and backstepping-based nonlinear control strategy for a 6 DOF quadrotor helicopter," *Chinese Journal of Aeronautics*, vol. 21, no. 1, pp. 261–268, 2008.

[8] A. Modirrousta and M. Khodabandeh, "A novel nonlinear hybrid controller design for an uncertain quadrotor with disturbances," *Aerospace Science and Technology*, vol. 45, pp. 294–308, 2015.

[9] A. Noormohammadi-Asl, O. Esrafilian, M. Ahangar Arzati, and H. D. Taghirad, "System identification and $H\infty$-based control of quadrotor attitude," *Mechanical Systems and Signal Processing*, vol. 135, Article ID 106358, 2020.

[10] Z. Cai, J. Lou, J. Zhao, K. Wu, N. Liu, and Y. X. Wang, "Quadrotor trajectory tracking and obstacle avoidance by chaotic grey wolf optimization-based active disturbance rejection control," *Mechanical Systems and Signal Processing*, vol. 128, pp. 636–654, 2019.

[11] J. Han, "From PID to active disturbance rejection control," *IEEE Transactions on Industrial Electronics*, vol. 56, no. 3, pp. 900–906, 2009.

[12] Z. Gao, "Active disturbance rejection control: a paradigm shift in feedback control system design," in *Proceedings of the 2006 American Control Conference*, pp. 2399–2405, Minneapolis, MN, USA, June 2006.

[13] J. Li, R. Li, and H. Zheng, "Quadrotor modeling and control based on linear active disturbance rejection control," in *Proceedings of the 2016 35th Chinese Control Conference (CCC)*, pp. 10651–10656, Chengdu, China, July 2016.

[14] H. Lu, X. Zhu, C. Ren, S. Ma, and W. Wang, "Active disturbance rejection sliding mode altitude and attitude control of a quadrotor with uncertainties," in *Proceedings of the 2016 12th World Congress on Intelligent Control and Automation (WCICA)*, pp. 1366–1371, Guilin, China, June 2016.

[15] R. Sanz, P. Garcia, and P. Albertos, "Active disturbance rejection by state feedback: experimental validation in a 3-DOF quadrotor platform," in *Proceedings of the 2015 54th Annual Conference of the Society of Instrument and Control Engineers of Japan (SICE)*, pp. 794–799, Hangzhou, China, July 2015.

[16] W. Dong, G.-Y. Gu, X. Zhu, and H. Ding, "A high-performance flight control approach for quadrotors using a modified active disturbance rejection technique," *Robotics and Autonomous Systems*, vol. 83, pp. 177–187, 2016.

[17] M. Fliess, R. Marquez, E. Delaleau, and H. Sira-Ramírez, "Correcteurs proportionnels-intégraux généralisés," *ESAIM: Control, Optimisation and Calculus of Variations*, vol. 7, pp. 23–41, 2002.

[18] F. Beltran-Carbajal and G. Silva-Navarro, "Generalized nonlinear stiffness identification on controlled mechanical vibrating systems," *Asian Journal of Control*, vol. 21, no. 3, pp. 1281–1292, 2019.

[19] F. Beltran-Carbajal, G. Silva-Navarro, and L. G. Trujillo-Franco, "A sequential algebraic parametric identification approach for nonlinear vibrating mechanical systems," *Asian Journal of Control*, vol. 19, no. 4, pp. 1564–1574, 2017.

[20] F. Beltran-Carbajal, R. Tapia-Olvera, I. Lopez-Garcia, A. Valderrabano-Gonzalez, J. C. Rosas-Caro, and J. L. Hernandez-Avila, "Extended PI feedback tracking control for synchronous motors," *International Journal of Control, Automation and Systems*, vol. 17, no. 6, pp. 1346–1358, 2019.

[21] F. Beltran-Carbajal, A. Favela-Contreras, J. L. Hernandez-Avila, O. Olvera-Tapia, D. Sotelo, and C. Sotelo, "Dynamic output feedback control for desired motion tracking on synchronous motors," *International Transactions on Electrical Energy Systems*, vol. 30, no. 3, Article ID e12260, 2020.

[22] S. Elias, R. Rupakhety, and S. Olafsson, "Analysis of a benchmark building installed with tuned mass dampers under wind and earthquake loads," *Shock and Vibration*, vol. 2019, Article ID 7091819, 13 pages, 2019.

[23] B. G. Korenev and L. M. Reznikov, *Dynamic Vibration Absorbers: Theory and Technical Applications*, John Wiley & Sons, England, UK, 1993.

[24] A. Yanik, "Absolute instantaneous optimal control performance index for active vibration control of structures under seismic excitation," *Shock and Vibration*, vol. 2019, Article ID 4207427, 13 pages, 2019.

[25] P. Castillo, P. García, R. Lozano, and P. Albertos, "Modelado y estabilización de un helicóptero con cuatro rotores," *Revista Iberoamericana De Automática e Informática Industrial RIAI*, vol. 4, no. 1, pp. 41–57, 2007.

[26] P. Castillo, L. E. Muñoz, and O. Santos, "Robust control algorithm for a rotorcraft disturbed by crosswind," *IEEE Transactions on Aerospace and Electronic Systems*, vol. 50, no. 1, pp. 756–763, 2014.